Synthesis and Characterization of Dyes

with Solar Energy Applications

by

Bradley J. Brennan

A Dissertation Presented in Partial Fulfillment
of the Requirements for the Degree
Doctor of Philosophy

Approved April 2012 by the
Graduate Supervisory Committee:

Devens Gust, Chair
James P. Allen
Thomas A. Moore

ARIZONA STATE UNIVERSITY

May 2012

ABSTRACT

The sun provides Earth with a virtually limitless source of energy capable of sustaining all of humanity's needs. Photosynthetic organisms have exploited this energy for eons. However, efficiently converting solar radiation into a readily available and easily transportable form is complex. New materials with optimized physical, electrochemical, and photophysical properties are at the forefront of organic solar energy conversion research. In the work presented herein, porphyrin and organometallic dyes with widely-varied properties were studied for solar energy applications. In one project, porphyrins and porphyrin-fullerene dyads with aniline-like features were polymerized via electrochemical methods into semiconductive thin films. These were shown to have high visible light absorption and stable physical and electrochemical properties. However, experimentation using porphyrin polymer films as both the light absorber and semiconductor in a photoelectrochemical cell showed relatively low efficiency of converting absorbed solar energy into electricity. In separate work, tetra-aryl porphyrin derivatives were examined in conjunction with wide-bandgap semiconductive oxides TiO_2 and SnO_2. Carboxylic acid-, phosphonic acid-, and silatrane-functionalized porphyrins were obtained or synthesized for attachment to the metal oxide species. Electrochemical, photophysical, photoelectrochemical, and surface stability studies of the porphyrins were performed for comparative purposes. The order of surface linkage stability on TiO_2 in alkaline conditions, from most stable to least, was determined to be siloxane > phosphonate > carboxylate. Finally, porphyrin dimers fused via their meso and beta positions were synthesized using a chemical oxidative synthesis with a copper(II) oxidant. The molecules exhibit strong absorption in the visible and near-infrared spectral regions as well as interesting electrochemical properties suggesting possible applications in light harvesting and redox catalysis.

ACKNOWLEDGMENTS

I would like to thank a number of people and organizations for their role in my research, my education, and my life in general. I must first thank my advisor Prof. Devens Gust and collaborators Profs. Tom and Ana Moore. They accepted me into their research group without reservation and provided me with their wisdom and resources. They embraced my research ideas and serendipitous discoveries, and allowed me to pursue multiple lines of research. I also could not have done any of the research without the members of the Gust Moore^2 research group, whom are among the most talented and brightest around. In particular I would like to thank Michael Hambourger for mentoring me and providing extensive knowledge and support over the years, Paul Liddell for his synthetic knowledge and providing me with every molecule I desired, Gerdenis Kodis and Amy Keirstead for their photophysical expertise, and Jim Bridgewater for his unlimited engineering skills. I would like to thank the members of the NSF-IGERT fellowship, members of the Center for Solid State Science, and the ASU Department of Chemistry and Biochemistry faculty for their fruitful discussions and integral help. Many thanks to the NSF-IGERT fellowship program, ASU, Sharp Corporation, NSF, and DOE for funding.

Beyond my research, I could not have seen all the angles of energy within our society without the help of the ASU Consortium for Science Policy & Outcomes, specifically Ira Bennett and Jameson Wetmore, and the members of the Energy, Ethics, Society and Policy working group.

I am deeply indebted to my friends and family for their enthusiasm, and to Chandra Goff my constant companion and life partner. They have seen me through my greatest triumphs and my darkest of days with unrelenting support. Finally, I would like to thank my doctors and their staffs for helping me prevail during my time of crisis, and without whom this document may never have been written.

TABLE OF CONTENTS

Page

CHAPTER

CHAPTER Page

APPENDIX

LIST OF TABLES

Table Page

LIST OF FIGURES

Figure Page

Figure Page

LIST OF ABBREVIATIONS

A	Absorbance
CB	Conduction band
CV	Cyclic voltammetry
D_{CT}	Diffusion charge transfer coefficient
DMAP	4-Dimethylaminopyridine
DMF	Dimethylformamide
DMSO	Dimethylsulfoxide
DSSC	Dye sensitized solar cell
EDCI	*N*-(3-Dimethylaminopropyl)-*N′*-ethylcarbodiimide hydrochloride
η	Power conversion efficiency
E	Energy
FF	Fill factor
FTO	Fluorinated tin oxide on glass
HPLC-GPC	High performance liquid chromatography – gel permeation chromatography
$h\nu$	Photon of light
I	Electrical current
I_{max}	Electrical current at maximum power
i_p	Current at electrochemical redox peak
I^-	Iodide
I_3^-	Tri-iodide

IPCE	Incident photon to current efficiency
IR	Infrared
ITO	Indium tin oxide on glass
IQE	Internal quantum efficiency
J_{sc}	Short-circuit photocurrent
KCl	Potassium chloride
λ	Wavelength
LHE	Light harvesting efficiency
$LiClO_4$	Lithium perchlorate
MALDI-TOF-MS	Matrix assisted laser desorption ionization – time of flight – mass spectrometry
MTHF	2-Methyltetrahydrofuran
NADH	*β*-Nicotinamide adenine dinucleotide reduced disodium salt
ν	Cyclic voltammetry scan rate
PEC	Photoelectrochemical cell
P_{in}	Power density of incident radiation
R	Resistance
SCE	Saturated calomel electrode
SnO_2	Tin oxide
$TBAPF_6$	Tetra-*n*-butylammonium hexafluorophosphate
TES	*N*-tris(hydroxymethyl)methyl-2-aminoethane-sulfonic acid
THF	Tetrahydrofuran
TiO_2	Titanium dioxide

TLC	Thin layer chromatography
UV-Vis-NIR	Ultraviolet - Visible - Near-infrared
V_d	Decrease in applied potential
V_{max}	Voltage at maximum power
V_{oc}	Open-circuit voltage

PREFACE

Few world issues compare to the challenge of providing for our ever-increasing energy consumption, without which our socio-technological house of cards would collapse. Energy in all its forms has been a staple of human progress for ages. From the advent of fire to the introduction of internal combustion engines to the multi-gigawatt fossil fuel power plants, our ability to burn hydrocarbon resources has spurred our earthly domination. Its ubiquity is the foundation of Western society, and our culture has been shaped by it. Our cities and country are designed around the energy infrastructure, our farms dependent on energy-intensive fertilizer production, and our personal habits closely linked to energy-demanding technologies.

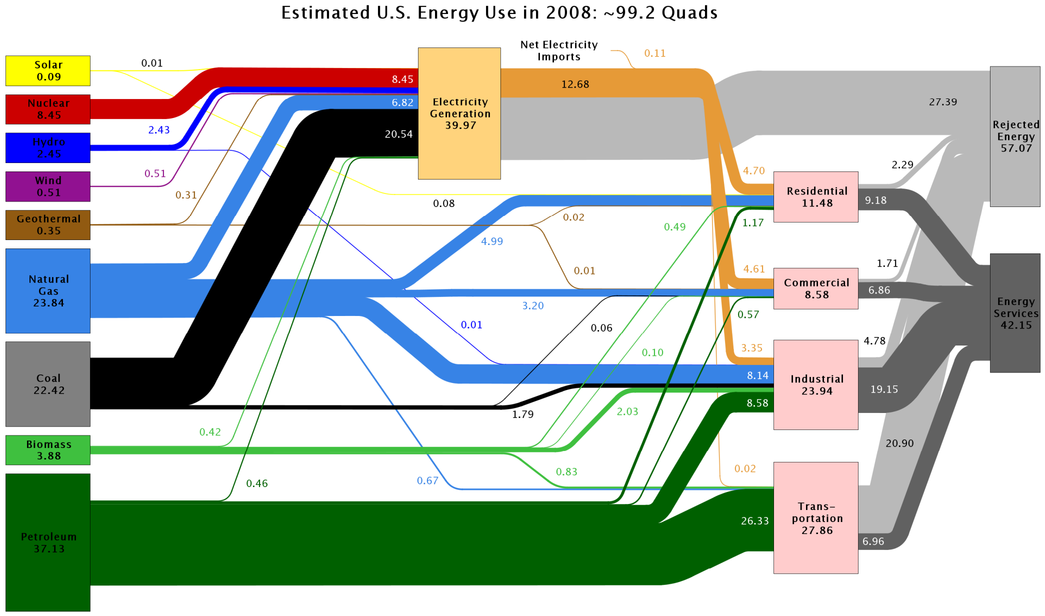

Figure 1. U.S. energy consumption – 2008. [1]

The United States consumed the equivalent of ~99 quadrillion Btu (quads) of energy in 2008 compared to a worldwide use of ~505 quads.[1-2] At nearly 20% of the world's consumption with a much lower percentage of the world's population, the United States has used cheap energy to propel it to the world's largest economy.[3] Most of the United States' energy comes from fossil fuels as shown in Figure 1, the bulk of which are the ancient decomposed remains of lifeforms. Being such, their extraction is unsustainable at the current rates and will eventually be depleted. Figure 1 shows that fossil fuels dominate each energy sector, making all aspects of the economy and lifestyle unsustainable in the long term.

Fossil fuels contain an inherent moral dichotomy. As they have helped increase the standard of living through technological progress, they have eroded the environment. Water quality issues from fracking for natural gas, runoff from coal mining, and acid rain seem mundane secondary problems compared to the longer term consequences of climate disruptions. Methane and carbon dioxide are greenhouse gases, and their release into the environment is a direct consequence of procuring, processing, or burning fossil fuels. The unrelenting increase in their atmospheric concentrations is well known, the hypothesized effects being realized, and the political discussions surrounding it controversial.[4]

With all the clamor regarding the issues of greenhouse gases, climate change, and oil imports in the media, one forgets the basis of the arguments: energy is required for society to function. Must we use fossil fuel sources? No. The sun provides 5.6×10^{24} joules of energy a year equating to > 5.3 million quads, which is over 10000 times the current energy usage.[5] With only 0.01% of that energy required for world demand, and with the sun being a sustainable resource, switching our main energy source to solar appears to be a logical move.

However, much change must occur for this transition. Some of it is technological, such as making existing solar energy conversion devices cheaper and more efficient. There is also a need to develop efficient methods of storing, transporting, and using that energy in all its forms. These technologies are currently moving through the stages of research and development or are already commercialized.

The techno-change is a fluid process, ever-changing. Innovators rule this area, mesmerizing even the most creative of minds with their developments. However, technology alone cannot change the world. The main obstacle to change is society itself. The energy transition can be described in many ways as a cultural transition with a technological component. All the technologies, be they crude or not, are already available; however they are not fully embraced by society. Without this support the energy transition is low on the list of society's priorities and progress is slow.

In preparation of the inevitable increase in solar energy usage, research is ongoing into conversion of sunlight into electricity and energy-dense chemicals such as hydrogen gas. Herein is the progress made into this field over the course of a graduate student career, advancing previous research by others and leaving many possibilities for the future.

1. OVERVIEW OF PHOTOELECTROCHEMICAL CELLS

1.1. PEC Design and Processes

A photoelectrochemical cell (PEC) is a generic term for a device that uses an absorbed photon to initiate an electrochemical cascade of reactions, producing an electrical current. The materials involved can vary considerably, however there must be a pathway for electrons to flow through the entire circuit. Solid conductors, semiconductors, and liquids containing redox-active electrolytes are the three main classes of materials used to compose the circuit.

Assembling and testing a photoelectrochemical cell is a direct method of analyzing the photoelectrochemical properties of a dye in conjunction with other specific materials in a device. PEC analyses will be shown throughout this text to compare light-absorbing materials utilizing multiple device designs.

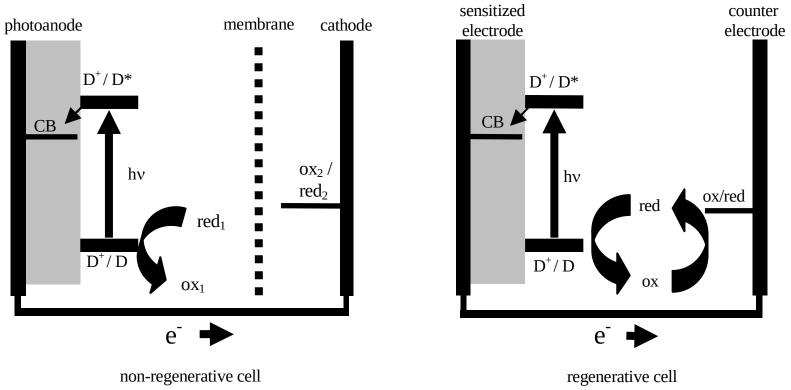

Figure 2. General PEC designs. Non-regenerative cell (left) and regenerative cell (right). Redox processes are shown as oxidized/reduced and correspond to the general formula (oxidized + ne$^-$ → reduced). Ox$_1$/red$_1$ and ox$_2$/red$_2$ correspond to separate redox couples. The dashed line in the non-regenerative cell corresponds to a semi-permeable membrane separating the anode and cathode. See text for specifics.

The two general types of PEC used in this text are shown in Figure 2 as non-regenerative and regenerative in design. Each type uses the same theory involving a photoelectrochemical cascade after light absorption by a photoactive species, but the non-regenerative has non-cyclical electron flow with electrochemical formation of oxidized and reduced products while the regenerative has continuous flow with cyclical redox components. No electron flow occurs in the absence of light. The directional flow of electrons (e^-) through the circuit depends on the redox potentials of all the species, with photo-anodic current shown for each type in Figure 2. The photoelectrochemical cascade is based on the redox gradients within the system, with electrons moving from more negative values to more positive values in the context of this text.

The mechanism of action for both designs in Figure 2 first involves a light-harvesting material or dye (D) absorbing a photon of light (hν), exciting an electron within the molecule to a higher-energy orbital (D*). The excited electron relaxes to the lowest energy singlet excited state according to Kasha's Rule. It can also then undergo intersystem crossing to a triplet state of lower energy.

$$E_{D^+/D^*} = E_{D^+/D} - E_{D^*} \qquad \text{(eq. 1)}$$

The excited species D* has a potential for oxidation determined by Equation 1. The ground-state oxidation potential of species D ($E_{D^+/D}$) is reduced by the energy of the dye excited state (E_{D^*}), yielding the electrochemical potential for D* to give up an electron and become oxidized (E_{D^+/D^*}). The value for D^+/D^* is therefore more negative than D^+/D, making D* a better reductant and able to give up its electron to another species with a more positive redox potential. The value for D^+/D is normally obtained by a voltammetric method such as cyclic voltammetry, with the excited state energy value obtained by spectroscopic methods.

In the two PEC designs shown in Figure 2, D is connected to a metal-oxide semiconductor; however this is not a requirement for PEC as will be seen in Chapter 2 where the polymeric light harvesting species is also the charge carrier. Metal oxide semiconductors have a conduction band (CB), an electronic region containing a high density of states capable of low-resistance electron flow.[6] When a species has a reduction potential more negative than the edge of the CB, the electron can occupy the electronic region of that material. Correspondingly, when D absorbs light to produce D*, it is able to transfer an electron to the semiconductor CB, provided the CB potential is more positive than E_{D^+/D^*}. This process forms D^+ and generates a charge separated state with the CB. This is generally called photo-induced electron transfer or electron injection. At this point the non-regenerative and regenerative cells differ.

In the non-regenerative cell shown in Figure 2, the injected electron travels with a redox potential corresponding to the potential of the semiconductor CB through the circuit to the cathode. At the cathode, the electron reduces a material (ox_2) in another redox process to form a reduced product (red_2). The cathodic side of the cell therefore accumulates this reduced species over time. The photoanode is contained in a compartment with the electrolyte containing a species (red_1) with a redox potential more negative than D^+ and therefore capable of reducing the oxidized dye D^+ back to D. This electron donor becomes oxidized, and is therefore consumed over time to form ox_1. The anodic and cathodic solutions are separated by a semi-permeable membrane such as Nafion®, allowing the electrodes to be in electrical contact while preventing the anodic and cathodic products from crossing into the other compartment. Overall, the absorption of one photon by the dye causes a single electron to move through the circuit, generating one molecule of the oxidized product (at the anode) and one molecule of the reduced product (at the cathode), assuming both are single-electron processes.

In the regenerative cell configuration shown in Figure 2, the process is simpler due to the regeneration of a redox mediator in the electrolyte. After injection of an electron in the semiconductor CB, the oxidized dye D^+ gets reduced to D by the reduced form of the redox species (red) in the electrolyte. The electron in the semiconductor CB travels to the counter electrode where it reduces the oxidized form of the electron donor (ox) to the reduced form (red). Overall, the redox mediator forms a complete circuit through the electrolyte, resulting in the net generation of electricity without a net chemical change in the cell.

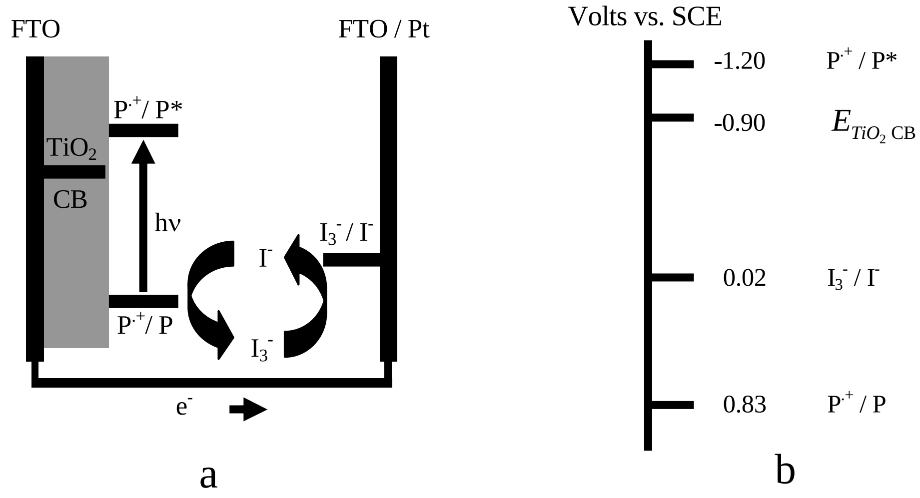

Figure 3. Grätzel-type DSSC. PEC design (3a) and general redox potentials of system components (3b).[7] Potentials for dye molecule (P) come from porphyrin **Zn-24**, examined in Chapter 3. TiO_2 conduction band potential varies widely with solvent and electrolyte, and is shown here as the value in acetonitrile solvent with 100 mM $LiClO_4$.[6-8] See text for specifics.

An example of a regenerative PEC is the dye-sensitized solar cell (DSSC) pioneered by Michael Grätzel and co-workers and shown in Figure 3a.[9] A nanoporous anatase crystalline-phase TiO_2 semiconductor film is coated with a monolayer of dye, normally using a carboxylic acid moiety of the dye to bind it to the surface. In the above example, the dye is a carboxylic acid analogue of tetra-aryl porphyrin **Zn-24** which is examined in Chapter 3. The DSSC functions as a regenerative PEC with the redox potentials of the system shown in Figure 3b. Electrons flow in the downward direction on the chart, towards more positive potentials. With each absorbed photon (hν), the excited porphyrin dye P* is able to inject an electron into the conduction band of TiO_2 with subsequent formation of the porphyrin radical cation ($P^{\cdot+}$). The electrons travel in the external circuit to the platinized FTO electrode, with the platinum serving to catalyze the reduction of I_3^- to I^-. The reduced species I^- is able to be oxidized by $P^{\cdot+}$, completing the electronic pathway.

The electrical current is determined by the number of electrons flowing in the photoelectrochemical cascade, and the output voltage is determined by the difference in electrochemical potentials of the processes at the two electrodes. In the DSSC in Figure 3, the electrode potentials correspond to TiO_2 E_{CB} and that of the I_3^-/I^- redox couple, giving a maximum theoretical voltage of 920 mV. By altering the potentials at each electrode, the output voltage can be altered; however the maximum theoretical current is still dependent on the number of photons absorbed by the system.

While the voltage is typically set by the choice of materials and device design, the current is determined by the light-harvesting ability of the dye and the efficiency of electron flow in the photoelectrochemical cascade. The dye can only absorb photons in a certain range of the solar spectrum, specifically photons with energies above its singlet excited state energy, providing an upper limit to the number of photo-excited electrons available. Due to the dye excited state redox properties being associated with the excitation energy as shown in Equation 1, there can be a tradeoff between harvesting more of the solar spectrum and obtaining redox potentials that fit within the redox potential confines of the PEC.[10] In addition, each photo-excited dye does not equate to an observable electron in the PEC photocurrent. Upon excitation, the dye must be able to transfer an electron to another redox-active material. These electron exchanges can occur through the same material or through different materials, but eventually the electron must be capable of traversing the entire circuit. The photoelectrochemical cascade can be summarized as a series of processes that involve producing a charge-separated state and routing those charges through a set of materials. Along the electronic pathway there are a number of places where those charges can recombine, removing them from the observed photocurrent output. All boundaries between redox-active materials are considered points of possible recombination, with the kinetics of the competing processes deciding the efficiency of the recombination mechanisms. Thus, device design considerations for the materials and construction are integral to thwarting recombination processes.

Due to the complexity and multitude of PEC designs and materials in the literature, a more detailed explanation of PEC system components, the effects of their alteration, and the fabrication of the specific PEC devices used in these studies is provided.

1.2. Conductive Substrates

PEC requires that light penetrate the device so that it can be absorbed by the photoactive material. The easiest way to incorporate a transparent window is to use glass or a transparent plastic as one of the substrates. In addition, it is particularly useful for the substrate to be electrically conductive so it can be used as a collector of the charge carriers from the photoactive materials. Generally, the transparent conductive material works as one or both of the electrodes in the PEC.

Transparent conductive substrates are generally prepared by taking a non-conductive substrate and adding a thin layer of conductive material. Commercially available transparent conductive substrates composed of silica glass with a thin conductive layer of either indium doped tin oxide (ITO) or fluorinated tin oxide (FTO) are commonly used. Doping of the semiconductor tin oxide with indium or fluorine gives a high conductivity.[11]

$$V_d = I\,R \qquad \text{(eq. 2)}$$

Conductivity allows for a flow of charge through the material and high conductivity (low resistance) is required for systems where charge flow could cause a voltage drop in the system according to Equation 2. The equation shows that the current flow (I) in amps in a material with a certain resistance (R) defines the voltage drop (V_d) within the system. For PEC, this amounts to a decrease in the voltage output of the system, and therefore its overall efficiency. The resistance values for ITO and FTO are on the order of 10 Ω/sq, allowing for a reasonable amount of current to flow through the conductive electrodes of a small PEC without a noticeable voltage drop.[11]

1.3. Metal Oxides and Metal Oxide Electrodes

When working with molecular dyes as sensitizers in PEC, a monolayer on a flat conductive surface only allows for a very small percentage of light to be absorbed. This inefficient use of electrode area was overcome by the emergence of high surface area semiconductors.[12-13] Using nano-sized semiconductive particles, the fabrication of porous semiconductive electrodes can produce surface areas over 2000 times that of a flat surface.[9, 14] This increase in surface area provides an equally high increase in the amount of the molecule that binds to the surface as shown in Figure 4. In the case of dyes, the electrode would then be able to absorb a much greater proportion of light.

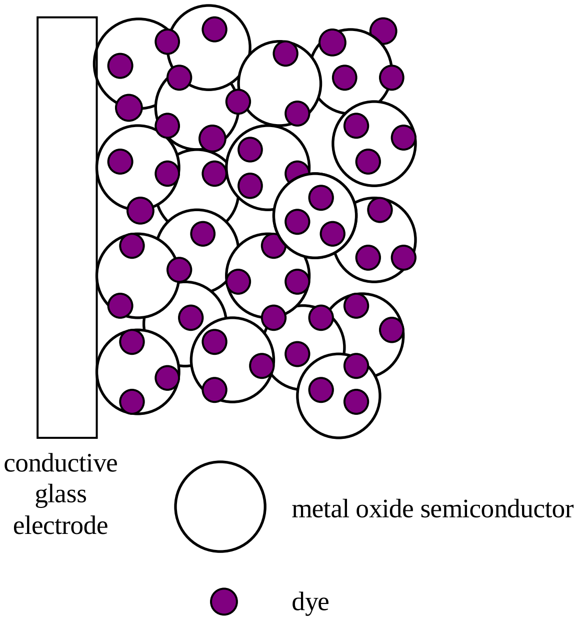

Figure 4. Dye-sensitized porous metal oxide electrode

The choice of semiconductor is dependent upon the characteristics desired. For DSSC the semiconductor should be transparent to visible light with a conduction band accessible to a photo-excited dye. This requires a wide-bandgap semiconductor. Bandgap is a semiconductor electronics term defined as the difference in energy (eV) between the populated valence band of electrons and the unoccupied conduction band, with that energy corresponding to a wavelength of light by Equation 3. Semiconductors are capable of absorbing photons of higher energy than their bandgap.

$E_{\mathrm{eV}} = \frac{1240_{eVnm}}{\lambda_{nm}}$ Where E is energy in eV and λ is wavelength in nm. (eq. 3)

Two of the most widely used wide-bandgap semiconductors are tin oxide (SnO_2) and titanium dioxide (TiO_2). Wide-bandgap semiconductors absorb light in the UV region and thus leave open the visible-light regions for the dyes to absorb. The semiconductor is used as an organizational structure and as a conduit for electrons via its conduction band. Semiconductors also have an advantage over metallic conductors by having lower rates of detrimental interfacial electron recombination processes in PEC devices.

1.4. Light-Harvesting Materials

The key to any PEC is the photoactive compound used to absorb light and initiate the photoelectrochemical cascade. In the case of the experiments herein, the photoactive materials are either small molecules or polymers. Molecules with π-conjugated bonding such as porphyrins can absorb light throughout the visible region and become excited in a π to π* transition[15] while organometallic dyes such as ruthenium polypyridyl derivatives have a metal-to-ligand charge transfer in the visible spectral region.[8, 16] Small molecules are typically bonded to porous metal oxide semiconductive electrodes while polymers are used as thin films in replacement of the semiconductor.

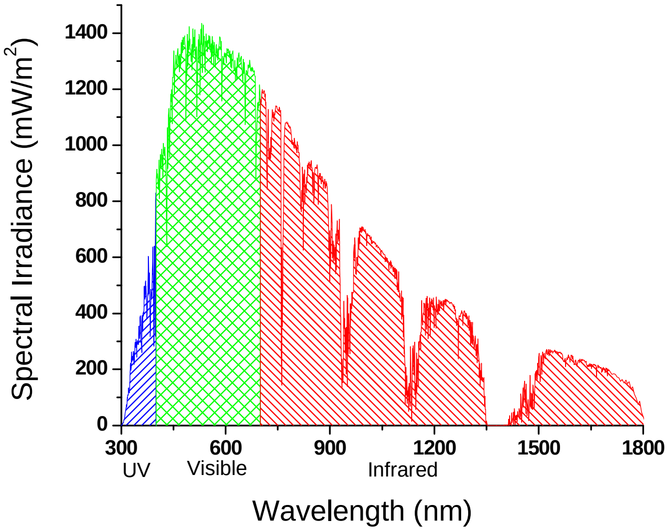

Figure 5. AM1.5G solar spectrum. Truncated solar irradiance AM1.5 global spectrum from 300 to 1800 nm, with ultraviolet (blue), visible (green), and infrared (red). Source: National Renewable Energy Laboratory - http://rredc.nrel.gov/solar/spectra/am1.5.

The light-harvesting properties of the photoactive material are important in determining its efficiency in gathering photons. The solar irradiance spectrum in Figure 5 relates to the terrestrial surface exposure to the sun's blackbody radiative output, with gaps due to absorbance from substances in the atmosphere. The peak solar energy hitting earth is in the visible region, with a long tail into the infrared region. Efficient light harvesting of the higher energy photons can thus be accomplished using photoactive materials capable of absorbing photons throughout the UV, visible, and near-infrared regions.

Beyond the light harvesting capabilities of the photoactive material, the electrochemical properties are very important. The PEC photoelectrochemical cascade is based on a flow of electrons dependent on the redox characteristics of all the species. The photo-excited material must be able to transfer an electron while its oxidized form must be able to take an electron from another species. Altering the molecular structure of the dye or changing the PEC materials are two commonly used methods to fit the electrochemical potentials of the dye into a PEC design.

1.5. Electrolytes

In PEC designs where a liquid is used between the electrodes, as is the case for the experiments herein, a number of constraints persist. First is that the liquid must be conductive. This is generally attained by using a supporting electrolyte in a suitable concentration (> 100 mM). The solvent and electrolytes should all be redox inactive unless used to shuttle electrons in the photoelectrochemical cascade. They should also be stable to irradiance and inert to the rest of the materials and processes in the system.

Electrochemical potentials of some materials are dependent on the solvent and electrolytes. In particular, metal oxide conduction band potentials vary with solvent and electrolyte. In aqueous solutions under standard conditions, metal oxide semiconductor conduction bands have a Nernstian pH dependence, with the CB potential becoming more negative by 59 mV per pH unit increase.[6, 17-18] In non-aqueous solutions this does not apply. However, lithium ions can intercalate into the semiconductor and affect the conduction band level in a similar way.[7] In addition, interactions between the metal oxide surface and solvents or dissolved species can change the surface conduction band potential.[8, 19-20]

In a DSSC there is a trend of using ionic liquids as electrolytes.[21] These are salts which are liquid at or near room temperature and which can contain a redox active component. Using a redox-active ionic liquid in the electrolyte allows for a high concentration of the desired species and also makes the solution conductive.[22-23] In addition, low volatility of ionic liquids makes evaporation and vapor pressure negligible. Due to the relatively high viscosity of commonly used ionic liquids, they are usually mixed with a low-viscosity solvent along with other additives.

Also contained in the DSSC electrolyte is lithium iodide, as a source of lithium and iodide ions, and iodine to complete the redox-active species I_3^- / I^-. A common additive is 4-*tert*-butylpyridine, which is thought to interact with the metal oxide surface and/or the redox electrolyte to increase overall efficiency.[8, 24] Additional additives can include guanidinium thiocyanate and benzimidazole analogues among others.[25-26] The electrolyte solvent is generally a mixture of alkyl-nitrile solvents with low viscosity, however a range of solvents have been used.[20]

The common redox species for DSSC is I_3^- / I^-, but others have been used.[27-28] Research into new redox species is ongoing. The focus has been to develop a species with a more positive oxidation potential than I^- to increase the theoretical V_{oc}. Tris-bipyridyl cobalt(II/III) complexes have shown promise.[29]

1.6. Counter Electrodes

With one electrode containing the photoactive material, the other electrode generally helps shuttle electrons through the system. In the case of DSSC, this generally entails a conductive material coated with platinum or another material capable of catalytic regeneration of I^- from I_3^-. In the case of non-regenerative PEC, an electron sink is required. The electrode must be able to accept electrons at the potentials of the semiconductor CB, and then use the electrochemical potential for a chemical reaction. This could involve the formation of an energy-rich product such as hydrogen gas, or could be a simple electrochemical reduction of a metal salt.

1.7. IPCE Testing

1.7.1. IPCE

Analysis of a PEC generally involves using a calibrated light source. Illumination of the PEC produces photocurrent when the light is capable of being absorbed by the photoactive material, and this can be analyzed in more detail depending on the method. One common method involves using a broad-spectrum light source and a monochromator to expose the PEC to specific wavelengths, with the output light calibrated for intensity. By measuring the photocurrent of the PEC at incremental wavelengths, and knowing the photon flux of that light, the incident-photon-to-current-efficiency (IPCE) curve can be obtained using Equation 4.[30]

$$\mathrm{IPCE}_{\lambda} = \frac{1.24 \ \mathrm{x} \ \mathrm{J}_{\mathrm{sc}} \ (\frac{\mu\mathrm{A}}{\mathrm{cm}^2})}{\mathrm{P}_{\mathrm{in}} \ (\frac{\mathrm{mW}}{\mathrm{cm}^2}) \ \mathrm{x} \ \lambda \, (\mathrm{nm})} \qquad \text{(eq. 4)}$$

Equation 4 states that the IPCE value at each wavelength (IPCE_λ) is calculated from the short-circuit current density (J_{sc}), the power density of the incident light at the specific wavelength (P_{in}), and the wavelength (λ), with the units shown. The constant 1.24 is derived from $\frac{\mathrm{N_A} hc}{F}$ where N_A is Avogadro’s number

$\frac{6.022x10^{23}}{\text{mol}}$, *h* is Plank's constant $\frac{6.626x10^{-34}\,\text{J}}{\text{s}}$, c is the speed of light $\frac{3.00x10^{8}\,\text{m}}{\text{s}}$, and F is Faraday's constant $\frac{96485\,\text{A s}}{\text{mol}}$.

As its name suggests, the IPCE curve describes the fraction of photons that strike the electrode at each wavelength that give rise to electrons flowing in the system. Since photoactive materials tend to absorb with different extinction coefficients at different wavelengths, the IPCE curve generally has a shape similar to that of an absorbance spectrum of the material.

1.7.2. IQE

The IPCE value is only a partial description of the PEC efficiency because it does not take into account the percentage of light absorbed, just the total light that strikes the electrode. For this reason the IPCE is often called the external quantum efficiency. When the percentage of light absorbed by the photoactive material is taken into account, the IPCE converts into the internal quantum efficiency (IQE). These values correspond to the number of electrons per absorbed photon at each wavelength tested. It is a more absolute efficiency for a system, removing an important variable. Converting the IPCE to IQE values involves knowing how much light is absorbed at each wavelength. This generally comes from the difference of the absorbance spectra of the electrode obtained before and after the photoactive material was added. Absorbance values (A) are logarithmic with the percentage of light absorbed, and so are converted to the light-harvesting efficiency (LHE) using Equation 5. The IQE is then determined using Equation 6. Generally, the IQE is the same at each wavelength absorbed unless other factors are involved.

$$\mathrm{LHE}_{\lambda} = 1 - 10^{-\mathrm{A}} \qquad \text{(eq. 5)}$$

$$\mathrm{IQE}_{\lambda} = \frac{\mathrm{IPCE}_{\lambda}}{\mathrm{LHE}_{\lambda}} \qquad \text{(eq. 6)}$$

1.7.3. AM1.5G Simulated Sunlight

While monochromatic light gives certain quantitative information for the PEC, analyses are also performed using real-world scenarios. The most common is using a simulated sun supplying light intensity equal to that hitting the earth. These are obtained using broad-spectrum lamp sources, generally xenon, with calibrated filters to simulate the solar spectrum. The AM1.5G spectrum shown in Figure 5 is associated with global average direct and diffusive sunlight through the atmosphere at a solar zenith angle of 48.2 degrees at a tilt of 37 degrees towards the sun (1.5 atmospheres) and factors in a number of average atmospheric values. Using intensity values of 1000 W/m^2, it is a good approximation of the average solar spectrum and intensity over the mid-latitudes of the northern hemisphere including much of the contiguous United States.

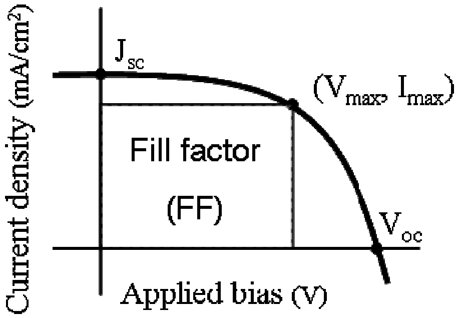

Figure 6. Current-voltage curve. J_{sc} corresponds to the electrical current with no applied bias. V_{oc} corresponds to the applied bias potential when no current is flowing. V_{max} and I_{max} correspond to the applied potential and current, respectively, that produce the maximum power output for the device. The fill factor (FF) is determine by Equation 7. See text for details.

When the AM1.5G spectrum at 1000 W/m^2 intensity is used as the incident radiation for the PEC, a number of commonly used values can be obtained. The general experimental procedure involves using an applied voltage bias on the PEC while illuminated. By scanning the applied bias, a current-voltage curve is obtained. An example is shown in Figure 6. With no applied bias, the photocurrent equates to the short-circuit current density (J_{sc}). With increasing applied bias, similar to placing an electrical load on the circuit, the current decreases until the PEC can no longer produce positive photocurrent. The applied bias at zero current is the open-circuit voltage (V_{oc}), related to the difference in redox potentials of the processes at the two electrodes in the PEC. With power coming from the product of current and voltage, the current-voltage curve contains a maximum power point (V_{max}, I_{max}) which helps determine the fill factor of the curve using Equation 7. The fill factor relates to how well the current-voltage curve simulates perfect diode behavior. Using Equation 8 and the variables discussed, the power conversion efficiency (η) corresponds to the maximum amount of power obtained in relation to the power input (P_{in}). When using AM1.5G simulated sunlight at 1000 W/m^2, η is the solar conversion efficiency standard used to compare PEC designs.

$$FF = \frac{I_{max} \text{ x } V_{max}}{J_{sc} \text{ x } V_{oc}} \qquad \text{(eq. 7)} \qquad\qquad \eta = \frac{J_{sc} \text{ x } V_{oc} \text{ x } FF}{P_{in}} \qquad \text{(eq. 8)}$$

2. PORPHYRIN POLYMER

2.1. Porphyrin Properties

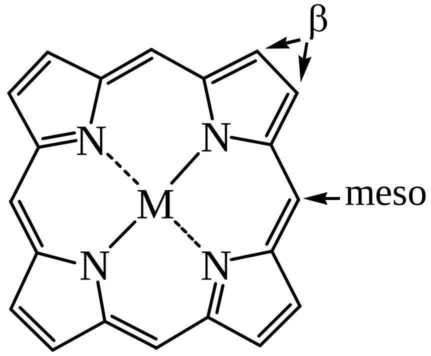

Figure 7. General porphyrin structure with β and meso positions shown. M can be a range of metal or non-metal atoms.

Porphyrins are synthetic analogues to the photosynthetic chlorophyll species, with general structure shown in Figure 7. The aromaticity and ease of synthetic alteration of the macrocyclic structure allows for a broad range of physical and electrochemical properties. Most notably, the interior of the macrocycle has the ability to chelate a wide array of metal atoms, each of which affects the physical and electrochemical properties differently.[31]

Porphyrins tend to absorb throughout the visible region in a π to π^* transition due to the large cyclic conjugation pathway and dipole transitions.[15, 31] Absorbance spectra generally contain a peak of high molar absorptivity near the UV region called the Soret band corresponding to the S_2 excited state, and up to four Q-band absorbance peaks in the visible with moderate molar absorptivity corresponding to the S_1 excited state. The fluorescence lifetimes of these excited molecules and their analogues can be over 10 nanoseconds, allowing for energy and/or electron transfers to occur before relaxation by unimolecular processes.[32-33] For all these reasons, porphyrins have been used extensively as light-harvesting dyes in photoelectrochemical cells (PEC).[29, 34-38]

2.2. Porphyrin Polymers

Generally, porphyrins are used in PEC by attaching to a porous semiconductor as described in Chapters 1 and 3. However the porphyrin itself can act as both a light-harvester and semiconductor. In polymeric form, researchers have been able to produce semiconducting porphyrin films with a range of electrochemical and physical features.[39-41] Porphyrin polymers are materials containing porphyrin units with a repeated bonding structure between them, generally without full conjugation between the macrocycles. In this way the porphyrin polymer physical and electrochemical properties are similar to the porphyrin monomer. However, depending on how the porphyrin is polymerized, additional redox mechanisms and/or photophysical features can be established. A major advantage to using polymerized material over monomeric ones is the ease of forming thin films and the ability of those films to electrically interact with both intra- and inter-molecular charge transfers.

Polymerization of porphyrins can be via conventional synthetic techniques[39] or via electrochemical methods.[40-41] The former generally involves a porphyrin capable of repeated coupling reactions, forming porphyrin polymers of various unit lengths. Electrochemical methods involve a multiple-electrode setup with a solution containing monomeric porphyrin. Applying an electrochemical potential (generally an anodic potential) to the electrode initiates an oxidation of the monomer species which then undergoes a coupling reaction with another monomer. Repeated reactions form a polymeric material which can be either soluble or insoluble in the reaction medium. If insoluble, the polymer will form a film on the electrode surface.

A number of oxidatively polymerized porphyrins have been characterized in the literature, most via electrochemical synthesis of thin films.[40, 42-43] These have been used for a number of purposes, from light harvesting to heterogeneous catalysis.[44-45] Our research group introduced a new variety of porphyrin polymer species derived from the monomers 5-(4-aminophenyl)-10,20-bis(2,4,6-trimethylphenyl)porphyrin **1** and a similar porphyrin-C_{60} analogue **2** shown in Figure 8.[46-47] These were electrochemically grown on conductive materials to form thin films.

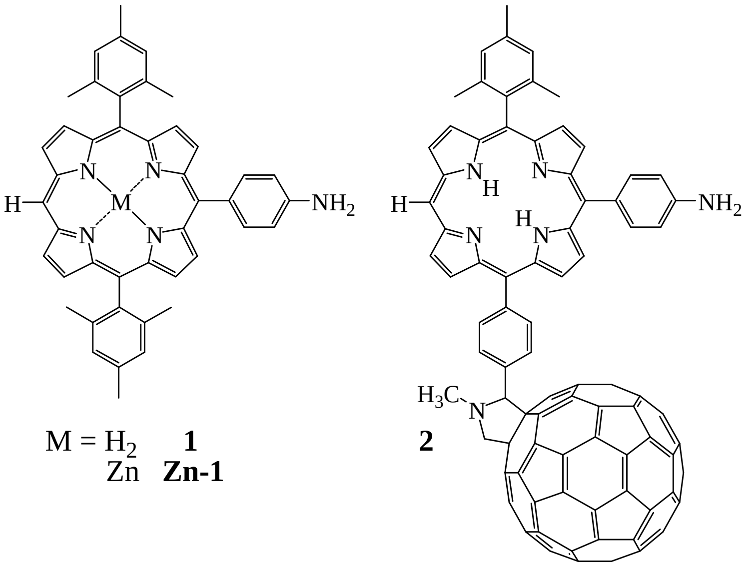

M = H_2 **1**
Zn **Zn-1**

2

Figure 8. Porphyrin monomers

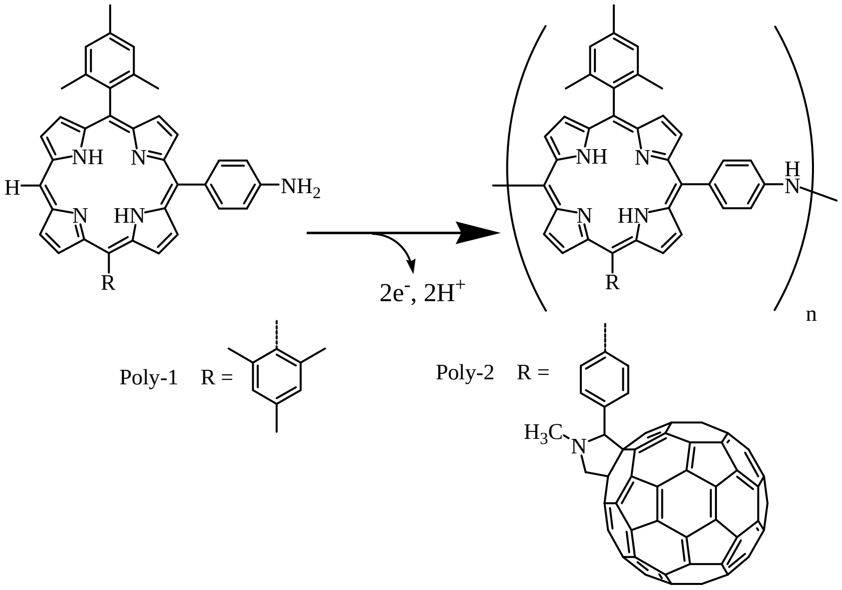

Figure 9. Porphyrin polymers

Porphyrins **1** and **2** were determined to oxidatively polymerize head-to-tail[46-47] much like that of the well-known polyaniline.[48] The general reaction is shown in Figure 9. In the case of these monomers, the porphyrin and aniline substituent are electronically partially disconnected due to rotation of the phenyl ring out of the porphyrin plane. Polymerization involves the single oxidation of the porphyrin macrocycle and of the aniline substituent, forming the radical cation species of each. A radical-radical coupling occurs between the porphyrin meso position and the aniline nitrogen, forming a new C-N bond along with release of two protons. Continued reactions produce chains with increasing numbers of porphyrin units.

Poly-1 and **Poly-2** both have the porphyrin macrocycle as the main component used for polymerization, with polymerization significantly altering the electrochemical potentials. The new porphyrin meso-aniline C-N bond makes the porphyrin polymer easier to oxidize than the monomer. It was determined that in its freebase (H_2) form, the porphyrin polymer is capable of acting as a p-type semiconductor by allowing intra- and inter-polymer transfer of holes (h^+) when oxidized.[46] In the case of **Poly-2**, the fullerene appendage is inert during the oxidative polymerization, but it is redox active when applying cathodic potentials where the fullerene can accept an electron.[47] It was also determined that excitation of **Poly-2** initiates an intra-molecular charge transfer between the porphyrin and fullerene substituent, forming the porphyrin radical cation and fullerene radical anion state ($P^{\cdot+}$ - $C_{60}{}^{\cdot-}$). This intrinsic charge separation allows for conversion of light energy into an electrochemical potential much like a p-n semiconductor junction, with the ability of those charges to transfer to neighboring porphyrins and fullerenes and propagate throughout the polymer films.

2.3. Electrochemically Polymerized Porphyrin

2.3.1. Synthesis

Polymeric films were produced by electrochemical oxidation of monomers **1**, **2**, or the metalated analogue **Zn-1** on metallic electrodes or conductive glass (FTO or ITO). Details of the electrochemical polymerization procedures for each monomer are contained in Chapter 6.2. Cyclic voltammetry (CV) was the preferred method of producing uniform films. By scanning the potential between where polymerization occurs and where the polymer is in the non-oxidized form, layers of precipitated polymer build up on the surface. This can be seen in Figure 10 with the growth of the polymer redox peaks. During the first potentiometric cycle there are three irreversible oxidations corresponding to the porphyrin macrocycle and aniline substituent. The first two overlapping near 1.0V vs. SCE correspond to the aniline and porphyrin macrocycle, with the third near 1.2V corresponding to the 2nd oxidation of the macrocycle.[46] Subsequent scans show a new set of redox peaks cathodic to those oxidations. These correspond to the additional polymer deposited. Continuous cycling of the potentials produces an increasingly thick film.

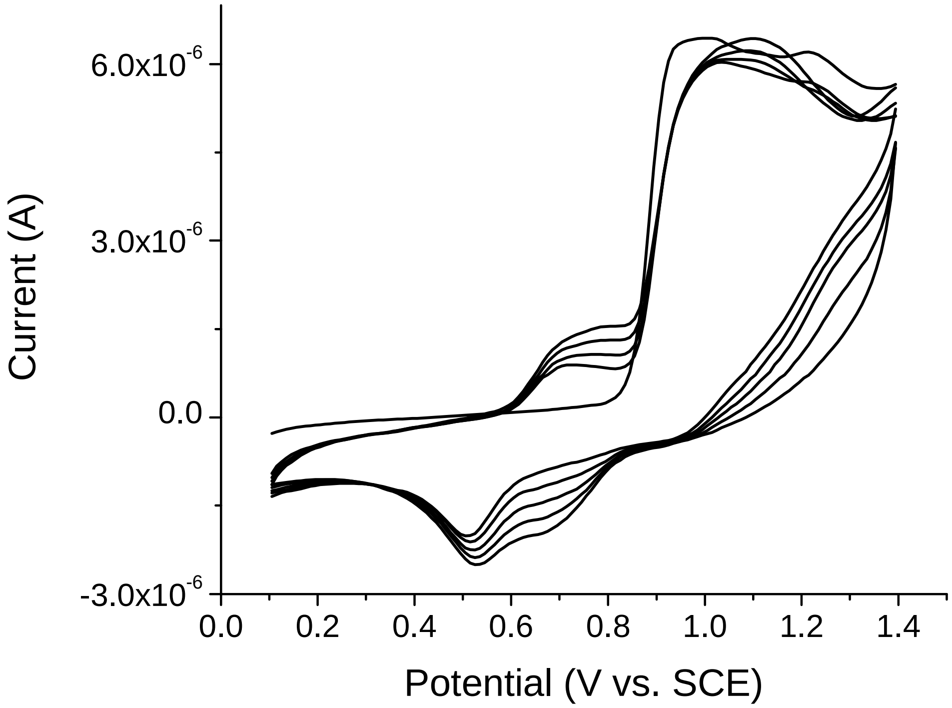

Figure 10. Electropolymerization of monomer **1** on platinum in acetonitrile with 100 mM $LiClO_4$ salt as electrolyte at a scan rate of 200 mV/sec.

2.3.2. Characterization

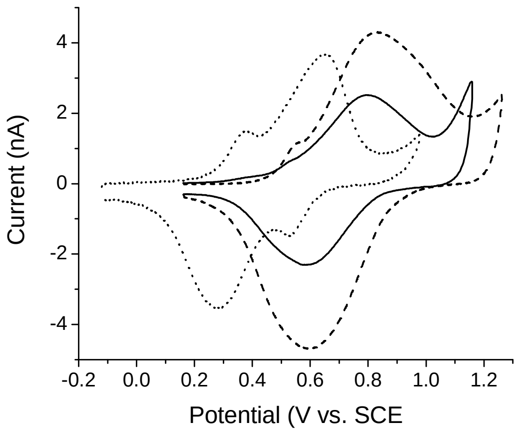

Figure 11. Cyclic voltammetry of polymer films **Poly-1** (solid), **Poly-2** (dashed), and **Zn-Poly-1** (dots) on platinum 25 μm electrode in acetonitrile with 100 mM $LiClO_4$ at a scan rate of 200 mV/sec.

Initial characterization of electropolymerized porphyrin thin films consisted of an electrochemical analysis. The polymer films were prepared by CV on platinum or conductive glass electrodes in a solution of monomer with added electrolytic salt for conductivity. After polymerization, the prepared films were rinsed and analyzed by CV in a porphyrin-free acetonitrile solution containing 100 mM $LiClO_4$ electrolyte. Repeated CV cycles resulting in the same spectra are a sign of good stability. Typical voltammograms of the polymers are shown in Figure 11. Note that there are no longer peaks for the monomer porphyrin and aniline, but a single main oxidation peak for each polymer species. **Poly-1** and **Poly-2** have similar oxidation potentials at 0.69V and 0.72V vs. SCE, respectively, due to the similar porphyrin structure while **Zn-Poly-1** is easier to oxidize due to the effects of zinc insertion. Also, **Poly-2** and **Zn-Poly-1** have shoulder peaks, possibly due to a “charge trapping” effect in the film. During the CV scan, charges can get trapped in the film, with their release occurring when the film is oxidized to the point of conductivity as discussed previously.[47]

When conductive glass is used as substrate, absorbance spectra can be obtained. Monomer and polymer spectra are shown in Figure 12. The polymer absorbance is slightly different than their respective monomers, with broadened features and red-shifting of the absorption bands. Notably, the ratio of Soret to Q-band absorbance intensities decreases in the polymers. Broadening could occur due to the aggregation of the porphyrin material in the solid-state while the shifting is due to the change in the porphyrin electronic states as a consequence of the new C-N bond formed during polymerization.

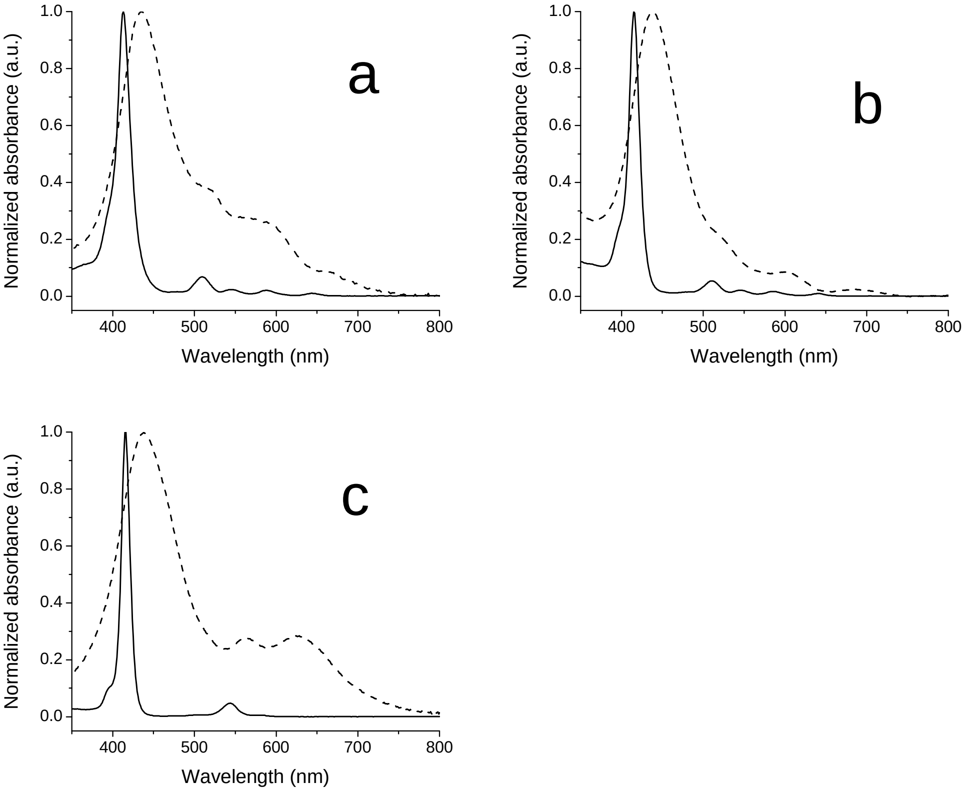

Figure 12. Monomer and polymer absorbance spectra. Monomers in solution of dichloromethane (line) and electropolymerized porphyrin on ITO (dash). Monomer **1** and **Poly-1** (a), **2** and **Poly-2** (b), and **Zn-1** and **Poly-Zn-1** (c). Normalized at the Soret. Corrected for absorbance of ITO. **Poly-Zn-1** and **Poly-2** prepared electrochemically from monomers in dichloromethane solvent with electrolyte, **Poly-1** prepared in acetonitrile solvent. See Chapter 6.2 for polymerization experimental details.

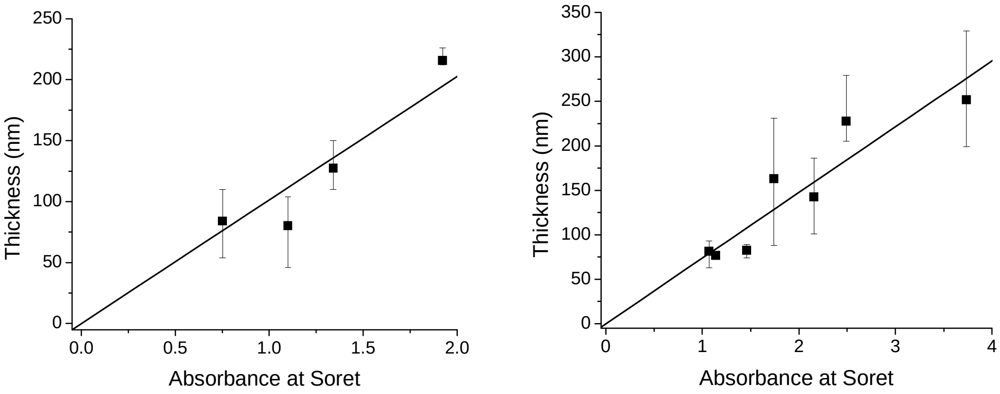

Figure 13. Polymer thickness. **Poly-1** (left) and **Poly-2** (right). Plot shows the thickness as a function of the absorbance at the polymer Soret. Regression lines are the least-squares best fit. The error bars show the range of results from multiple experiments on the same film.

Assuming that the films are uniform in their density, the absorbance should be linear with polymer film thickness. Using profilometry to determine thickness, films of **Poly-1** and **Poly-2** with various thicknesses were analyzed and plotted with their absorbance at the soret peak in Figure 13. A generally linear trend was determined as 101 nm and 74 nm per absorbance unit for **Poly-1** and **Poly-2**, respectively.[47]

2.4. Chemically Polymerized Porphyrin

2.4.1. Synthesis

In addition to electrochemical polymerization, chemical oxidative polymerization was attempted using Cu^{2+} salts as a strong oxidant. Though not known for being good oxidants, Cu^{2+} salts are good one-electron oxidizers in certain solvents,[49] and have been previously used to oxidize porphyrins[50] and polymerize aniline.[51] A more extensive discussion of Cu^{2+} as a one-electron oxidant is contained in Chapter 4.2.1.

Unlike electrochemical polymerization, chemical oxidative polymerization requires that the oxidant have the appropriate redox potential and that sufficient equivalents of oxidant are used. In the case of **Zn-1**, the oxidant must be capable of oxidizing the porphyrin and aniline substituent. In acetonitrile solvent $Cu(BF_4)_2$•6 H_2O was found to be sufficiently oxidizing. For polymerization, 3.5 equivalents of Cu^{2+} was used, a slight excess over the 3 equivalents theoretically required for full polymerization. Two equivalents are needed for each porphyrin-porphyrin coupling reaction, which ends with a non-oxidized molecule. With the polymer being easier to oxidize than the monomer, the polymer will oxidize after its formation and use another equivalent of oxidant for each coupling reaction. The metalated analogue of **1**, **Zn-1**, was used for the polymerization because it had been found to polymerize electrochemically much like **1**, and because Cu^{2+} could insert into the freebase analogue during the reaction. After polymerization, removal of the zinc ion to produce **Poly-1** was easily accomplished with trifluoroacetic acid. Attempts to repeat the reaction with the zinc-inserted analogue of dyad monomer **2** yielded an entirely insoluble product.

2.4.2. Characterization

Chemically polymerized **Poly-1** was soluble in THF and dichloromethane solvents suggesting shorter chainlengths than the relatively insoluble electrochemically polymerized **Poly-1**. HPLC-GPC analysis, experimentally described in Chapter 6.2, showed the average molecular weight to be 4343 with a polydispersity of 1.37 corresponding to an average chainlength of 6.8 porphyrin units.[52]

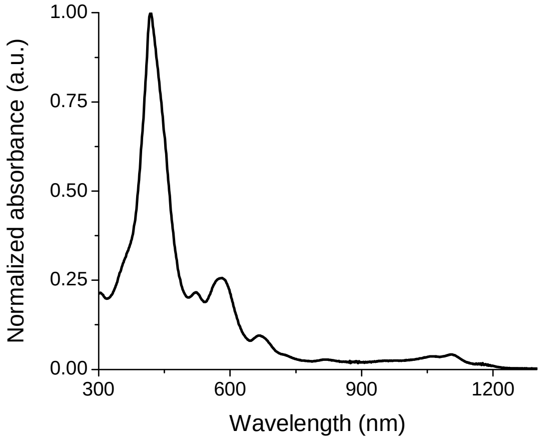

Figure 14. Absorbance spectrum of chemically polymerized **Poly-1** in THF. Absorbance values normalized at the Soret.

The absorbance spectrum of the material in THF solvent is shown in Figure 14. The spectrum in the UV-Visible spectral regions is similar to that of the electropolymerized **Poly-1** spectrum in Figure 12. However, the NIR spectral region contained a series of unknown absorbance peaks. Upon closer inspection and characterization, it was determined that a side reaction occurred in which the meso positions of the porphyrins dimerized much like a reaction described by Osuka and co-workers.[53] The side reaction has a similar radical-radical coupling as the first step, and is followed by additional couplings to form a fused porphyrin dimer, shown in Figure 15 as the freebase analogue still containing the unreacted aniline groups. Synthetic analogues of the proposed impurity show NIR absorbance peaks similar to those shown in Figure 14.[53]

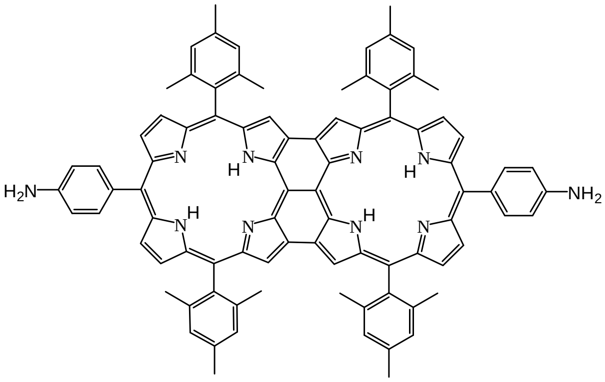

Figure 15. Porphyrin polymer impurity.

With aniline substituents capable of being oxidized for further reactions, the impurity shown in Figure 15 is capable of continuing the polymerization reaction. It is unknown whether the impurity forms and incorporates itself into the polymer, whether two polymer chains dimerize to form the impurity, or both. However, chromatography of the material on silica gel using dichloromethane eluent revealed that the impurity was indeed embedded in the polymer chains and not a separate product.

The impurity can also be seen in the NMR spectra, most obviously with characteristic peaks for the mesityl ortho and para methyl groups of similar fused porphyrins discussed in Chapter 4. Mass spectrometry was less helpful, as the impurity-containing polymer mass peaks appeared to overlap with pure polymer species due to the small difference in masses.

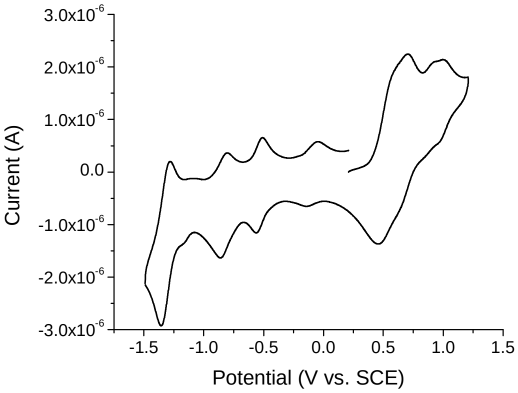

Figure 16. Electrochemistry of chemically polymerized **Poly-1**. Performed in dichloromethane with 100 mM TBAPF$_6$ salt as electrolyte. Referenced using ferrocene as internal standard and converted to SCE.

Electrochemistry was another method helpful for confirming the fused porphyrin impurity. Figure 16 shows a number of oxidation and reduction peaks for the heterogeneous **Poly-1**. Those at -0.53 V and -0.83 V vs. SCE are close to similar freebase fused porphyrin reduction peaks discussed in Chapter 4.2.4 Table 7. The reduction at -1.31 V is most similar to that seen previously from the electrochemically polymerized head-to-tail porphyrin polymer reduction at -1.0 V vs. SCE,[46] but cathodically shifted possibly due to the polymer already having been reduced at another site on the chain. On the anodic side, the broad peaks between 0.50 and 1.0 V likely contain oxidation of the head-to-tail polymer as well as the impurity. The additional peaks observed in the voltammogram could derive from the aniline substituents, the impurity, or unknown redox states formed from differences in conjugation due to the impurity.

Efforts to promote the desired polymerization by hindering the side reaction were not successful, and the adverse photophysical and electrochemical properties of the impurity inhibit the impure polymer’s use as a light-harvesting semiconductor. These properties are more thoroughly discussed in Chapter 4, and the chemically polymerized porphyrin will not be discussed further. The electrochemically prepared **Poly-1** did not appear to have an impurity seen from UV-Visible-NIR spectroscopy or electrochemical methods; however the level of characterization on the thin solid films could not match that of the soluble chemically polymerized material.

2.5. Analysis of Electrochemically Polymerized Porphyrin

2.5.1. Hole Transfer Study

The usefulness of porphyrin polymers as semiconductors is partially based on their ability to transfer charges within the polymer films. In the case of **Poly-1**, **Poly-2**, and **Poly-Zn-1**, the polymers are relatively easy to oxidize and could act as p-type semiconductors. P-type semiconductors transfer holes, or in another sense they transfer electrons between oxidized sites. Charge transfer within the porphyrin polymer films is likely via a self-exchange process where oxidized porphyrin macrocycles within the film can transfer their holes intra- or inter-chain in a diffusional process. To this end, the diffusion charge transfer coefficient (D_{CT}) of holes was studied in electrolytic solution.

In an electrolytic solution, oxidation of the polymer films requires compensating anions to penetrate the film. The porphyrin polymer films studied here have been previously shown to incorporate the relatively small anions of perchlorate and hexafluorophosphate upon polymer oxidation.[46] Whether the counterion can penetrate is important, as polymerization using cyclic voltammetry requires oxidation and reduction of the film during each voltammetric cycle to continue polymerization, with counterion incorporation required for electroneutrality. The rate at which the ions can be incorporated is also important. Ion diffusion rates can limit the overall rate of charge diffusion within a polymer, with ion size being particularly significant.[54-57] Interactions or differences in interaction between the redox states of the polymer and the electrolyte could also affect charge transfer. It is known that metal-containing porphyrins are capable of binding axial ligands, affecting porphyrin physical and electronic properties.[31]

There are multiple methods to determine D_{CT} for semiconductors. The most popular use standard 3-electrode electrochemical experiments and apply analogues of the Cottrell equation to chronocoulometric or chronoamperometric studies, or use cyclic voltammetry and apply the Randles-Sevcik equation.[56, 58-62] In the former, a potential is applied to an electrode-immobilized semiconductive material immersed in an electrolyte. The potential is stepped from a point where the material is in a particular redox state to one in which the redox state is changed. In this case, the potential is made increasingly more oxidizing thereby removing electrons from the porphyrins. Upon the change in potential, charge flows within the film to convert to the new redox state, and this process is analyzed as a function of time. The integrated analogue of the Cottrell equation shown as Equation 9 allows the rate of diffusive charge transfer within the film for the redox process to be quantified.

Integrated Cottrell equation $$Q = 2nF\mathrm{A}\mathrm{D}_{\mathrm{CT}}^{1/2}\mathrm{C}t^{1/2}\pi^{-1/2} \qquad \text{(eq. 9)}$$

Where Q is the charge in coulombs, *n* is the number of electrons involved in the redox process, *F* is the Faraday constant, D_{CT} is the charge diffusion coefficient, C is the concentration of oxidized species (mol/cm^3), and *t* is time.

Randles-Sevcik equation $i_p = 2.69\text{x}10^5 n^{3/2} \text{AD}_{CT}^{1/2} \text{C}\nu^{1/2}$ (eq. 10)

Where i_p is the peak current, A is the electrode area, *n* is the number of electrons in the redox process, C is the concentration of redox species (mol/cm^3), ν is the potential scan rate, and D_{CT} is the charge diffusion coefficient. Assumes room temperature of 298 K.

Cyclic voltammetry can also be used to determine the charge transfer coefficient. Cyclic voltammetry of surface-immobilized species results in electrical current which increases linearly with scan rate ($i \sim \nu$). However, at faster scan rates the current becomes semi-infinite diffusion limited and follows a linear increase with the square root of scan rate ($i \sim \nu^{1/2}$). With the transition to diffusion-limited response, cyclic voltammetry data can be analyzed by the Randles-Sevcik equation (Equation 10) to determine D_{CT}. The values using either Cottrell-based or cyclic voltammetric experimentation should ideally be the same. With regard to our experiments, similar values between the two experimental methods were obtained, with chronocoulometry producing the most precise and reproducible results.

Charge transfer coefficients for porphyrin polymers in electrolyte reportedly show a wide range of conductivity up to 10^{-7} cm^2 sec^{-1} for values of D_{CT}.[61-63] As a comparison, polyaniline films were reported to have a D_{CT} value of 3.6 x10^{-8} cm^2 sec^{-1} under aqueous acidic conditions.[64] Diffusion coefficients for structurally similar porphyrins can depend on the metal incorporated into the macrocycle, and differ for each redox state of the metal or porphyrin substituent.[63] Results can also differ with experimental conditions, making comparisons with literature-cited materials difficult. To allow for comparisons to p-type porphyrin polymer semiconductors, a previously characterized porphyrin polymer based on the monomer Zn-tetrakis-p-hydroxyphenyl porphyrin **3**, shown in Figure 17, was analyzed using the same methods.[42]

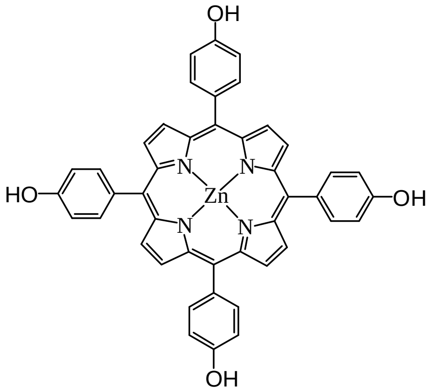

Figure 17. Zn-tetrakis-p-hydroxyphenyl porphyrin (monomer **3**)

As a strict comparison to previous literature, **Poly-3** was examined alongside **Poly-1** and **Poly-2** in a similar experiment to Savenije.[42] Cyclic voltammetry was used to polymerize the monomers. Experimental details for polymerization of each monomer are contained in Chapter 6.2. Platinum (25 μm diameter) or FTO (~0.5-1 cm^2 area) were used as substrates. Savenije used ITO electrodes of unknown area for his experiments. The thin polymer film electrodes were then subjected to cyclic voltammetry in acetonitrile solvent containing 100 mM $LiClO_4$. The CV scan rate was increased in successive cycles until no discernable polymer oxidation peak could be observed.

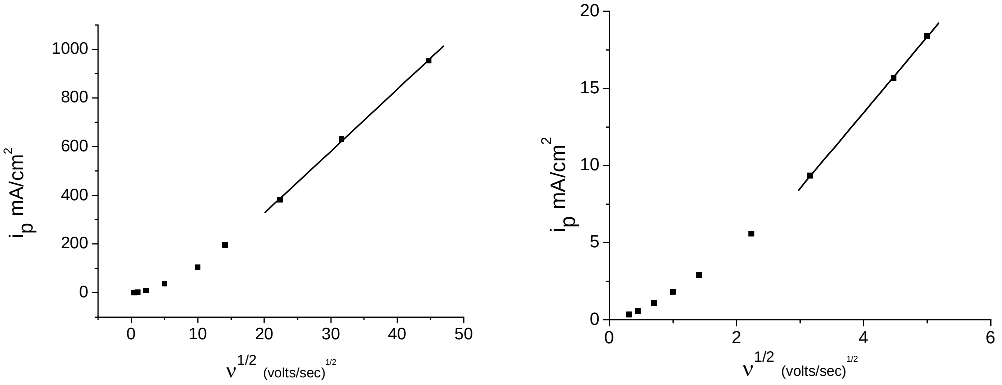

Figure 18. Current dependence on scan rate $\nu^{1/2}$. **Poly-1** on platinum (left) and on FTO (right). Peak current density from anodic peak is shown. Experiments conducted in acetonitrile with 100 mM $LiClO_4$. Best-fit linear regression lines are shown.

Results using cyclic voltammetry provide striking differences depending on the substrate. Using **Poly-1** as an example, Figure 18 shows how the peak oxidation current i_p varies as a function of the square root of the potentiometric scan rate ν. As expected, the current transitions from being linear with scan rate to being linear with $\nu^{1/2}$. However, when the slope was used to determine D_{CT}, the results were vastly different for the substrates. Using the Randles-Sevcik equation (Equation 10) and known values for the variables, the D_{CT} values were calculated in Table 1.

Table 1. Charge diffusion values from cyclic voltammetry

Polymer	D_{CT} Pt $cm^2\ sec^{-1}$	D_{CT} FTO $cm^2\ sec^{-1}$
Poly-1	1.6×10^{-9}	4.2×10^{-11}
Poly-2	5.7×10^{-9}	3.5×10^{-11}
Poly-3	2.3×10^{-8}	7.1×10^{-11}

Experiments conducted in acetonitrile with 100 mM $LiClO_4$. Values of D_{CT} determined using the Randles-Sevcik equation with n=1 for **Poly-1** and **Poly-2**, and 0.49 for **Poly-3**.[61] Densities were used to calculate polymer concentration. Density of **Poly-1** and **Poly-2** determined previously as 1.42 and 1.56 g/cm^3, respectively.[47] **Poly-3** determined previously to be 1.35 g/cm^3.[65] Relative errors for D_{CT} are ±15-50%.

The difference is thought to be due to the larger active surface of FTO (~0.5-1 cm^2) compared to the platinum microelectrode at 4.9×10^{-6} cm^2. As discussed in Chapter 1.2 with Equation 2, there is a linear drop in the applied potential with increasing current. Using the relatively small platinum microelectrode, the drop in applied potential does not become an issue even at high scan rates. However, significant compensation for such drops (iR compensation) is required for the much larger FTO electrodes due to the high currents obtained at higher scan rates. Even with iR compensation, the relatively low values for uncompensated resistance commonly obtained can cause broadening in the voltammetric spectra. This would decrease the peak current values in cyclic voltammetry and give artificially low values of D_{CT} from the Randles-Sevcik equation. Non-comprehensive testing using a 1.6 mm diameter platinum disk with iR compensation resulted in intermediate D_{CT} values between larger FTO and the platinum microelectrode (results not shown). Thus, the platinum microelectrodes give a more accurate determination of D_{CT} due to the low currents obtained during the experiments and were used for all subsequent charge mobility studies.

The results on FTO are useful, however, as they provide evidence that D_{CT} for the porphyrin reference polymer **Poly-3** is comparable to published results. The D_{CT} value of 7.1×10^{-11} cm^2 sec^{-1} for **Poly-3** on FTO is similar to the 8.5×10^{-11} cm^2 sec^{-1} initially determined by Savenije on ITO substrates.[61]

Polymer films on platinum microelectrodes were also studied using chronocoulometry. The electropolymerized films were held at an applied potential where the polymer was not oxidized, and then a more oxidizing potential was applied. The electrical charge flowing from the polymer with the change in applied potential was measured as a function of time, and then the applied potential was shifted back to its original value. The step-potential became increasingly more oxidizing with each experiment. Specific experimental details are given in Chapter 6.2.

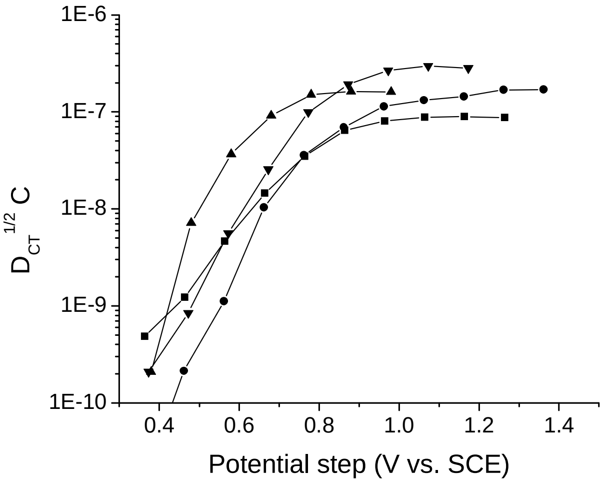

Figure 19. $D_{CT}^{1/2}C$ as a function of chronocoulometric pulse potential **Poly-1 (■)**, **Poly-2 (●)**, **Poly-Zn-1 (▲)**, and **Poly-3 (▼)**. Potential step from non-oxidized state to various potentials. Values of $D_{CT}^{1/2}$ determined using n=1 for **Poly-1**, **Poly-2**, and **Poly-Zn-1**, and 0.49 for **Poly-3**.[61] Polymers analyzed on platinum microelectrode in acetonitrile with 100 mM $LiClO_4$.

The values of $D_{CT}^{1/2}C$ for polymer oxidation in acetonitrile solvent with 100 mM $LiClO_4$ were determined at various step potentials using an integrated analogue of the Cottrell equation (Equation 9) and shown in Figure 19. As the polymer becomes increasingly oxidized, the value increases and plateaus at step potentials where the polymer would become fully oxidized. At the plateau, the concentration of oxidized polymer is equal to the concentration of polymer on the electrode and thus the D_{CT} values can be determined. Results are shown in Table 2 along with the oxidation potential at peak current from cyclic voltammetry.

Table 2. Charge diffusion values from chronocoulometry and polymer oxidation peak potentials

Polymer	$D_{CT}^{1/2}C$ mol cm^{-2} sec$^{-1/2}$	D_{CT} cm^{2} sec^{-1}	E_{ox} peak V vs. SCE
Poly-1	9.2 x10^{-8}	1.7 x10^{-9}	0.80
Poly-2	1.4 x10^{-7}	1.7 x10^{-8}	0.83
Poly-Zn-1	2.3 x10^{-7}	1.0 x10^{-8}	0.65
Poly-3	2.7 x10^{-7}	2.3 x10^{-8}	0.76

Polymer on platinum microelectrode in acetonitrile with 100 mM $LiClO_4$. Values determined from plateau $D_{CT}^{1/2}C$ values using the integrated Cottrell equation. Values of D_{CT} determined using n=1 for **Poly-1**, **Poly-2**, and **Poly-Zn-1**, and 0.49 for **Poly-3**.[61] Densities were used to calculate polymer concentration. Density of **Poly-1** and **Poly-2** determined previously as 1.42 and 1.56 g/cm^3, respectively.[47] **Poly-Zn-1** was assumed to be the same concentration as **Poly-1**. **Poly-3** determined previously to be 1.35 g/cm^3.[65] Relative errors for D_{CT} are ±1-30%.

The results of chronocoulomic testing in Table 2 revealed that the porphyrin polymers gave similar D_{CT} values to voltammetric scan rate testing (Table 1) on platinum microelectrodes. These values are in the upper range of those determined by White for metalloporphyrin polymers,[63] and similar to or higher than other semiconductive polymers based on embedded redox-active metal centers.[56, 59, 66-67]

With the relatively high charge transfer coefficients obtained, it was hypothesized that charge-compensating anion mobility might be limiting the charge transfer rate. Previous studies have shown that dried films of **Poly-1** and **Poly-2** contain only 19% and 26% free space by volume, respectively.[47] For oxidation of the polymer film, which occurs in the chronocoulometric and cyclic voltammetric experiments, each porphyrin is paired with a counterion for charge neutrality, and thus the size of the anion could play a role in a space-limited situation. In such a case, the polymer itself would be required to swell further to re-orient and accommodate the anion during the oxidation process.

The effects of anion size were tested using different salts as electrolytes in chronocoulometry experimentation using **Poly-1**. The salts employed contained anions of varying size, all larger than the ClO_4^- anion used for the polymerization process. The salts, in increasing anion size, were tetrabutylammonium p-toluenesulfonate (TBAPTS), lithium bis(trifluoromethane)sulfonamide ($LiNTf_2$), and sodium tetrakis-(3,5-bis-trifluoromethylphenyl)borate ($NaBPh_4$). For these experiments, **Poly-1** was electrochemically prepared in a method identical to previous experiments, and chronocoulometry experiments performed in acetonitrile solvent with 100 mM of the added salt.

Table 3. Charge diffusion values for **Poly-1** using chronocoulometry with various salts

electrolyte	$D_{CT}^{1/2}C$ mol cm^{-2} sec$^{-1/2}$	D_{CT} cm^{2} sec^{-1}
TBAPTS	7.0 x10^{-8}	9.8 x10^{-10}
$LiNTf_2$	1.2 x10^{-8}	2.9 x10^{-11}
$NaBPh_4$*	2.6 x10^{-9}	1.4 x10^{-12}

Polymers electrochemically grown on platinum microelectrode using $LiClO_4$ or $TBAPF_6$ salt as electrolyte. Values determined using plateau $D_{CT}^{1/2}C$ values using the integrated Cottrell equation with polymer variables provided in Table 2 caption. D_{CT} reproducibility within a factor of 2. *Values determined using a relatively thin film.

There is a general decrease in D_{CT} for **Poly-1** with increasing size of anion as shown in Table 3. With the largest anion BPh_4^-, the polymer redox peak was impossible to distinguish with thicker films, showing insulating behavior. However, when placed into a ClO_4^- solution, the polymer gave a typical CV spectrum (not shown). The value of D_{CT} for BPh_4^- shown in Table 3 should be taken as a maximum value and was determined using a relatively thin polymer film where possible pinholes were present for ion flow. Overall, the results suggest that there is an ion-related rate-limiting process involved for charge transfer upon oxidation when using counterions larger than those used for polymerization.

Additional evidence comes from a chronocoulometric study of **Poly-Zn-1** films on platinum, grown using $LiClO_4$ electrolyte, and analyzed by chronocoulometry in 100 mM $LiClO_4$ electrolyte containing 3% v/v pyridine in acetonitrile. Pyridine is able to ligate as an axial ligand to the zinc in the metalloporphyrin polymer.[68] Average values for D_{CT} were found to be 2.3×10^{-10} $cm^2\ sec^{-1}$ compared to 1.0×10^{-8} $cm^2\ sec^{-1}$ without pyridine. Assuming insignificant polymer swelling upon the added pyridine, its ligation would consume a portion of the free space between polymer chains. In so doing it could promote a diffusive ion-limiting D_{CT} value and/or it could hinder inter-chain charge-transfers by blocking porphyrin-porphyrin macrocycle stacking. In either case, the ligation of pyridine appears to decrease the charge transfer rate in **Poly-Zn-1**, suggesting that axial-bound interactions could be applied for sensor applications.

Although it was not possible to determine the exact charge diffusion coefficients of the polymers, minimum D_{CT} values of 1.7×10^{-9} $cm^2\ sec^{-1}$ for **Poly-1**, 1.7×10^{-8} $cm^2\ sec^{-1}$ for **Poly-2**, 1.0×10^{-8} $cm^2\ sec^{-1}$ for **Zn-Poly-1**, and 2.3×10^{-8} $cm^2\ sec^{-1}$ for **Poly-3** were determined when the smallest anion salt was used for characterization.

2.5.2. PEC Testing

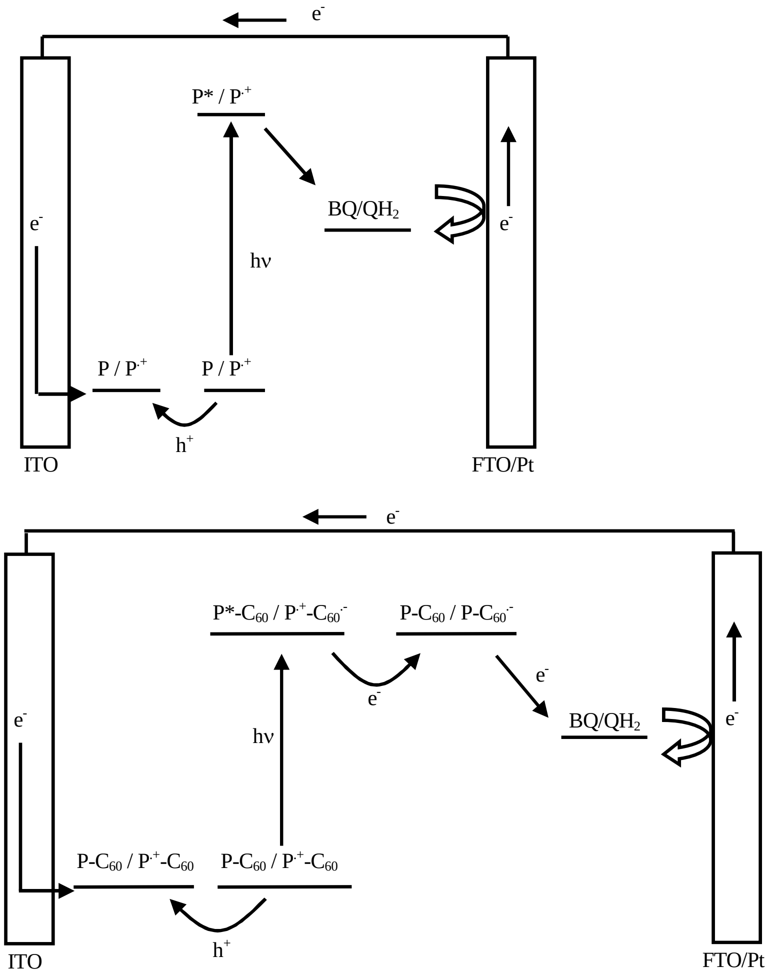

Figure 20. Porphyrin polymer PEC designs and proposed mechanism. **Poly-1** (top) and **Poly-2** (bottom). Porphyrin electropolymerized on ITO substrate. See text for details.

The semiconductive nature of the porphyrin polymers, and their ability to absorb a wide range of visible light, makes them possible candidates as the active material for planar thin film PEC. In these PEC designs, a compact film of semiconductor acts as both the light absorber and a charge carrier. In the case of **Poly-1**, the polymer can absorb light and transfer holes after charge separation with other PEC materials, producing a photocurrent. For the porphyrin-fullerene dyad

Poly-2, light absorption is followed by an efficient internal charge separation to form $P^{\cdot +}$-$C_{60}^{\cdot -}$, with both holes (h^+) and electrons (e^-) capable of diffusionally-traversing the polymer film. The PEC designs shown in Figure 20 are similar to those described in Chapter 1.1 but with photo-cathodic electron flow and with the polymer acting as both semiconductor and charge carrier. Excitation of **Poly-1** causes photo-induced electron transfer to the oxidized redox species in solution (benzoquinone BQ), with subsequent hole transfer to the ITO electrode. Photo-excited **Poly-2** undergoes an internal charge separation, with the fullerene anion able to migrate and eventually transfer an electron to BQ in solution while the porphyrin transfers the hole to the ITO electrode. Regeneration of the BQ occurs at the platinized FTO counter electrode.

Poly-1 and **Poly-2** were electrochemically grown on ITO substrates and the electrodes made into a regenerative PEC cell using platinized FTO as counter electrode as described in Chapter 6.2. Initially, an electrolyte was used which contained 150 mM tetra-*n*-butylammonium hexafluorophosphate ($TBAPF_6$) in acetonitrile with the common I_3^-/ I^- redox couple (600 mM LiI and 50 mM I_2). However it was determined that cathodic photocurrent was preferred for the PEC. This was experienced previously for porphyrin thin films by Hupp and co-workers.[69] Since no electron- or hole-blocking materials were used between electrodes, there was nothing that directed the charge flow. Cathodic photocurrent involves electrons flowing from the polymer into solution, reducing I_3^- into I^-, opposite of what normally occurs in a Grätzel-type PEC. Generally, photocurrents involve photo-excited electron injection into the attached electrode, but in this case it appeared that the photo-excited porphyrin polymer was transferring electrons into the electrolyte. Increasing the iodine content of the electrolyte would theoretically increase the photocurrents, but iodine absorbs light and is both corrosive and potentially reactive in higher concentrations. The redox couple was changed to benzoquinone (BQ) / hydroquinone (QH_2) which is more stable.

A regenerative PEC was fabricated consisting of an ITO substrate with electropolymerized **Poly-1** or **Poly-2,** and with a platinized FTO counter electrode. A solution consisting of 150 mM $TBAPF_6$ and 25 mM hydroquinone (QH_2) with various concentrations of BQ in acetonitrile was used as the PEC electrolyte. Details of PEC fabrication are contained in Chapter 6.2. The porphyrin polymer PEC was illuminated with 460 nm monochromatic light and the photocurrent obtained. With increasing concentration of BQ, the cathodic photocurrent increased as shown in Figure 21.

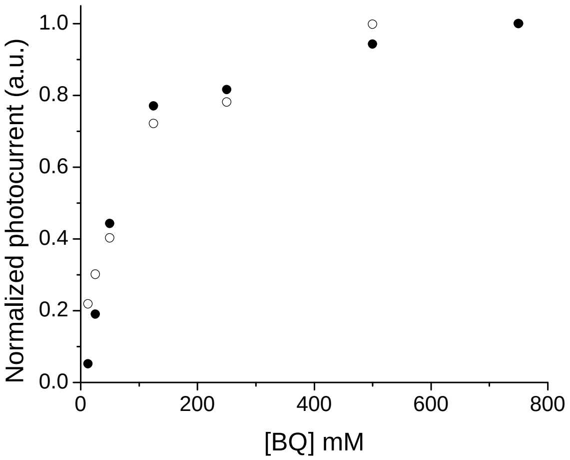

Figure 21. Photocurrent vs. [BQ] for ● **Poly-1** and ○ **Poly-2**. Electrolyte contained 150 mM TBAPF$_6$ and 25 mM QH$_2$ in acetonitrile with concentration of BQ shown on the x-axis. Photocurrent was obtained using monochromatic 460 nm polymer-side illumination and normalized to the highest photocurrent.

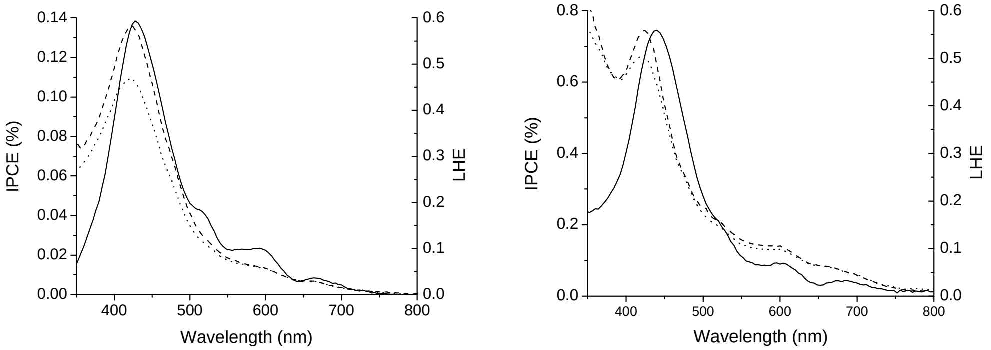

Figure 22. Polymer IPCE and LHE spectra. **Poly-1** (left) and **Poly-2** (right). IPCE using polymer-side (dots) and solution-side (dashed) illumination. Light harvesting efficiencies of electrodes (solid). LHE values determined from absorbance spectra. Photocurrent reproducible to 2% discrepancy. Electrolyte consisted of 750 mM BQ and 25 mM QH$_2$ with 150 mM TBAPF$_6$ in acetonitrile.

Photocurrents for **Poly-1** or **Poly-2** PEC were obtained at incremental monochromatic wavelengths, and used to produce the IPCE spectrum described in

Chapter 1.7.1. Experimental details are outlined in Chapter 6.2. Typical IPCE spectra along with the light harvesting efficiency spectra of **Poly-1** and **Poly-2** are shown in Figure 22. The IPCE spectra were obtained using either polymer-side illumination where the illumination direction is through the ITO/polymer towards solution, or solution-side illumination where the illumination direction is through the counter electrode and solution towards the polymer/ITO. In either case, the photocurrent generally overlaps with the absorbance features of the polymer, with a slight blue-shifting of the IPCE spectrum possibly due to slight differences between absorbance of the polymer in the solid-state, where the LHE spectrum is obtained, and in the electrolytic solution. The maximum IPCE values of ~0.14% and 0.75% for **Poly-1** and **Poly-2**, respectively, are quite low suggesting that there are barriers to efficient charge collection.

IPCE spectra using the above procedures were obtained for porphyrin polymer PECs consisting of various thickness of **Poly-1** or **Poly-2**. These thicknesses were obtained using the previously-described conversion of polymer absorbance to thickness using 101 nm and 74 nm per absorbance unit at the Soret for **Poly-1** and **Poly-2**, respectively.[47] In order to compare the energy conversion efficiencies of the samples, the internal quantum efficiencies (IQE) were determined from the IPCE value at the Soret and the Soret LHE values using Equation 6.

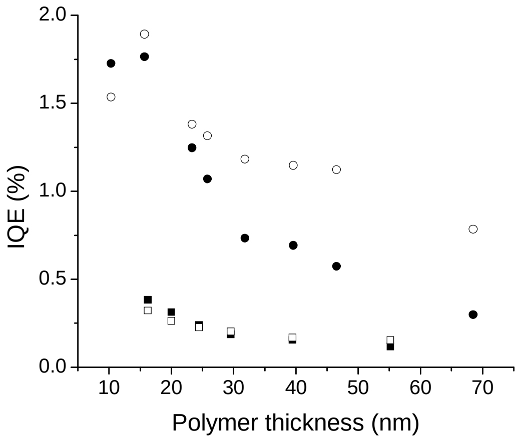

Figure 23. IQE vs. polymer thickness. **Poly-1** (squares) and **Poly-2** (circles) with Polymer-side illumination (filled) and solution-side illumination (hollow). Electrolyte consisted of 750 mM BQ and 25 mM QH_2 with 150 mM $TBAPF_6$ in acetonitrile. Internal quantum efficiency was determined from IPCE and LHE values at the Soret wavelength. Thickness determined using Soret absorbance of polymer as 101 nm and 74 nm per absorbance unit for **Poly-1** and **Poly-2,** respectively. Differences in reflectance of FTO and ITO glass taken into account by dividing initial IQE values by their transmittance.

Figure 23 plots the IQE values as a function of polymer thickness and PEC illumination direction. It should be noted that without polymer, photoanodic currents (negative values of photocurrent) was observed in the PEC, likely due to the slight absorbance of the electrolyte in the visible region. With very thin electrodes, pinholes in the polymer film likely allow for efficient electrolyte penetration to the electrode, decreasing observed photocathodic current.

Figure 23 shows a number of interesting trends. Solution-side illumination gives higher PEC charge collection efficiencies than polymer-side illumination as the polymer film gets thicker. With thinner films < 25 nm thick, the illumination pathway plays less of a role. In addition, the P-C_{60} dyad polymer **Poly-2** is generally more efficient than **Poly-1**, but both are relatively inefficient.

Taking into account the differences in reflectance of the FTO counter electrode and ITO substrate (platinized FTO reflects more light) by dividing the initial IQE values by their transmittance, there is a discrepancy in the PEC efficiency with illumination direction. This discrepancy increases as the polymer thickness increases and highlights a particular disadvantage of planar thin film polymer electrodes. Due to their compactness and relatively low surface area, excitation energy in the case of **Poly-1** or fullerene radical anions for **Poly-2** must be accessible to the electrolyte for the charge transfer to BQ to occur as shown in Figure 20. Internal relaxation of the photo-excited **Poly-1** or charge recombination between charge carriers in **Poly-2** decrease the efficiency by wasting an absorbed photon, so having a photo-excited polymer near to the polymer-electrolyte interface is ideal. When energy migration or charge migration is efficient, it does not matter where photo-excitation takes place. However, if it is inefficient then one would expect the PEC to be more efficient when a higher percentage of polymer excitation occurs near the interface. This translates to how the PEC is illuminated to produce photocurrent. If illuminated through the polymer electrode, then the polymer will absorb more of the light near that electrode and less at the polymer-electrolyte interface. If illuminated through the solution, then the polymer will start absorbing the photons at the interface. Thicker films show this discrepancy in efficiency to a greater degree.

The photo-excited polymer likely relaxes to the ground state for **Poly-1** or via charge recombination in the dyad polymer **Poly-2** before it can access the BQ in the electrolyte. The energy from the light is lost, decreasing efficiency and analogously filtering light before it can reach the polymer-electrolyte interface where the efficiency of conversion is higher.

The higher efficiency of **Poly-2** compared to **Poly-1** can likely be attributed to the ‘dyad effect.’ **Poly-2** produces a charge-separated state $P^{\cdot +}$-$C_{60}{}^{\cdot -}$ with each absorbed photon. The charges are able to move in the polymer films via self-exchange processes with neighboring porphyrin units. The hole must migrate to the ITO electrode while the electron must come into contact with the electrolytic solution where the redox couple can shuttle it to the FTO electrode. As the charges move there is a chance they will recombine either with their own countercharge or the countercharge from a different charge-separated state, decreasing the efficiency. However, the excitation energy in **Poly-1** films must come into contact with the electrolytic solution without the added mobility of a charge-separated state. The results provide evidence that the charge mobility of the dyad polymer is the likely reason for the increased efficiency.

Both **Poly-1** and **Poly-2** show very low IQE values at all thicknesses, with decreasing values as the polymer films increase in thickness. Increasing the polymer thickness increases the amount of light harvested and available for the photoelectrochemical cascade, but the absorbed photons are less likely to produce photocurrent. Decreasing the distance between the polymer and the redox species while still allowing for ample light-harvesting is possible if a high surface area active electrode could be fabricated. Using a porous wide-bandgap p-type semiconductor or fabricating a bulk-heterojunction type PEC are possible routes for future experiments aimed at increasing efficiency.[70-71]

3. SILATRANES

3.1. Introduction

A staple of many PEC devices are metal oxides, commonly used as semiconductors for transporting electrical charges. Metal oxides are a general term for a material with a bonded network of metal ions with bridging oxygens. Depending on the metal and its oxidation state, metal oxides have a range of properties, and they are easily doped with other elements.[6, 72] The surface generally terminates with a hydroxyl species that scientists have exploited to functionalize the material. When the metal oxide has a high surface area such as with nanoporous metal oxide semiconductors, surface functionalization allows for a relatively high concentration of the bonded species. This can be useful in applications such as solar cells or heterogeneous catalysis.

The general reactivity of metal oxide surface hydroxyls allows for bridging or non-bridging connections of dyes using a variety of functional groups.[73-76] The most common of these groups is carboxylate, which has been shown to form a number of ester and bridged surface linkages, two of which are shown below in Figure 24.[77-79] In the linkages, a condensation reaction between the carboxylic acid and surface hydroxyls results in the carboxylate oxygens bonded to metal ions of the particular metal oxide.

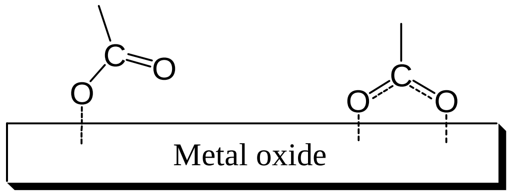

Figure 24. Carboxylate linkages on metal oxide. Bonding to the surface hydroxyl groups as mono-dentate (left) and bi-dentate (right).

Metal oxide connections constrain the orientation of the bound molecule and its distance to the metal oxide surface, characteristics that become increasingly important when well-packed monolayers are desired or when electron transfer is possible. A carboxylate bi-dentate connection on TiO_2, for example, has been theoretically and experimentally determined to lie approximately normal to the plane of the semiconductor.[80-82] Thus, due to the sp^2 hybridization of the bridging carboxylate carbon atom, a linear rigid substituent to the carboxylate would extend normal to the TiO_2 surface. This directly affects the interface distances and packing properties of the molecule on the semiconductor.

The stability of molecules on the surface depends on the strength of the surface bonding. In the case of carboxylate linkages, the bridging connection should have increased strength over the non-bridging connection due to the effects of multiple bonding. However, it is known that carboxylate connections are weak and able to readily hydrolyze in aqueous solutions when $pH > 4$.[83] In non-aqueous solutions, porphyrins containing surface carboxylate linkages can be removed from the surface in mixed solutions of chloroform and methanol. Thus, the application of derivatized metal oxides using carboxylate linkages is limited. Decreasing the susceptibility to hydrolysis is the key to broadening the usefulness of functionalized metal oxides.

A popular alternative to the carboxylate linkage is the more hydrolytically stable phosphonate. Its ester-type linkages, formed in a similar way to the carboxylate, are capable of mono-dentate, bi-dentate, and tri-dentate surface connections as seen in Figure 25.[78] Though substantially more stable than the carboxylate linkage, surface linkages to TiO_2 formed from the phosphonate functional group readily hydrolyze in aqueous solutions with pH > 7.[78, 83-84] Many applications related to biological systems would not be compatible with either carboxylate or phosphonate when neutral or slightly basic aqueous solutions are employed.

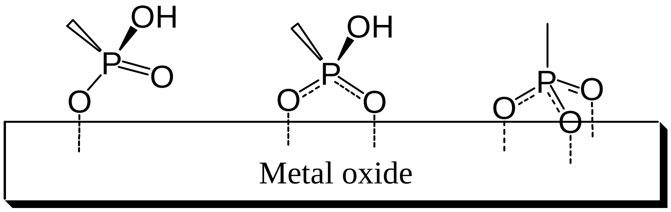

Figure 25. Phosphonate linkages on metal oxide. Bonding to the surface hydroxyl groups as mono-dentate (left), bi-dentate (middle), and tri-dentate (right).

One of the most stable surface connections readily available to researchers is bridged siloxane bonding, generally formed from reactive species such as trihalo- or trialkoxy-silanes with surface hydroxyl groups on metal oxides.[85-86] The bonding mechanism is different than the previously described carboxylate and phosphonate connections. Here, the surface hydroxyl groups displace the labile halo or alkoxy substituents. These linkages, shown in Figure 26**,** have been shown to be more stable to hydrolysis than carboxylates in aqueous solutions.[87] Furthermore, the lack of hydrolytic cleavage in the pH range 1-13 suggests them to be more stable than phosphonates as well.[88]

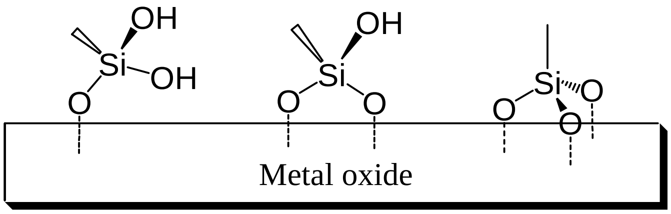

Figure 26. Siloxyl linkages on metal oxide. Bonding to the surface hydroxyl groups as mono-dentate (left), bi-dentate (middle), and tri-dentate (right).

Aminopropylsilane derivatives have historically been the most commonly used silanization reagents for attaching molecules to metal oxide surfaces. The trichloro- and trialkoxy-aminopropylsilanes have functionalized a number of different metal oxide surfaces, but used tedious preparations including anhydrous conditions and in-situ reaction sequences.[85, 89-90] In these procedures the metal oxide hydroxyl groups would first react with the silane to functionalize the surface, and later the amine appendage would undergo a separate coupling reaction, generally an amide coupling to another molecule. Post-surface modification analyses using this method are difficult because determining the surface coverage of the original silanization and then the percentage of amines reacted in the second step is tedious if not impossible. Performing the coupling reaction with the amine prior to silanization is ideal. However, the general reactivity of trihalo- and trialkoxy-silanes makes them incompatible with many synthetic procedures.

Stabilizing the silane precursor would open up new synthetic avenues and applications.

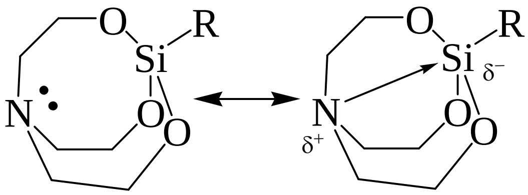

Figure 27. Silatrane structure. The substituent R can vary greatly, and affects the resonance as seen from observed Si→N bonding lengths.[91-92]

A useful synthetic method to stabilize the silanes prior to surface functionalization is to use triethanolamine as a chelating protecting group to form alkoxysilanes that resist hydrolysis.[91-92] The resulting pentacoordinate silicon functional group shown in Figure 27 is commonly called the silatrane. The silicon atom resists nucleophilic attack due to the chelate effect of the triethanolamine protecting group and because the triethanolamine nitrogen lone-pair coordinates the silicon to form an electron-rich silicon. A simplified structure will be used throughout this text.

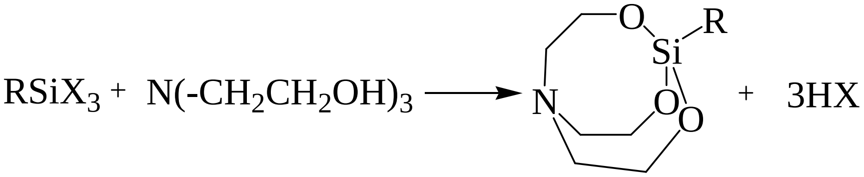

Figure 28. Synthesis of silatranes. The substituent R can vary widely while X is generally chloro or alkoxy groups.

Synthesis of silatranes generally uses trichloro- or trialkoxy-silanes with triethanolamine as shown in Figure 28.[91-92] Since many trialkoxysilanes are liquids, as is triethanolamine, the reactions can be done without solvent and with excellent yields.

With the stability of silatranes, a molecule such as aminopropylsilatrane can first react with a carboxylated molecule in an amide coupling, and the product can be purified and used later. The deprotection of the silatrane to the commonly used trihalo- or trialkoxy-silanes has not been vigorously explored; however, it was experimentally determined herein that silatranes efficiently react with the surface hydroxyl groups on nanoporous semiconducting metal oxides with mild heating in an inert solvent like toluene or acetonitrile.[76] Also, aminopropylsilatrane was previously found to react with the surface of mica in aqueous conditions.[93-94] It is hypothesized that the surface hydroxyl groups act as nucleophiles to the silicon, and due to their high concentration on the surface, are able to remove the triethanolamine protecting group by competitive bonding. The surface reaction silanizes the surface with the attached molecule with no need to deprotect the silatrane beforehand.

3.2. Results and Discussion

3.2.1. Synthesis

Silatranes were experimentally determined to resist hydrolysis to the extent that they can be purified by silica gel column chromatography. This useful feature opened a synthetic doorway and was exploited to synthesize complex silatrane molecules, some of which require this purification method. These syntheses generally involved a synthetic coupling reaction to attach a molecule with silatrane functionality onto a more complex molecule.

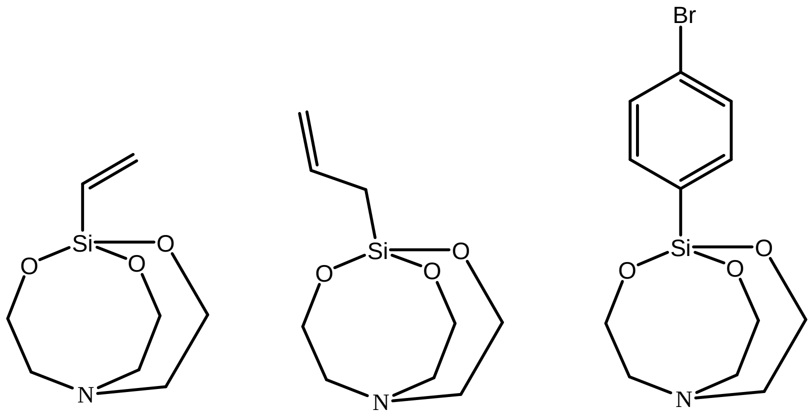

vinylsilatrane (4) allylsilatrane (5) p-bromophenylsilatrane (6)

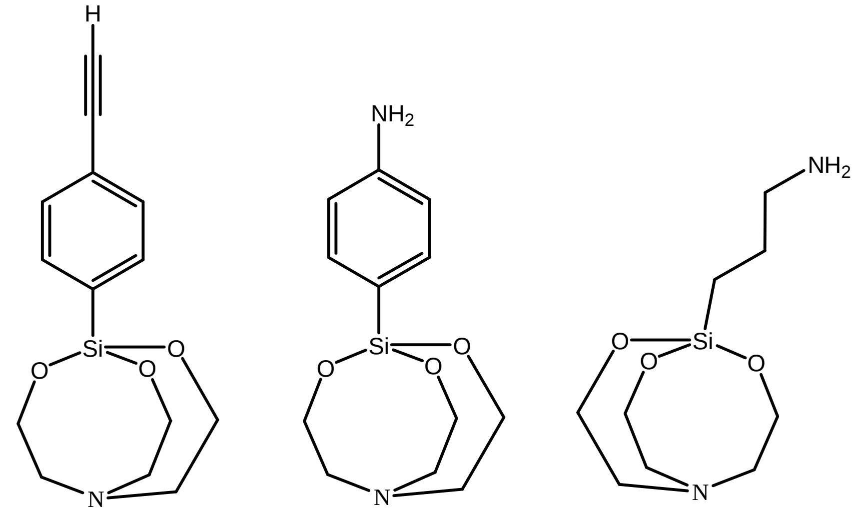

p-ethynylphenylsilatrane (8) p-aminophenylsilatrane (9) aminopropylsilatrane (10)

Figure 29. Silatranes for coupling reactions

The small molecules shown in Figure 29. were synthesized or obtained, with experimental details and characterization provided in Chapter 6.3. The silatranes are capable of undergoing further synthetic coupling reactions for attachment. Vinylsilatrane **4** was obtained from commercial sources while silatranes **5**, **6**, and **9** were synthesized from commercially available trialkoxysilane precursors. Silatrane **8** was synthesized from **6** via a Sonogashira coupling with trimethylsilylacetylene followed by deprotection. Aminopropylsilatrane **10** was previously synthesized in the laboratory from the trialkoxysilane precursor.

Vinysilatrane **4** and allylsilatrane **5** are olefins capable of undergoing reactions such as the carbon-carbon bond forming Mizoroki-Heck reaction.[95-96] p-Bromophenylsilatrane **6** can undergo a number of reactions including Suzuki-Miyaura couplings.[97] p-Ethynylphenylsilatrane **8** is capable of a number of couplings including a Sonogashira coupling.[98] Finally, p-aminophenylsilatrane **9** and aminopropylsilatrane **10** are capable of Buchwald-Hartwig reactions and amide-type coupling reactions.[99-100] These are of course a non-extensive list of the reactions suitable for the functional groups involved, but are a hint of the range of synthetic possibilities.

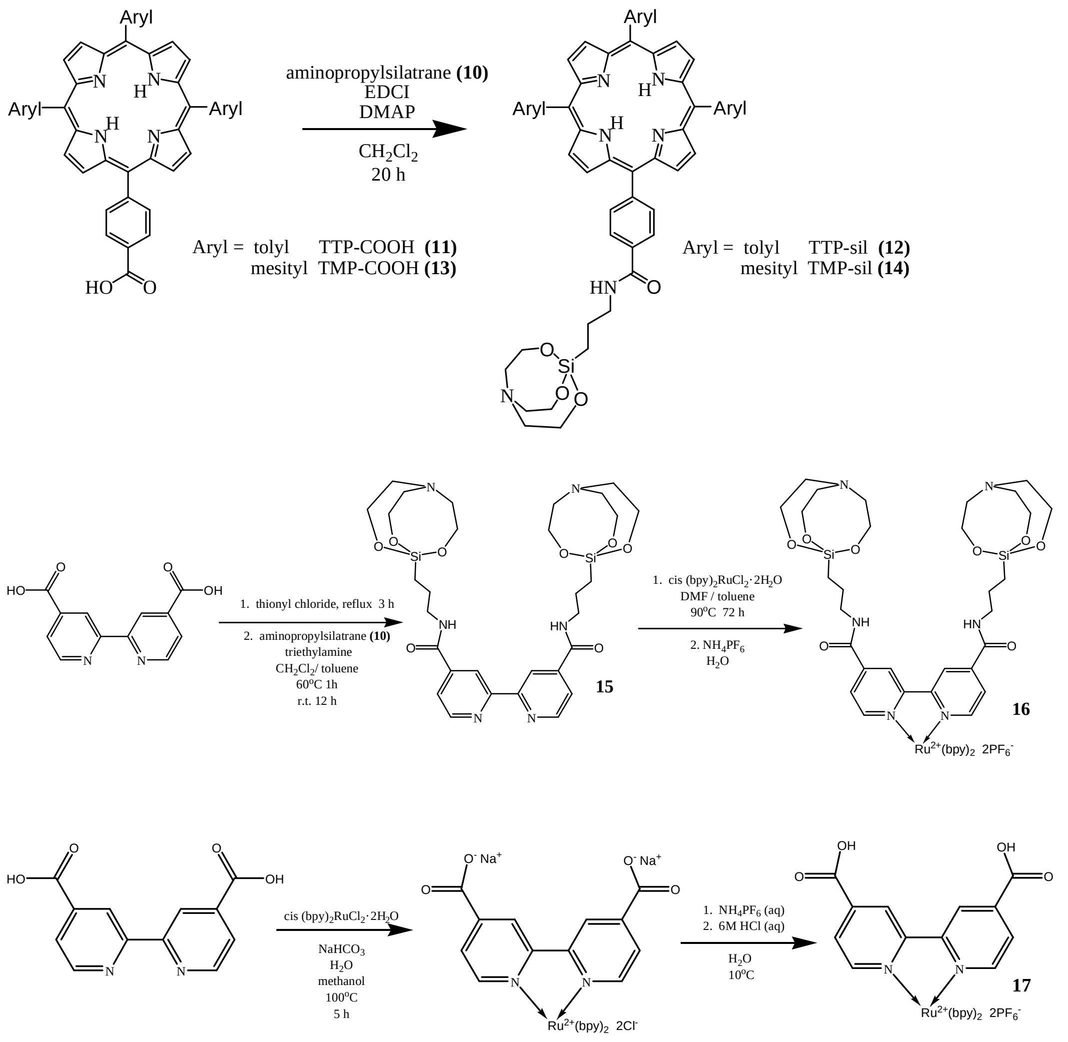

Figure 30. Silatrane and carboxylate dyes. Synthetic scheme for preparation of TTP-sil **12** and TMP-sil **14** (top), Ru(bpy)$_3$-sil **16** (middle), and Ru(bpy)$_3$-COOH **17** (bottom). Synthetic details and characterization are contained in Chapter 6.3.

To explore the stability and solar energy applications of silatranes, a number of carboxylic acid- and silatrane-functionalized dyes were synthesized for use in PEC devices. The initially synthesized molecules shown in Figure 30, based on the commonly used porphyrin macrocycle and tris-bipyridyl ruthenium complexes Ru(bpy)$_3$, were synthesized from amide couplings between aminopropylsilatrane **10** and the carboxylate features of the dyes. Experimental details and characterization are provided in Chapter 6.3. Porphyrin-silatranes TTP-sil **12** and TMP-sil **14** used *N*-(3-dimethylamino propyl)-*N′*-ethylcarbodiimide hydrochloride (EDCI) and 4-dimethylaminopyridine (DMAP) as amide coupling reagents for the reaction between the amine and carboxylic acid group. For the ruthenium-based dye, the ligand 2,2ʹ-bipyridyl-4,4ʹ-dicarboxylic acid reacted with the amine via an acyl chloride intermediate to produce **15**. This molecule was then used as the final ligand attachment to the ruthenium complex, with the final step consisting of anion metathesis from chloride to hexafluorophosphate yielding Ru(bpy)$_3$-sil **16**. The ruthenium dye functionalized with carboxylic acid **17** was synthesized using a procedure similar to Sprintschnik et al.[101]

In later work, a comparison between siloxyl linkages and the most commonly used surface linker functional groups, carboxylic acids and phosphonic acids, was performed. Zn-tetra-tolyl porphyrin analogues were synthesized containing trans-β-vinyl linkers containing carboxylic acids, phosphonic acids, or silatrane functional groups as shown in Figure 31. The porphyrins are structurally identical except for the functional group used to attach to a metal oxide surface.

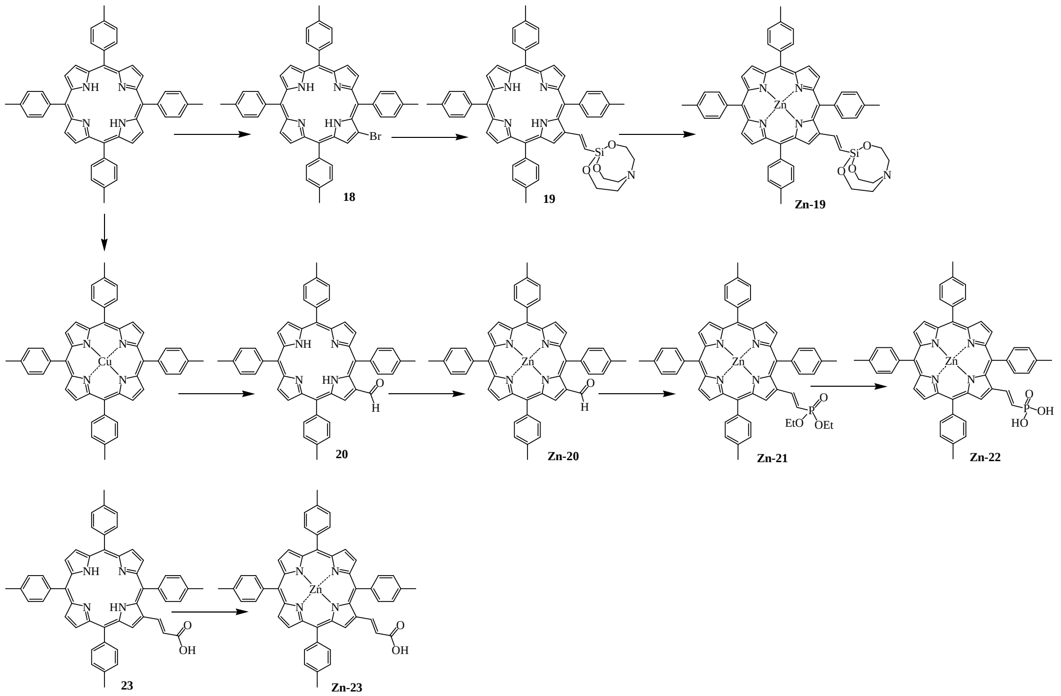

Figure 31. Porphyrin analogues with various surface linkers. See Chapter 6.3 for synthetic details and characterization.

The silatrane porphyrin **19** was synthesized using a Mizoroki-Heck reaction between vinylsilatrane **4** and β-brominated porphyrin **18**, and zinc was inserted to produce **Zn-19**. The phosphonic acid porphyrin was synthesized using a multi-step process starting with the formylation of tetra-tolylporphyrin using the Vilsmeier-Haack reaction procedure of Bonfantini et al. to produce porphyrin β-formyl-TTP **20**.[102] Zinc was inserted, and a Horner-Wadsworth-Emmons reaction was performed with tetraethylmethylene diphosphonate using sodium hydride base following a modified procedure to produce the protected phosphonic acid.[103-104] The reaction resulted in a mixture of cis and trans isomers, with only the trans isomer desired for the comparative study. Use of iodine allowed for efficient isomerization of the mixture to the trans porphyrin isomer **Zn-21**. The porphyrin was later deprotected by reaction with bromotrimethylsilane and subsequent hydrolysis to give the desired phosphonic acid porphyrin **Zn-22**. The carboxylic acid porphyrin **23** was obtained as the trans isomer and zinc inserted to produce the desired carboxylic acid porphyrin analogue **Zn-23**.

3.2.2. Carboxylic Acids vs. Amidopropylsilatrane Linkers

Initial comparisons of the silatrane-functionalized molecules TTP-sil **12**, TMP-sil **14**, and Ru(bpy)$_3$-sil **16** with similar carboxylic acid-functionalized molecules TTP-COOH **11**, TMP-COOH **13**, and Ru(bpy)$_3$-COOH **17**, were carried out in a PEC setup using nanoporous SnO_2 electrodes. Soaking the electrodes in a solution of silatrane porphyrin in toluene at 80^{o}C or Ru(bpy)$_3$-sil in acetonitrile at 80^{o}C produced an electrode with high visible light absorption. Sensitization of electrodes with carboxylic acid porphyrins used ethyl acetate solutions and Ru(bpy)$_3$-COOH used acetonitrile as solvent. Experimental details for electrode preparation and sensitization are given in Chapter 6.3. Due to the location of the structural differences between the two sets of dyes, the light-absorption characteristics for each pair of analogues are virtually identical, and only very small shifting of the absorption peaks occurs when the chromophore is bonded to the SnO_2 electrode as seen in Figure 32. In solution the porphyrin shows a typical four Q-bands in the visible region with moderate extinction coefficients and a Soret with strong intensity. The Q-bands for the two dyes TMP-COOH **13** and TMP-sil **14** nearly overlay each other on the spectrum from the electrode, while the Soret is skewed due to the high absorption and light scattering of the electrode. The porphyrin absorbance on these two electrodes is nearly equal, showing that the surface coverage is similar. The silatrane porphyrins can therefore form a monolayer on the surface similar to that of the carboxylic acid porphyrins, a positive trait if silatranes are to be used as covalent surface modifiers. Electrodes sensitized with ruthenium-based dyes gave similarly comparable electrodes.

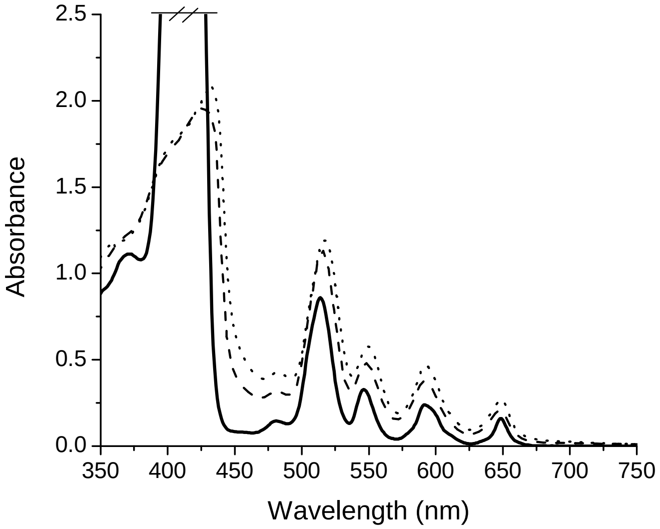

Figure 32. Absorbance spectra of TMP-sil **14** in 2-methyltetrahydrofuran solution (solid), a SnO_2 electrode derivatized with TMP-sil **14** (dashed) and a SnO_2 electrode derivatized with TMP-COOH **13** (dots). The solution spectrum Soret band absorption is truncated to highlight the Q-band region. Electrode spectra have been corrected for scatter by subtraction of the spectra of the underivatized electrodes.

Initial PEC experimentation on nanoporous TiO_2 electrodes, where there is minimal driving force for electron injection into the semiconductor conduction band, showed large discrepancies in photocurrent between the carboxylate and amidopropylsilatrane dyes suggesting electron injection issues (results not shown). The dyes were then used to sensitize SnO_2 because it is known that a larger driving force for electron injection from the photo-excited dyes into the semiconductor conduction band is present due to a more positive conduction band electrochemical potential, and therefore it would not be a major factor in the experiments.[37, 105]

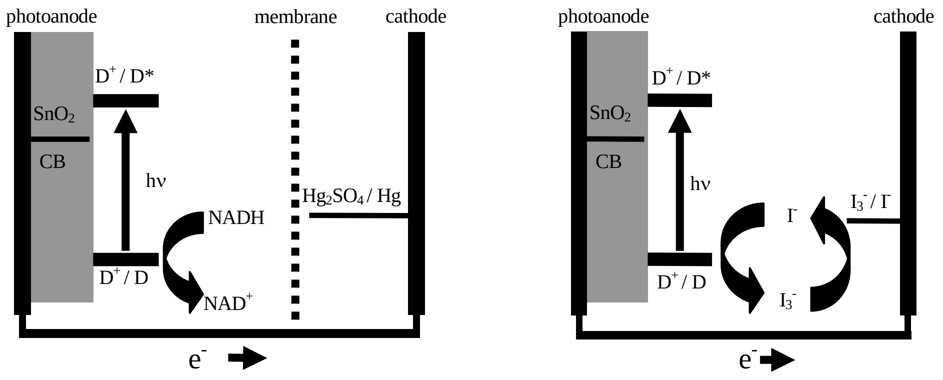

non-regenerative cell

regenerative cell

Figure 33. PEC designs. Non-regenerative (left) and regenerative design (right)

Using sensitized SnO_2 electrodes, two PEC designs were tested and compared for each dye and set of dye analogues. The design and mechanism of electron flow is shown in Figure 33. One was a non-regenerative PEC design that uses the biological molecule NADH as a sacrificial electron donor to regenerate the oxidized dye after electron injection into the semiconductor. The photoanode chamber contained an aqueous buffered solution containing 10-15 mM NADH, 250 mM N-tris(hydroxymethyl)methyl-2-aminoethane-sulfonic acid (TES) and 100 mM KCl electrolyte at pH ~7.35. The counter electrode in the cathode chamber was composed of mercury (Hg) and mercurous sulfate (Hg_2SO_4) in a saturated aqueous K_2SO_4 solution. The Hg_2SO_4/Hg redox couple has a potential of 0.4 V vs. SCE[106] and is capable of accepting electrons from SnO_2 CB (-0.24 V vs. SCE, pH 7).[105] Mercurous sulfate converts to mercury metal as electrons are shuttled to the electrode. The design allowed for continuous electron flow when irradiated with visible light. The second PEC design was a standard regenerative dye-sensitized solar cell (DSSC) using the I_3^-/I^- redox couple in an electrolyte containing 100 mM LiI, 50 mM I_2, 650 mM 1-butyl-3-methylimidazolium iodide, and 50 mM 4-*tert*-butylpyridine in an 85:15 acetonitrile:valeronitrile solvent mixture. The reduced form of the mediator regenerates at the platinized FTO counter electrode and allows for cyclic electron flow within the cell. For additional information on the PEC design, testing, and analytical procedures refer to Chapter 1 and Chapter 6.3.

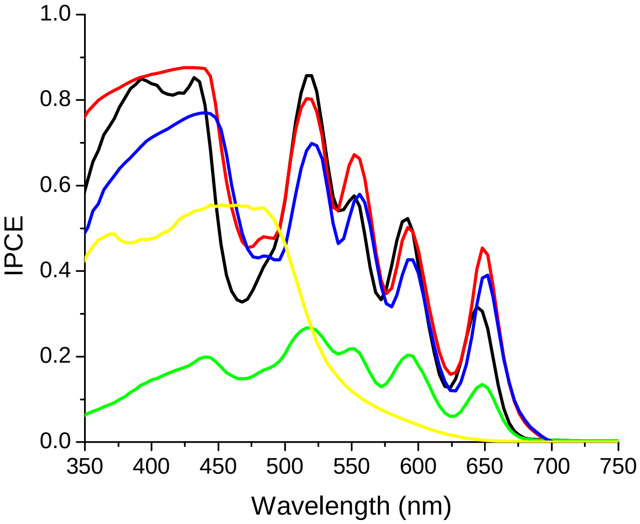

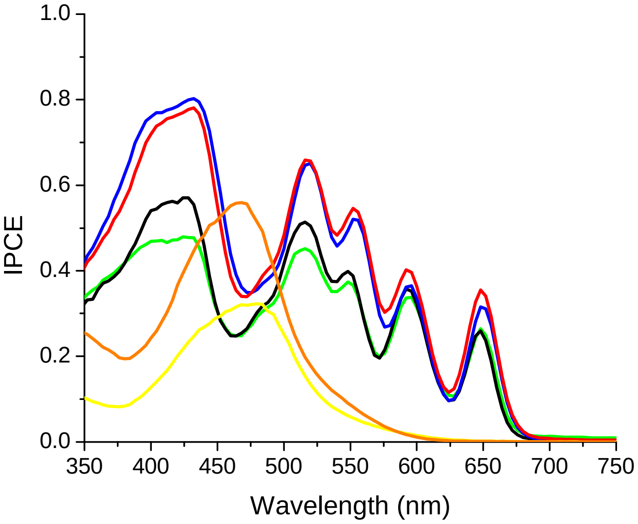

Figure 34. IPCE spectra for the non-regenerative (top) and regenerative (bottom) PEC configurations. Photoanodes were sensitized with TTP-sil **12** (red), TMP-sil **14** (black), TTP-COOH **11** (blue), TMP-COOH **13** (green), Ru(bpy)$_3$-sil **16** (yellow), or Ru(bpy)$_3$-COOH **17** (orange).

Photocurrents at incremental excitation wavelengths were converted to the incident photon to current efficiency (IPCE) for both non-regenerative and regenerative PEC designs and the IPCE traces are shown in Figure 34. As can be seen, the IPCE spectrum of TMP-sil is similar to the absorbance spectrum of that molecule shown in Figure 32.

Note that the dye Ru(bpy)$_3$-COOH **17** is not included in the non-regenerative aqueous cell IPCE spectrum in Figure 34. Due to its solubility in water and the pH of the buffer, it was leached from the electrode before any PEC experimentation could be initiated. The carboxylate bonding to the surface from the carboxylic acid porphyrins also could have hydrolyzed, however the porphyrin insolubility in water would have prevented leaching.

Table 4. Internal quantum efficiencies of dyes in PEC

Sensitizer	Internal Quantum Efficiency (IQE) [b]	
	Non-regenerative cell	Regenerative cell
TMP-sil (14)	0.86	0.59
TTP-sil (12)	0.87	0.78
Ru(bpy)$_3$-sil (16)	0.93	0.62
TMP-COOH (13)	0.26	0.46
TTP-COOH (11)	0.83	0.80
Ru(bpy)$_3$-COOH (17)	[a]	0.78

Values determined using IPCE and LHE values at the porphyrin Soret or Ru(bpy)$_3$ visible absorption peak.

[a] The Ru(bpy)$_3$-COOH desorbs from the electrode under the experimental conditions, precluding accurate determination.

[b] The relative error limits on the IQE values are +/- 5%.

Using the absorption characteristics of the sensitized electrodes, the internal quantum efficiencies (IQE) were determined using Equation 6 and are shown in Table 4. The IQE takes into account the amount of dye and the ability of each dye to absorb a photon, giving the percentage chance that each absorbed photon gives rise to an observed electron of photocurrent. The lower extinction coefficients of the ruthenium-based dyes produced electrodes with a lower overall absorbance, giving lower IPCE values than the porphyrin electrodes, but the IQE values are similar.

The IPCE spectra and IQE values show a number of trends and correlations. Overall the porphyrins and ruthenium compounds give reasonable IQE values over 0.5 with some approaching the theoretical limit of 1, with the TMP-COOH **13** dye as an outlier. The IQE values in the non-regenerative PEC are also generally higher than those of the regenerative PEC, with TMP-COOH **13** again being the outlier. This result was expected due to the removal of a major recombination pathway. As a sacrificial donor to the oxidized porphyrin, NADH undergoes degradation processes after losing an electron and its redox characteristics are therefore chemically irreversible in this experimental design.[38] The charge recombination from the semiconductor conduction band to the oxidized redox mediator does not occur due to its degradation and thus one would expect, all processes being equal, that there would be a direct increase in the IQE for the non-regenerative PEC over the regenerative type. Of course all the processes are not equal; each varying between the dyes for any number of reasons.

The difference in PEC performance for the TTP-based dyes **11** and **12** and their TMP-based analogues **13** and **14** is intriguing. Due to their similar photophysical and electrochemical properties, one would expect all the dyes to give equal IQE. However, the TTP-based dye analogues have equal or greater IQE values in each PEC design than the TMP-based dyes. In addition, the silatrane-based dyes have equal or greater IQE values than their carboxylic acid analogues.

It was hypothesized that a structural difference between the molecules could be altering their properties and affecting the PEC efficiency.

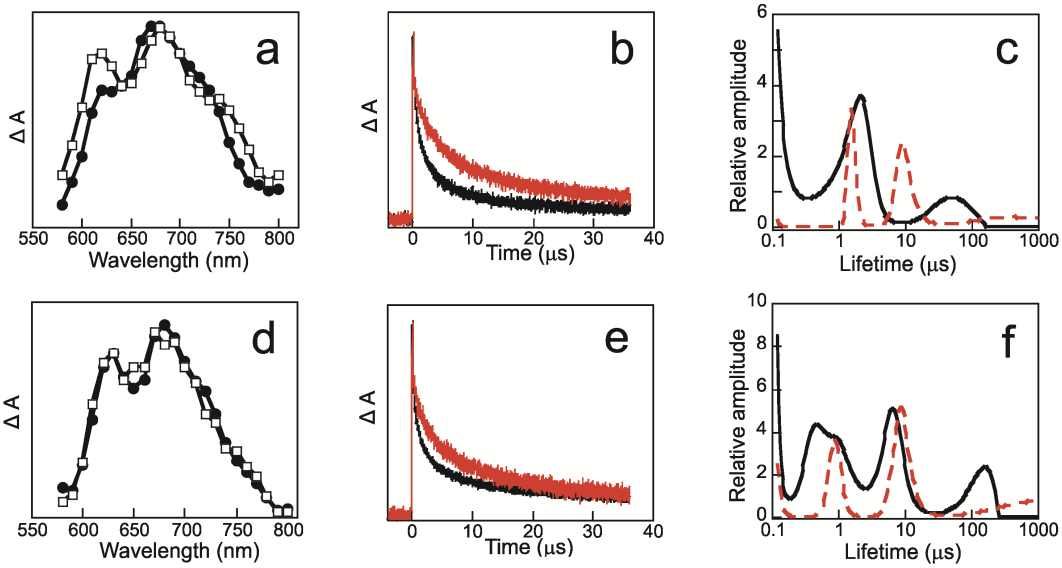

Figure 35. Transient absorption studies. Transient absorption data generated upon laser flash photolysis (515 nm, ~5 ns pulse) of SnO_2 porphyrin electrodes in borate buffer (pH = 7.35). Transient absorption spectra obtained 500 ns after excitation for (a) TMP-COOH **13** (●) and TMP-sil **14** (□) and (d) TTP-COOH **11** (●) and TTP-sil **12** (□). Decay profiles at 680 nm for (b) TMP-COOH **13** (black) and TMP-sil **14** (red) and (e) TTP-COOH **11** (black) and TTP-sil **12** (red). Lifetime distributions for exponential decay components of porphyrin radical cation absorbance at 630 nm for (c) TMP-COOH (**13**) (solid black line) and TMP-sil (**14**) (dashed red line) and (f) TTP-COOH (**11**) (solid black line) and TTP-sil (**12**) (dashed red line).

One of the processes that could limit the PEC efficiencies is recombination of the injected electrons in the semiconductor conduction band with the oxidized dye prior to regeneration of the neutral porphyrin by the reduced redox species in the electrolyte. In collaboration with Dr. Amy Keirstead, transient absorption studies of sensitized SnO_2 electrodes were performed in an inert aqueous borate buffer at pH 7.35.[76] Upon excitation of the dye on the electrode, electron injection occurred from the dye to the semiconductor, and the resulting porphyrin radical cation was studied by its absorbance. The results of this study are shown in Figure 35 with experimental details contained in Chapter 6.3. The transient spectra of the TMP and TTP-based sensitizers shown in Figure 35a and 35d, respectively, are similar to each other and typical for a tetra-arylporphyrin radical cation species.[107] This suggests that there are similar electronic properties between the carboxylate- and siloxyl surface-linked porphyrin radical cations.

However, the distance between the surface and the porphyrin macrocycle is different for the two linker systems. The decays of the porphyrin radical cation, presumably via recombination from the surface to the dye, are shown in Figure 35b and 35e. They reveal that the overall decay process is slower in the siloxyl surface-linked dyes and that it has multiple components. Analysis by the exponential series method (ESM) allowed for a more quantitative analysis of the data.[108-109] Figure 35c and 35f show the relative amplitudes of the decay components between 100 ns and 1 ms on a logarithmic scale for TMP-based dyes and TTP-based dyes, respectively. While the component clusters between 1 μs and ~500 μs vary to a small degree, there is a large difference between the carboxylate- and siloxyl surface-linked dyes on the shorter and longer timescales. Specifically, the siloxyl-linked dyes have a significantly lower degree of charge recombination than the carboxylate dyes in the 100-500 ns time frame, and they have an additional long component that extends past 1 ms. These results fit qualitatively with electron transfer theory which states that the rate of electron transfer (k) decreases exponentially with distance according to Equation 11.[110] This occurs both for photo-excited charge injection and recombination processes with porphyrin as the donor and the semiconductor as acceptor.

$$k = k_0 \exp\left[-\beta\left(R - R_0\right)\right] \qquad \text{(eq. 11)}$$

Where k_0 is the rate when the electron donor and acceptor are at van der Waals distance R_0, β is a scaler, and R is the donor-acceptor distance.

The transient spectroscopy results, along with the IQE values for the dyes, provide evidence for a number of hypotheses. First, the high IQE values for the siloxyl surface-linked dyes in the non-regenerative PEC, where the distance dependence should slow down electron injection compared to the shorter surface-linker of the carboxylate dyes, suggests that the inefficiencies lie elsewhere in the system. Secondly, the porphyrin siloxyl surface-linked dyes have slower semiconductor-to-porphyrin recombination, allowing more time for the redox molecule to reduce the porphyrin radical cation to the ground state. Thirdly, the differences in IQE values between the TMP- and TTP-based dyes are not based on a difference in the lifetime of the porphyrin radical cation. It is possible that the ortho methyl groups of the mesityl groups on the TMP-based dyes provide steric hindrance for the redox molecule from the PEC electrolyte to transfer an electron to the oxidized porphyrin. If so, it would be accentuated, as it is, in the non-regenerative cell because of the bulkiness of the electron donor NADH molecule as shown in Figure 36.

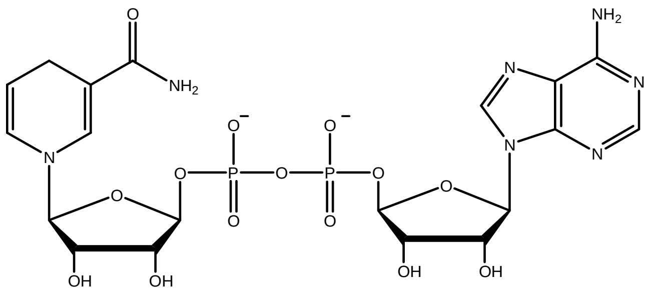

Figure 36. NADH structure

The comparisons with the ruthenium-based dyes did not give a complete picture due to the inability of Ru(bpy)$_3$-COOH **17** to stay bonded to the surface of the electrode in aqueous buffer. However, the fact that Ru(bpy)$_3$-sil **16** both stays on the electrode and works with high efficiency in the non-regenerative PEC (IQE 0.93) demonstrates that silatranes can have useful applications with water-soluble dyes. Most water-soluble dyes currently available cannot be used as photosensitizers due to their unstable connections to metal oxides in neutral to basic pH aqueous solutions. The differences in efficiency between Ru(bpy)$_3$-sil **16** and Ru(bpy)$_3$-COOH **17** in the regenerative PEC, where the carboxylic acid analogue had a much higher IQE (0.78 vs. 0.62), are difficult to explain without a more detailed study.

Overall, the comparison of dyes gave a number of conclusions. The analysis of the IQE values in Table 4 show that TTP-based dyes work more efficiently than the TMP-based analogues in PEC, and the transient absorption studies suggest that this trend isn’t due to a difference in rates of recombination. The transient absorption study also confirms, from the increased porphyrin radical cation lifetime, that an increased distance from the surface to the dye in the siloxyl-linked porphyrins slows down recombination from the semiconductor to the oxidized porphyrin. This is likely the reason for the increased IQE values for the siloxyl surface-linked porphyrins over the carboxylic acid analogues. Finally, it was shown that Ru(bpy)$_3$-COOH **17** desorbed from the surface into the buffer solution while Ru(bpy)$_3$-sil **16** was stable, providing a new route to using water-soluble dyes on metal oxide electrodes in aqueous solutions by functionalizing them with silatrane moieties.

3.2.3. Porphyrin Dyes with Different Surface Linkers

In the above study, a direct comparison of the linkers was not possible due to surface-to-dye distance and structural variability between the linker moieties. A more ideal comparison would be one among dyes with only the surface linker functional group as the structural difference. For that reason, Zn-tetra-tolyl-porphyrin-based dyes were synthesized containing functionalized *trans*-β-vinyl substituents with silatrane **Zn-19**, phosphonic acid **Zn-22**, or carboxylic acid **Zn-23**.

The porphyrins were studied using a variety of analytical techniques to determine their relevant properties, and then tested in a regenerative PEC design on TiO_2 electrodes to determine their performance differences. Finally, the stability of the porphyrins on the electrodes was determined by attempting to leach off the dyes under alkaline conditions.

The porphyrin absorbance, fluorescence, and electrochemical properties were examined and compared. Due to issues that arise from coordination of the porphyrinic zinc to the carboxylate and phosphonate porphyrins, the esterified molecules were used for experimentations in solution. No significant differences are expected for the esterified porphyrins over the porphyrins used to sensitize the electrodes.

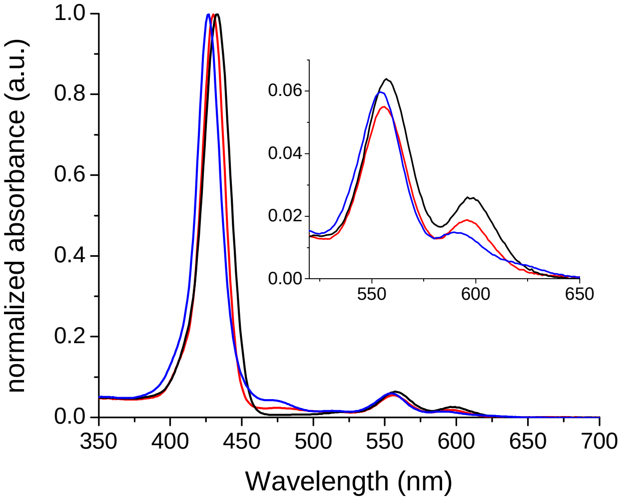

Figure 37. Absorbance spectra of porphyrins. Zn-TTP-COOMe **Zn-24** (black), Zn-TTP-diethyl phosphonate **Zn-21** (red), and Zn-TTP-sil **Zn-19** (blue). Experiments performed in dichloromethane solvent and normalized at the Soret band. Inset shows a comparison of the Q-band region.

The UV-Vis absorbance profiles shown in Figure 37 suggest that the porphyrins have generally similar features. Only minor shifts and discrepancies are observed between them. Zn-TTP-COOMe **Zn-24** has the most red-absorbing bands at 433 nm for the Soret, and 557 and 598 nm for the Q-bands. The Zn-TTP-diethyl phosphonate **Zn-21** absorptions are slightly shifted to the blue at 430, 556, and 596 nm, while Zn-TTP-sil **Zn-19** has the most blue-shifted bands at 427, 554, and 590 nm. The fluorescence of the porphyrins in Figure 38 affirms that the porphyrins have similar spectroscopic properties.

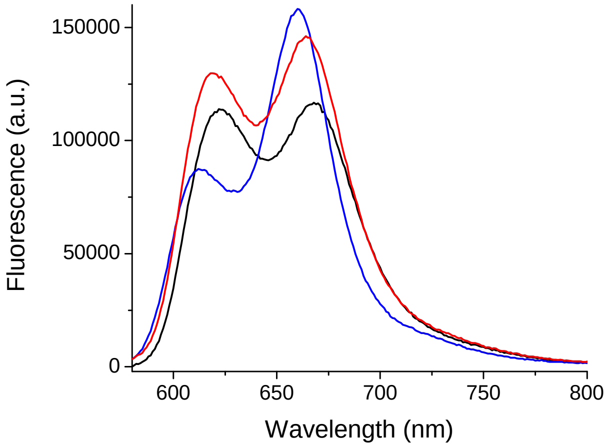

Figure 38. Fluorescence spectra of porphyrins. Zn-TTP-COOMe **Zn-24** (black), Zn-TTP-diethyl phosphonate **Zn-21** (red), and Zn-TTP-sil **Zn-19** (blue). Experiment performed in dichloromethane solvent. Excitation of the porphyrin at wavelengths with absorbance values ~0.05.

Table 5. Electrochemistry of porphyrins

Porphyrin	Electrochemistry (V vs. SCE)	
	$E_{ox\ 1}$	$E_{red\ 1}$
Zn-TTP-COOMe (Zn-24)	0.83	-1.23
Zn-TTP-diethyl phosphonate (Zn-21)	0.73	-1.26
Zn-TTP-sil (Zn-19)	0.75	-1.37

Electrochemistry performed in dichloromethane containing 100 mM $TBAPF_6$ electrolyte with ferrocene as internal reference.

The electrochemical properties were also examined and are shown in Table 5. The oxidation potential is the most important, as the oxidized porphyrin is the active species in the PEC after electron injection. Comparing the porphyrins, the range in oxidation and reduction potential differences are >100 mV. Because the porphyrins were examined in a regenerative PEC with the I_3^- / I^- redox couple, the differences in oxidation potential are negligible in the experimental design. For all three porphyrins, a significant driving force exists for the porphyrin radical cation to oxidize iodide (at 0.02 V vs. SCE),[111] and thus the differences in porphyrin oxidation potentials are small relative to the driving force for the reaction with I^-.

From the porphyrin oxidation and excited singlet-state energy values, the singlet excited-state redox potentials can be calculated using Equation 1 described in Chapter 1.1. The values for Zn-TTP-COOMe **Zn-24**, Zn-TTP-diethyl phosphonate **Zn-21**, and Zn-TTP-sil **Zn-19** are -1.20, -1.31, and -1.32 V vs. SCE respectively. With the conduction band of TiO_2 beginning at ~ -0.90 V vs. SCE,[7] there is ample driving force for electron injection from the singlet excited-state. Overall, the porphyrin properties suggest that they should act similarly in a PEC unless the surface connection plays a role.

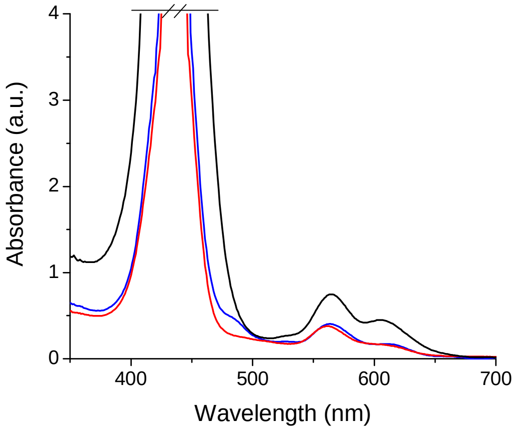

Figure 39. Absorbance spectra of porphyrins on TiO_2. Zn-TTP-COOH **Zn-23** (black), Zn-TTP-PO_3H_2 **Zn-22** (red), and Zn-TTP-sil **Zn-19** (blue). Spectra of the bare TiO_2 electrodes were subtracted from the sensitized electrodes. The Soret was truncated to highlight the Q-band region.

Nanoporous TiO_2 semiconductive electrodes were sensitized with Zn-TTP-COOH **Zn-23**, Zn-TTP-PO_3H_2 **Zn-22**, or Zn-TTP-sil **Zn-19** by soaking in ~0.2

mM porphyrin solutions in toluene at 90°C for 1 h. Details are provided in Chapter 6.3. Typical spectra for the porphyrin sensitizer on the TiO_2 electrodes are shown in Figure 39. The spectra of the porphyrins on the electrode are similar to those in solution, with slight red-shifting of the peaks. As can be seen in Figure 39, the high surface area of the electrodes allows for high absorbance values. Virtually all the light is absorbed surrounding the Soret wavelength, with significant absorbance throughout the visible spectrum.

What also can be seen in Figure 39 is a discrepancy in absorbance between electrodes with Zn-TTP-COOH **Zn-23** and those with either Zn-TTP-PO_3H_2 **Zn-22** or Zn-TTP-sil **Zn-19**, with the carboxylate surface-linked porphyrin having nearly double the absorbance values. This reproducible difference on TiO_2 electrodes of similar thicknesses and surface areas demonstrates that there are differences among the surface coverages of those porphyrins. Due to the similarity of the molecules, the most logical explanation for such a difference would involve the surface linkage. In the case of the carboxylate connections, there is a maximum of two surface bonds per molecule, while the phosphonate- and siloxyl-linked dyes can have up to three bonds. If three bonds are used, the surface might be able to accommodate fewer dyes on the surface than if two surface bonds form. However, that assumes that the surface binding sites are limiting the amount of dye coverage. For these porphyrins, the macrocycle and aromatic substituents make the molecule large and bulky, with the surface linkage covering a relatively small area in relation to the rest of the molecule. In addition, studies have shown that carboxylic acids generally bind to TiO_2 using the bi-dentate linkage, while phosphonic acids and silanes generally prefer bi-dentate over tri-dentate linkages.[77-78, 85, 112-115]

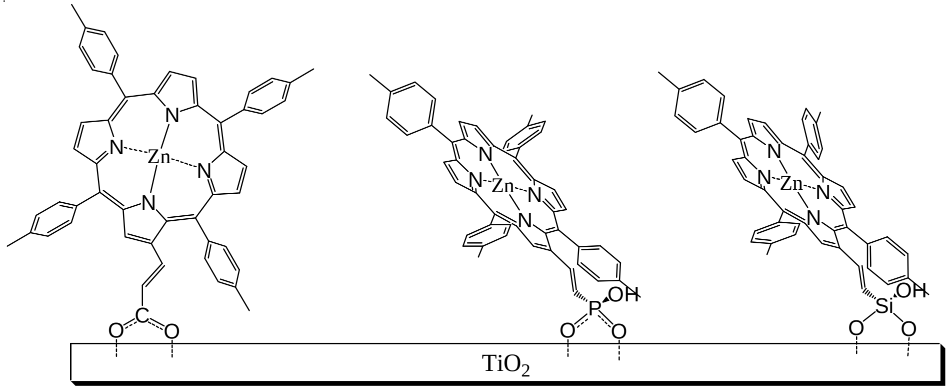

Figure 40. Surface bonding hypothesis. General representations of the proposed most common surface bonding schemes for the dyes Zn-TTP-COOH **Zn-23** (left), Zn-TTP-PO_3H_2 **Zn-22**, and Zn-TTP-sil **Zn-19** on TiO_2 electrodes.

It cannot be assumed that the porphyrins lie normal to the surface of the semiconductor after bonding. The dyes are relatively rigid molecules, and cannot contort to pack into an ideal monolayer. Each type of surface connection for the linker functional groups has a stereochemistry that must be maintained. Referring back to the bonding types of the carboxylic acids, phosphonic acids, and silanes in Figure 24, Figure 25, and Figure 26, respectively, one can see a similarity between the phosphonate and silane linkers compared to the carboxylate. The carboxylate bi-dentate connection uses a bridging carbon that is sp^2 hybridized, allowing a rigid molecule to extend normal to the plane of the semiconductor surface. This would allow for the least steric hindrance and thus the greatest potential for an efficiently packed porphyrin monolayer. The phosphonic acid and silane, on the other hand, are tetrahedral in nature, making tri-dentate connection the only linkage where the rigid porphyrin would be normal to the semiconductor plane. The proposed surface linkages are represented in Figure 40. In the bi-dentate phosphonate and siloxyl connections, the porphyrin would be angled to the surface, creating a surface steric barrier for space-limited porphyrin monolayer formation. If the phosphonic acid and silatrane porphyrins are bonding to the surface using similar geometry, one would expect a similar concentration of dye on the surface such as was observed. However, additional analyses such as IR spectroscopy would be needed to verify how the dyes are linking to the surface.[14, 77-79, 112-113, 116-120]

An additional hypothesis is that for the carboxylate, the surface binding reactions are reversible processes and that the monolayer is formed from a series of binding and un-binding events, culminating in the observed surface concentration.

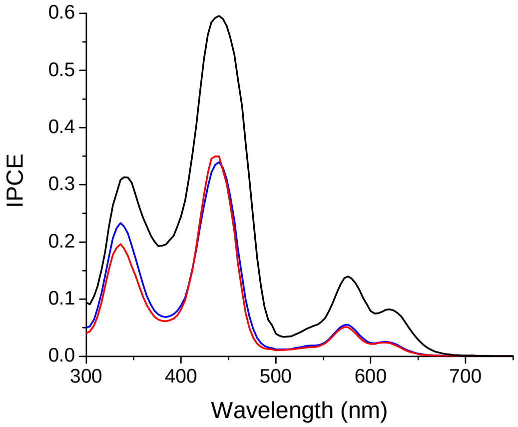

Figure 41. IPCE of porphyrins comparing surface linkage. Zn-TTP-COOH **Zn-23** (black), Zn-TTP-PO_3H_2 **Zn-22** (red), and Zn-TTP-sil **Zn-19** (blue) on TiO_2 electrodes. Electrolyte consisted of 100 mM LiI, 50 mM I_2, 650 mM 1-butyl-3-methylimidazolium iodide, and 50 mM 4-*tert*-butylpyridine in a 85:15 acetonitrile:valeronitrile solvent mixture.

The dye-sensitized TiO_2 electrodes were used to prepare regenerative DSSC-type PECs as described in Chapter 6.3. The PEC performance for each dye on TiO_2 electrodes are revealed in the IPCE spectra in Figure 41. The IPCE spectra generally match the absorbance spectra, with the phosphonate and silatrane having similar values to each other but lower values than the carboxylate. This difference appears to be related to the amount of dye on the surface, suggesting that the photocurrent is related to the dye surface coverage. However, the IQE values are not consistent across the wavelength spectrum. For all the dyes, the LHE around the Soret wavelength is nearly unity, and thus all the light around these wavelengths is absorbed. Additional dye would not have an effect on this value because the light would be absorbed before penetrating the entire electrode. Due to the LHE around unity at the Soret wavelength, the IPCE value at that wavelength should equate to the IQE according to Equation 6. The IQE value at the Soret wavelength for Zn-TTP-COOH **Zn-23** is 0.60 while those of the phosphonate and silatrane analogues are 0.35 and 0.34, respectively. In the visible region, the IQE values obtained from Equation 6 using the LHE and IPCE at the porphyrin Q-band (~580 nm) gives lower numbers of 0.19 for carboxylate-linked and 0.11 for phosphonate and siloxyl-linked porphyrins. The reproducible variance could be an effect of light scattering within the electrode or could be a positive effect of increased concentration of surface-linked carboxylic acid porphyrin compared to the other dyes. With increased porphyrin concentration and illumination of the electrode through the TiO_2 film comes two advantages. One is that there is less exposed TiO_2 surface area where recombination between electrons and the I_3^- can occur. The second is that due to the relatively high extinction coefficient of the porphyrin Soret, more light is absorbed by porphyrins closer to the conductive FTO electrode and thus injected electrons have a decreased distance to travel by charge migration through the TiO_2 conduction band. More experiments varying surface concentration and TiO_2 thickness would be needed to verify the discrepancy.

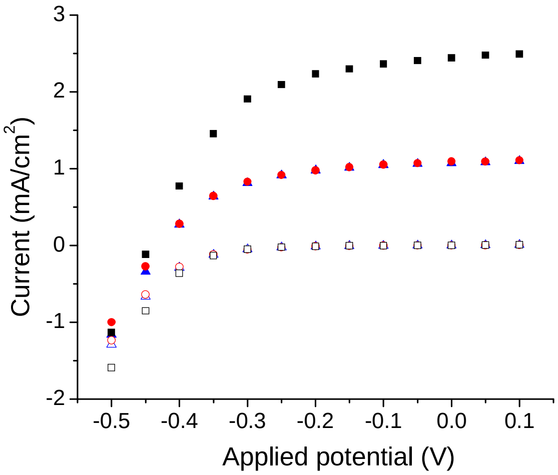

Figure 42. Current-voltage curve. Zn-TTP-COOH **Zn-23** (squares), Zn-TTP-PO_3H_2 **Zn-22** (circles), and Zn-TTP-sil **Zn-19** (triangles) on TiO_2 electrodes. Filled shapes are results under simulated AM1.5G illumination at 1000 W/m^2 and hollow shapes are results in the dark. Electrolyte consisted of 100 mM LiI, 50 mM I_2, 650 mM 1-butyl-3-methylimidazolium iodide, and 50 mM 4-*tert*-butylpyridine in a 85:15 acetonitrile:valeronitrile solvent mixture.

Overall, the evidence demonstrates that similar dyes with different surface linkers have photocurrents that correspond to the surface concentration of dye, and that the silatrane and phosphonic acid analogues perform nearly identically in the regenerative PEC. This was confirmed when the electrodes were tested under simulated AM1.5G sunlight as shown in Figure 42. Illuminated and under electrical load, the PECs gave slowly decreasing current as the applied voltage increased until near the V_{oc}. Under forward bias, where the applied voltage promotes photocurrent flow, there was little to no change in the photocurrent, suggesting that it does not affect the internal efficiency of the system. In the dark, the current-voltage data were typical for an n-type semiconductor. The results of the PEC current-voltage measurements are in Table 6. The carboxylic acid dye shows J_{sc} ~2.49 mA/cm^2 while the phosphonic acid and silatrane analogues were 1.11 and 1.10 mA/cm^2 respectively. The V_{oc} was fairly consistent, as expected, at 444 mV for the carboxylate surface-linked, 426 mV for the phosphonate-linked, and 423 mV for the siloxyl-linked analogues. With similar fill factors, the efficiencies of the dyes on TiO_2 under AM1.5G simulated sunlight are consistent with the differences in the observed photocurrent in the IPCE spectra. Overall, the efficiency (η) of the PEC is quite low in comparison to published data.[36] However no attempts were made to produce the most efficient solar cell, only to provide a good comparison with reproducible data using a simple PEC design.

Table 6. Current-voltage analysis

Porphyrin	J_{sc} mA/cm^2	V_{oc} mV	FF	η %
Zn-TTP-COOH (Zn-23)	2.49	444	0.52	0.57
Zn-TTP-PO_3H_2 (Zn-22)	1.11	426	0.53	0.25
Zn-TTP-sil (Zn-19)	1.10	423	0.53	0.25

Illumination under 1000 W/m^2 simulated AM1.5G sunlight. Electrolyte consisted of 100 mM LiI, 50 mM I_2, 650 mM 1-butyl-3-methyl imidazolium iodide, and 50 mM 4-*tert*-butylpyridine in a 85:15 acetonitrile:valeronitrile solvent mixture.

The dyes appear to be generally equal in their inherent efficiencies in the regenerative PEC setup, with the carboxylic acid porphyrin having higher photocurrent due to effects of the increased concentration of dye on the surface. The combined results suggest that all other aspects tied to the PEC efficiencies such as electron injection, recombination rates, and differences in dye oxidation potentials do not appear to have a strong influence, and thus the similar dyes were good models for comparison. More extensive experiments would be needed to verify such arguments.

3.2.4. Leaching Study

The stabilities of carboxylic acid, phosphonic acid, and silatrane derivatives bonded to TiO_2 electrodes were studied in alkaline conditions. Because Zn-TTP-COOH **Zn-23**, Zn-TTP-PO_3H_2 **Zn-22**, and Zn-TTP-sil **Zn-19** are not water soluble, the general stability of the porphyrin dyes was tested in a mixed organic/aqueous solvent system. TiO_2 electrodes were sensitized by soaking in ~0.2 mM porphyrin solutions in toluene at $90^{o}C$ for 1 h, and rinsed with toluene and acetonitrile. They were then soaked for 20 minutes in a solution containing THF, methanol, and an aqueous basic solution containing 0.5% Cs_2CO_3 (w/w) in a ratio 10:5:2, and then rinsed. See Chapter 6.3 for experimental details. The porphyrins are soluble in the solvent mixture and so could desorb from the surface. UV-Visible spectroscopy was used to determine the amount of porphyrin still on the surface after the experiment.

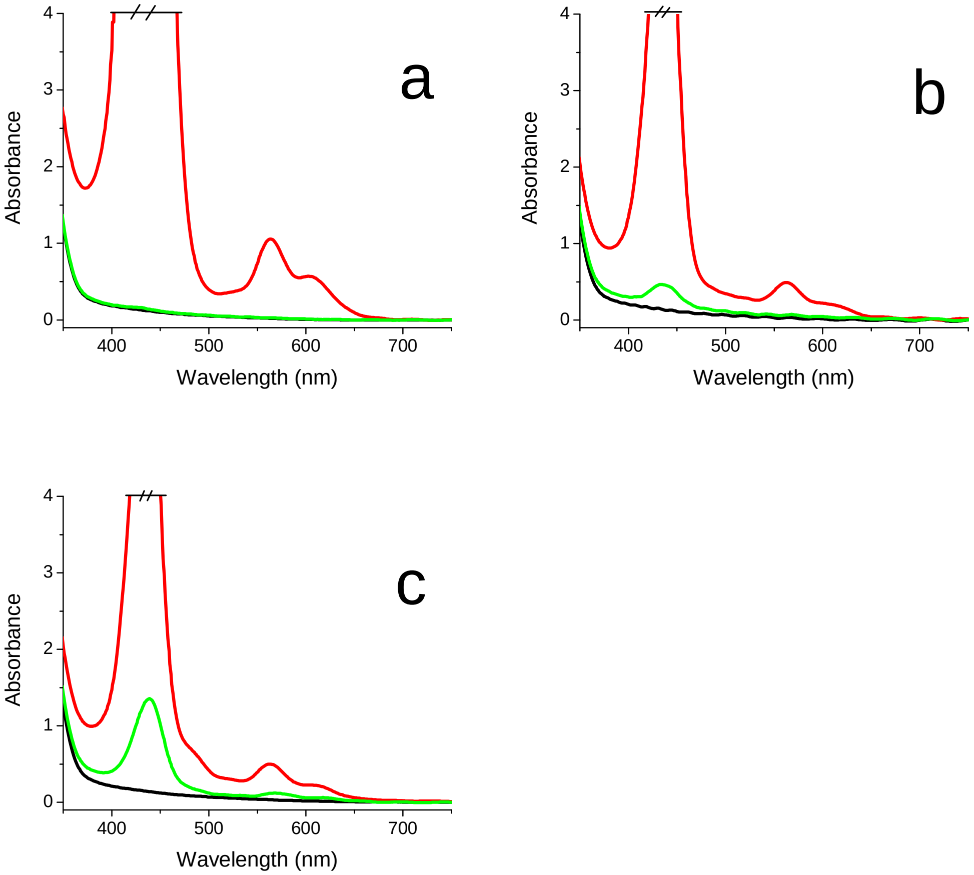

Figure 43. Porphyrin leaching. Zn-TTP-COOH **Zn-23** (a), Zn-TTP-PO_3H_2 **Zn-22** (b), and Zn-TTP-sil **Zn-19** (c). Absorbance spectra of bare TiO_2 (black), sensitized electrode (red), and electrode after leaching (green). The Soret was truncated to highlight the Q-band region.

After leaching, a noticeable decrease in the dye absorbance on the electrode was observed as shown in Figure 43, corresponding to the decrease in surface concentration of dye. Slight shifting of the spectra occurred, likely due to a change in the solvent system the porphyrins were exposed to for adsorption and leaching. The carboxylate-linked dye completely desorbed while the phosphonate-linked dye mostly desorbed and the siloxyl-linked analogue desorbed to a lesser extent. No porphyrin was completely stable under the experimental conditions, but the results show a stability trend of siloxyl > phosphonate > carboxylate.

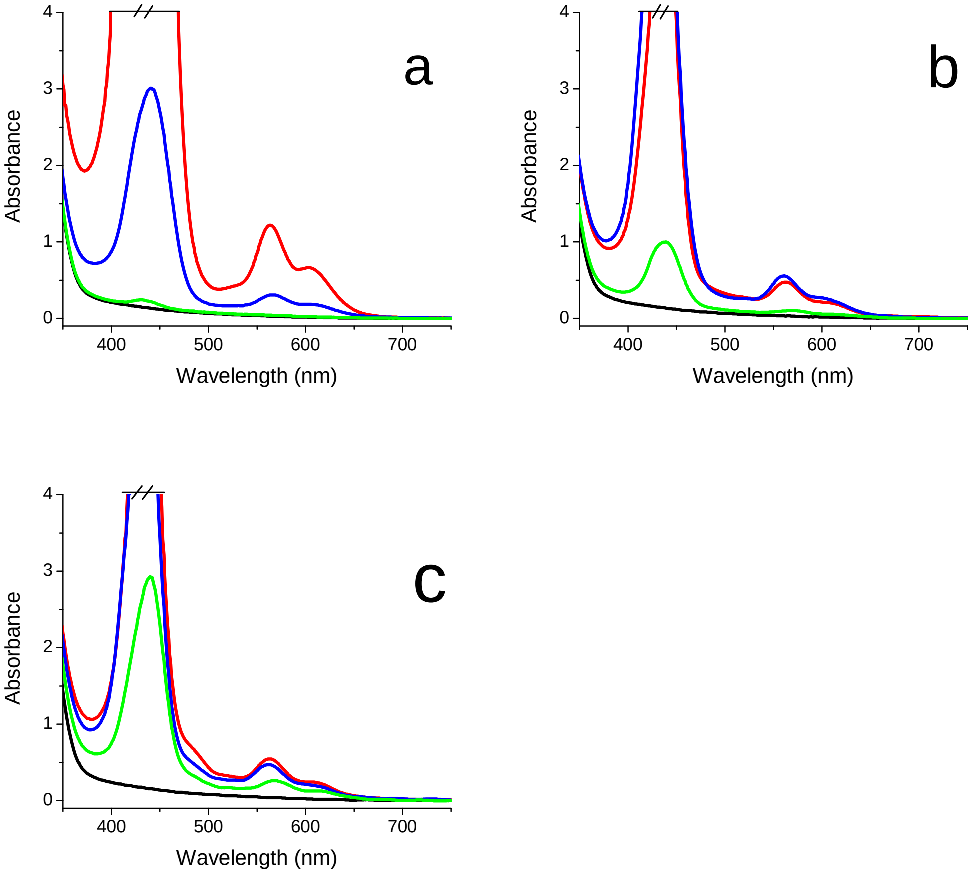

Figure 44. Porphyrin leaching after curing. Zn-TTP-COOH **Zn-23** (a), Zn-TTP-PO_3H_2 **Zn-22** (b), and Zn-TTP-sil **Zn-19** (c). Absorbance spectra of bare TiO_2 (black), sensitized electrode before (red) and after (blue) curing, and electrode after leaching (green). The Soret was truncated to highlight the Q-band region.

In a second set of leaching studies, the TiO_2 electrodes were sensitized with the porphyrins using same method as the initial leaching study, and then they were 'cured' by heating for 1 h in an acetonitrile solution containing 0.6% water at 80^{o}C. The results of that study are shown in Figure 44. It was hypothesized that the deprotection reaction of the silatrane dye on the TiO_2 surface only required a single bond to form in order for the dye to stay on the surface. However, the maximum number of bonds was desired. During the curing process, the silatrane porphyrin could further react with the surface in a porphyrin-free solvent and allow the polar triethanolamine byproduct to dissolve away from the electrode. The carboxylate and phosphonate analogues do not have the same issue with deprotection, but could theoretically change their surface bonding system in the different solvent.

The results of the study provide good evidence that the curing process affects the surface linkage. In the case of Zn-TTP-COOH **Zn-23**, the linker stability was so low that the porphyrin mostly desorbed into the curing solution. After leaching, the carboxylate-linked dye was effectively removed from the surface. In the case of the phosphonate- and siloxyl-linked analogues, the linkages were relatively stable during the curing process, showing only minor differences in porphyrin absorbance. Slight shifting in absorbance peaks after curing is likely due to the differences in porphyrin solvent exposure before the spectra were obtained. After leaching, a larger proportion of phosphonate and silatrane porphyrins was still on the electrode compared to the uncured samples, with nearly half of the siloxyl-linked porphyrin still on the surface under the harsh leaching conditions. The results echo the initial leaching study in the surface stability trends, but suggest that curing allows for stronger surface interactions. It is likely that a larger percentage of surface-linked dyes transitioned to a multi-dentate connection type. More experiments and analyses would need to be performed to determine the best experimental conditions for curing the electrodes and the reasoning for their increased stability.

The leaching studies along with the PEC testing show that siloxyl-linkages have increased stability over the phosphonate linkages, and equal PEC performance, making it a better candidate for surface linkages where high stability is necessary.

4. FUSED PORPHYRIN DIMERS

4.1. Introduction

Dramatic alteration of porphyrin properties can be accomplished fairly readily. This is due in part to the extensive set of synthetic schemes made available over the years. Many of these capitalize on the aromatic nature of the macrocycle and also the exchange of metal and non-metal atoms bound to the inner pyrrole nitrogens. Methods to expand the aromatic ring allow for extension of light absorption from the typical UV-Visible region towards the infrared, leading to new properties and applications.[121-124]

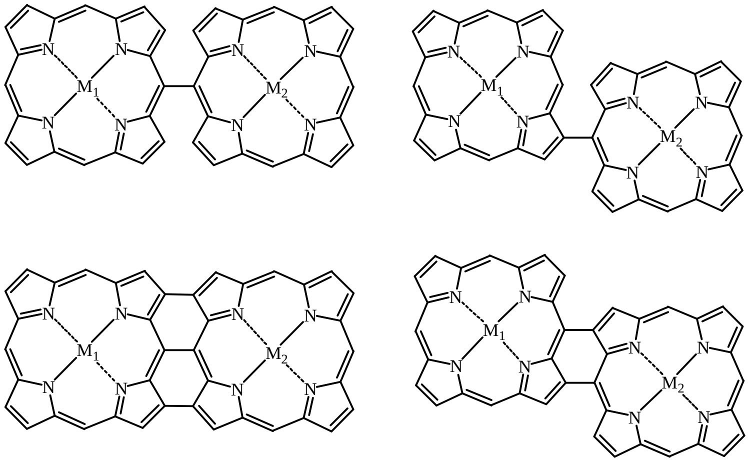

Figure 45. Porphyrin dimer species. Meso-meso connected (top left), meso-β connected (top right), meso-meso β-β triply connected (bottom left), and meso-β doubly connected (bottom right) porphyrin dimers. The identity of M_1 and M_2 can be a range of metal and non-metal atoms.

Porphyrin dimer species with the general structures shown in Figure 45 were only recently brought into the porphyrin mainstream literature by Osuka and co-workers.[53, 125-126] The singly connected porphyrins are orthogonal, retaining the general properties of the monomer porphyrin species. However, meso-β doubly connected and meso-meso β-β triply connected porphyrin dimers have their aromatic rings fused. With the fusion comes a dramatic shift in the optical absorption properties towards the near-infrared (NIR), with the triply connected dimer absorbing further into the NIR region than the doubly connected. The electrochemical properties also change dramatically.[53, 127]

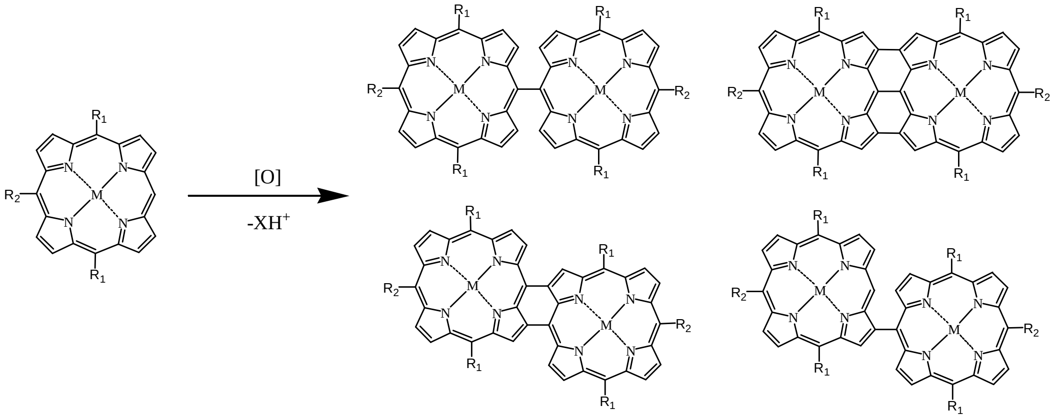

Figure 46. Oxidative synthesis of porphyrin dimers. M can be a range of metal and non-metal atoms. Generally Zn^{2+}, Cu^{2+}, Ni^{2+}, Pd^{2+} are used. X is the number of protons produced, with two for each coupling reaction to form a new porphyrin-porphyrin bond. [O] denotes oxidation, the removal of electrons from the porphyrin.

Via the oxidative synthesis shown in Figure 46, porphyrins with unsubstituted meso and surrounding β positions can dimerize upon formation of the porphyrin radical cation, with the products depending on the porphyrin structure and the equivalents of oxidant used. Porphyrins with two unsubstituted meso positions are able to polymerize, and were the initial focus of research by Osuka. Long chains of meso-meso connected porphyrins were synthesized and tediously purified for analysis.[128] These meso-meso connected porphyrins were later able to be further reacted using similar synthetic techniques to the triply connected fused porphyrin analogues.[129]

Synthetic techniques for the oxidative reaction include the use of electrochemical methods or using one-electron chemical oxidizers. Electrochemical synthesis is an inefficient method to produce a bulk product, but the reaction can be controlled using specific electrochemical potentials. This is an optimal method when a reactant has multiple redox mechanisms or when electrochemical studies are desired. For bulk electrochemical reactions, a solution containing an inert electrolyte and the reactant porphyrin is used in a typical three-electrode electrochemical setup. At potentials where the porphyrin is oxidized, the radical cation porphyrin species react and dimerize. Generally, high surface-area working and counter electrodes are employed to speed the process.

While electrochemical techniques provide a route to relatively controlled reactions, the most efficient way to produce a bulk product is with a chemical oxidative synthesis. These methods have been used for oxidative polymerizations of aniline, pyrrole, thiophene, and many others.[130] However, the reactivity of porphyrins is such that many oxidizers have side-reactions beyond removing electrons.[53, 131] In addition, porphyrins have multiple oxidations, with the first appearing to be the only one required for the oxidative dimerization reaction.

A range of one-electron chemical oxidizers have been tested in the porphyrin fusion reactions. All are capable of oxidizing the porphyrin to promote the reaction, but their cost, stability, and tendency for side-reactions vary considerably. Silver(I) salts such as $AgPF_6$ are strong oxidizers in solvents such as chloroform, and were initially the most commonly used oxidants to form meso-meso connected porphyrins.[125, 132] Tris(4-bromophenyl)aminium hexachloroantimonate (BAHA) was initially used to produce the doubly and triply connected porphyrin dimers, but halogenated side-products occurred to a significant degree.[53, 126] The meso and β positions are reactive to nucleophilic attack when oxidized, and thus inert ions must be used. BAHA contains bromine and chlorine atoms which are the likely sources of contamination during the reaction. When $AgNO_2$ was used, oxidation of the porphyrin followed by meso substitution by NO_2^- yielded a meso-NO_2 porphyrin in high yield.[125] Mixtures of the strongly oxidizing $AuCl_3$ in conjunction with AgOTf also produced fused porphyrin dimer products, but without the silver additive there was significant chlorination of products.[131] Currently, the most commonly used chemical oxidation method to produce doubly and triply connected porphyrins is a mixture of the moderately oxidizing 2,3-dichloro-5,6-dicyano-1,4-benzoquinone (DDQ) with scandium(III) salts.[133] The scandium ion coordinates DDQ, forming a more strongly oxidizing species capable of oxidizing most porphyrins.

Using a singly meso-unsubstituted porphyrin a reactant, porphyrin dimers are the main products of the oxidative reaction. When multiple equivalents of oxidant are used, doubly and triply connected porphyrins prevail. However, the choice of metal or non-metal atom in the porphyrin macrocycle has a major impact on the ratio of doubly and triply connected porphyrin dimers.[53, 133] Irrespective of the above oxidants used, zinc porphyrins tend to produce a majority of triply connected porphyrins when multiple equivalents are used. Copper porphyrins tend to give mixtures of doubly and triply connected porphyrins. Nickel and palladium porphyrins tend to give a majority of doubly connected products.

Porphyrins with inserted metals are always used for the oxidative synthesis for a few reasons beyond those described above. First is that many of the reactions use metal ions with labile ligands as the oxidizer (i.e. Ag^+, Au^{3+}, Sc^{3+}), making these ions capable of insertion into the macrocycle and complicating the reaction. Also, acidic protons capable of fully protonating the inner pyrrole nitrogens are a co-product of the reaction, with protonated porphyrins generally being unreactive. Metalation decreases this chance of protonation. After the reaction, some of the metals are capable of being removed to form the freebase porphyrin products, allowing for different metals to be inserted. Palladium is generally hard to remove, followed by nickel, then copper, with zinc the most readily removed of the metals shown in Figure 46.[31]

An interesting and relatively unexplored detail of the doubly and triply connected fused dimer porphyrins is their ability to have two different metal or non-metal atoms in a single aromatic macrocycle. Fendt and co-workers showed this was possible, providing some electrochemical and optical properties of the mixed-metal species.[127]

Currently, the photophysical properties of doubly and triply connected porphyrins limit applications based on their optical properties. Although they absorb a large amount of visible and NIR light, they undergo non-radiative relaxation in an uncharacteristically fast rate, with excited-state lifetimes of less than 20 picoseconds.[134-136] This suggests an efficient excited-state relaxation mechanism. A few hypotheses were unveiled.[134-135, 137] No conclusive evidence of any mechanism has been established to date, but various results suggest it is a consequence of an accessible pathway from the S_1 excited-state to the S_0 ground-state. If a mechanism is determined and structural changes allow the relaxation rate to decrease, the subsequent increase in excited-state lifetime of these types of molecules would open up new frontiers for their applications.

4.2. Results and Discussion

4.2.1. Synthesis

Many of the commonly used chemical oxidants described earlier require tedious anhydrous reaction conditions, darkness, and/or use expensive metals. However, the relatively inexpensive and stable transition metal ion Cu^{2+} becomes a strong oxidizer in certain environments.[49] For example, the electrochemical potential for the Cu^{2+}/Cu^{+} redox process of $Cu(ClO_4)_2$ in 1-propanol is 0.39 V vs. SCE, making Cu^{2+} a weak oxidant.[49] However, in acetonitrile $Cu(ClO_4)_2$ has a published value of 0.95 V vs. SCE, and in nitromethane it is 1.01 V vs. SCE (converted from ferrocene reference to SCE by adding 0.36 V).[49, 138-140] These values vary with the counterion or electrolyte in the system.[138] Water has an effect on the oxidizing ability of the Cu^{2+} salts, making the oxidation potentials more negative (weaker oxidizer) due to ligation with the naked copper ion. Trace amounts of water (10 mM), common even in some high-purity solvents, affect these potentials. Published values for oxidation potentials will likely include this variable to a degree.[49, 141] Projected values for Cu^{2+}/Cu^{+} electrochemistry in anhydrous nitromethane solvent and with perchlorate counterion are 1.05 V vs. SCE.[141] Even with trace amounts of water, the Cu^{2+} redox potentials in acetonitrile and nitromethane are generally capable of oxidizing a wide variety of porphyrins, and thus capable of promoting the porphyrin-porphyrin coupling reactions. Indeed, $Cu(ClO_4)_2$ in acetonitrile has previously been used to oxidize porphyrins.[50]

A general synthetic scheme was used with partially hydrated $Cu(ClO_4)_2$ or $Cu(BF_4)_2$ as a source of Cu^{2+}, and with acetonitrile or nitromethane solvent to produce the strongly oxidizing conditions. Previous research has shown that it is possible to use amounts of a non-coordinating anhydrous solvent and maintain a strongly oxidizing environment.[50] However, co-solvents were not used due to the acceptable solubility of the porphyrins during the reaction. Doubly and triply connected fused porphyrin dimers were the desired products, so 3-3.6 porphyrin equivalents of Cu^{2+} was used to produce fully-fused porphyrin dimers, minimizing all singly connected porphyrin dimer intermediates. Experimental details for all reactions are contained in Chapter 6.4.

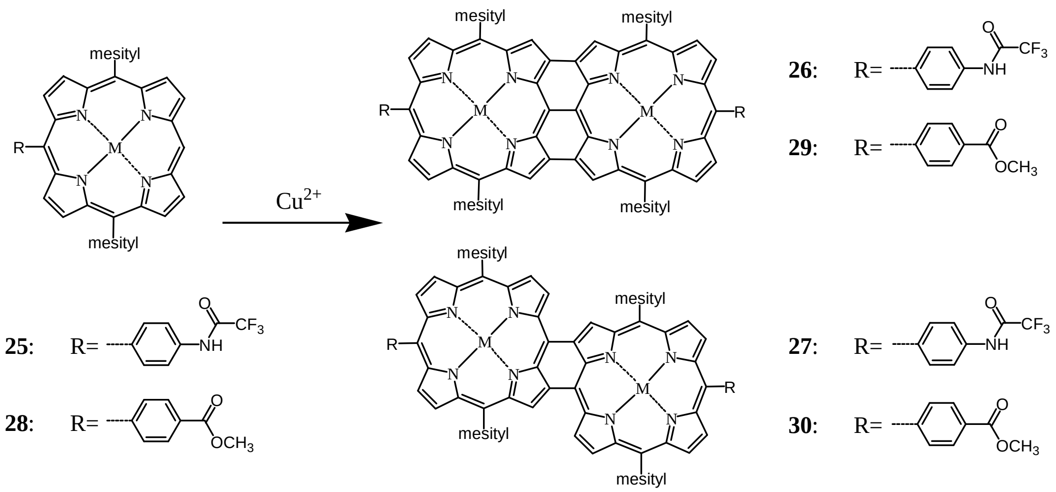

Figure 47. Fused porphyrin dimers. Source of Cu^{2+} was $Cu(ClO_4)_2$ or $Cu(BF_4)_2$. Product mixtures were dependent on reaction conditions and porphyrin metalation (M). Experimental details are contained in Chapter 6.4.

Figure 47 shows the general reaction scheme, with product mixtures containing both doubly and triply connected porphyrin dimers for all experimental conditions with acetonitrile solvent. However, using nitromethane solvent with **Cu-25,** the doubly connected porphyrin **Cu-27** was obtained as the sole product. After completion of the reaction, the porphyrin products were in their oxidized form. The reactions were quenched using aqueous potassium ferrocyanide as a weak one-electron reductant, putting the porphyrin molecule into its stable, neutral form.

Purification of product mixtures containing both doubly and triply connected porphyrins was difficult. Due to solubility issues and similar R_f values, all fused dimers containing the same metal ion (Cu^{2+} or Zn^{2+}) could rarely be purified from the crude reaction products. Exploiting a tendency for the triply connected porphyrins to have increased binding strength to its metal ions compared to the doubly connected porphyrins, it was possible to selectively demetalate the doubly connected porphyrin dimer from a mixture of Cu-triply and Cu-doubly connected products. Using a mixture of chloroform, trifluoroacetic acid, and sulfuric acid, Cu-doubly connected products were demetalated with minimal demetalation of the Cu-triply connected analogue. This provided increased separation of products in column chromatography and ease of purification. Selective demetalation of product mixtures containing zinc porphyrins was not possible using a variety of weak acids.

Cu-25 was prepared from **1** by reacting with trifluoroacetic anhydride and subsequent insertion of Cu^{2+}, with experimental procedures described in Chapter 6.4. The above oxidative reaction procedure with **Cu-25** using $Cu(ClO_4)_2{\bullet}6H_2O$ in acetonitrile yielded **Cu-26** and **H_2-27** at 29% and 34%, respectively. A similar reaction with **Cu-28** yielded **Cu-29** and **H_2-30** at 31% and 47%, respectively. Switching to nitromethane solvent and $Cu(BF_4)_2{\bullet}6H_2O$, **Cu-25** yielded only doubly connected **Cu-27** as the sole product which was easily isolated at 98% yield without need for demetalation and column chromatography.

Zn-28 underwent a reaction with $Cu(ClO_4)_2{\bullet}6H_2O$ in acetonitrile to form a mixture containing mostly triply connected **Zn-29**. However, there were increased difficulties with purification stemming from an inability to selectively demetalate the products as with the previous reactions with the Cu-porphyrins. The Zn-products were fully demetalated for purification, but only the triply connected **H_2-29** was obtained in pure form at a rather low 36% yield.

Metalation of doubly and triply connected fused freebase porphyrin dimers was performed by conversion of **H_2-27** to **Zn-27**, **H_2-27** to **Cu-27**, **H_2-29** to **Zn-29**, and **H_2-30** to **Zn-30** with different reaction procedures. Metalation of doubly connected **H_2-27** and **H_2-30** with either zinc(II) acetate or copper(II) acetate using the method discussed in Chapter 6.1 was facile and much like a standard tetra-aryl type porphyrin, giving a quantitative yield of product from an overnight reaction. Metalation of triply connected **H_2-29** to the di-zinc product was more difficult, requiring long-term heating to promote the reaction past the mono-zinc product. Column chromatography provided a purified product in only 62% yield. It is possible that mixed-metal triply connected porphyrin species could be synthesized from mono-zinc fused dimers as readily-accessible starting materials.

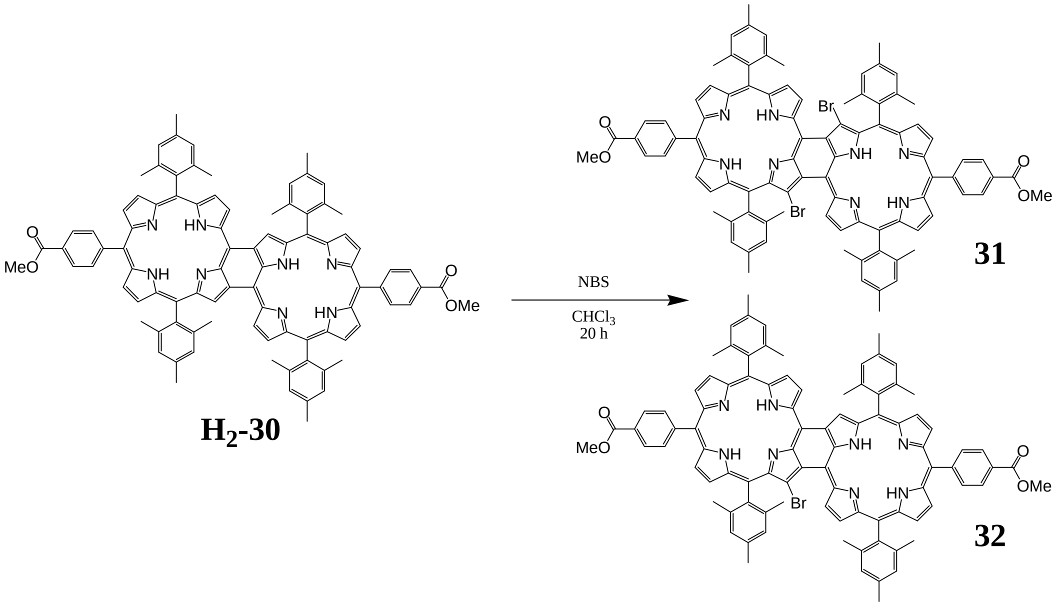

Figure 48. Bromination of **H_2-30**

The reactivity of the obtained doubly connected porphyrin dimers was gauged with a standard bromination reaction shown in Figure 48. Experimental details are contained in Chapter 6.4. Using a single equivalent of N-bromosuccinimide (NBS), bromination of the porphyrin was selective at the porphyrin positions shown. Because the reaction was performed at room temperature and all NBS was consumed, those specific positions appear to be the most reactive to electrophilic substitution, and akin to the more reactive meso positions than the β positions of standard aryl porphyrins.

4.2.2. Absorbance Spectra

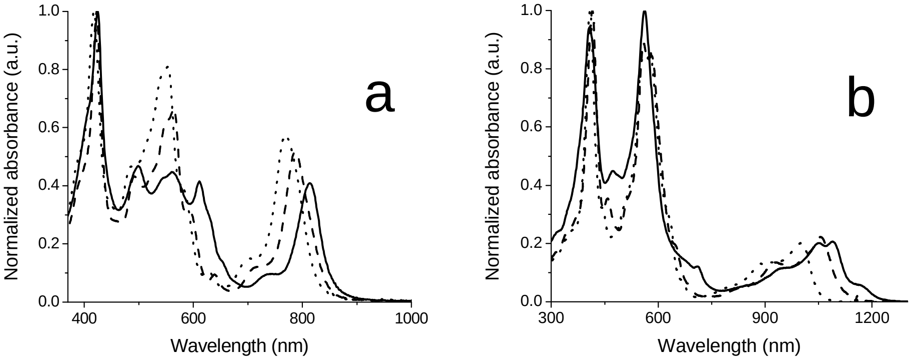

Figure 49. Absorbance spectra of fused porphyrin dimers. (a) doubly connected porphyrins **H_2-27** (solid), **Zn-27** (dashed), and **Cu-27** (dots). (b) triply connected porphyrins **H_2-29** (solid), **Zn-29** (dashed), and **Cu-29** (dots). Spectra normalized at the highest absorbance value.

Doubly and triply connected fused porphyrin dimers have distinctive spectroscopic features as shown in Figure 49. The fused dimers absorb throughout the ultraviolet, visible, and into the NIR with three sets of absorption bands (I,II,III). Unlike simple porphyrins, whose spectra relate to the four orbital model, fused porphyrin spectra can be approximated using an eight orbital model.[142] Band I contains a characteristic peak near 420 nm for doubly connected and 410 nm for triply connected fused porphyrins. Band II is a strongly absorbing set of peaks in the visible region, spanning from near 500 to past 600 nm. Band III consists of the longest wavelength peaks, with doubly connected porphyrins having main peaks around 800 nm and the triply connected between 1000 and 1100 nm with broad shoulder peaks. The metalated analogues are blue-shifted in absorbance from the freebase counterparts, with Cu-porphyrin dimers blue-shifted more than the Zn-porphyrin dimers.

The spectral features were not noticeably affected by the differences in meso-phenyl substitution patterns between triply connected porphyrins **26** and **29**, and between doubly connected porphyrins **27** and **30**. The orthogonal nature of the phenyl ring rotation electronically disconnects the rings, decreasing their interaction with the porphyrin orbitals. However, brominated products **31** and **32** are significantly different from the non-brominated analogue as seen in Figure 50. Band III decreases in relative intensity and shifts with increasing bromination, while there is a slight increase in relative intensity for Band II.

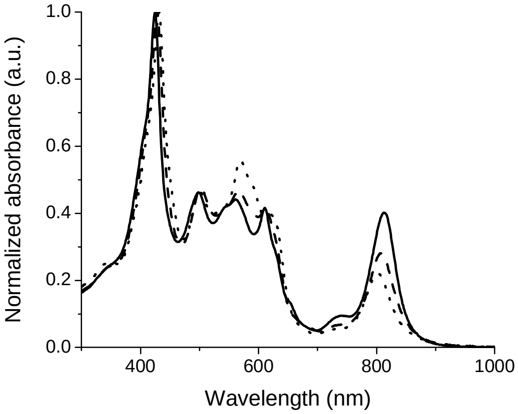

Figure 50. Absorbance spectra of doubly connected porphyrins **H_2-30** (solid), mono-brominated **32** (dashed), and di-brominated **31** (dots).

4.2.3. Macrocycle Distortions

The fused porphyrins have been shown to be relatively planar in conformation;[53] however, some of the synthesized molecules showed signs of distortion as revealed by ^{1}H-NMR data (contained in Chapter 6.4). The ^{1}H-NMR of triply connected **H_2-29** showed an unsymmetrical and broad peak for the four β-type hydrogens near the fused porphyrin connections and also for the four inner pyrrole hydrogens. These peaks are also dramatically shifted from similar freebase triply connected molecules, with the β-type hydrogens at 6.91 ppm compared with a literature value of 7.36 ppm, and the inner pyrrole hydrogens at 4.34 ppm compared to 1.42 ppm.[53] The source of the likely distortion is unknown.

The brominated products **31** and **32** show irregular broadening and shifted peaks to an even greater extent than **H_2-29**. The most obvious of which related to the aryl substituents, where twice as many peaks were observed compared to the non-brominated but similarly symmetrical **H_2-30**. For example, di-brominated **31** had four distinct meso-mesityl ortho-methyl peaks compared to two for the non-brominated analogue. This suggests a change in symmetry for **31** from the expected C_{2h}. The degree of splitting and isolation of the peaks allowed for a more detailed analysis.

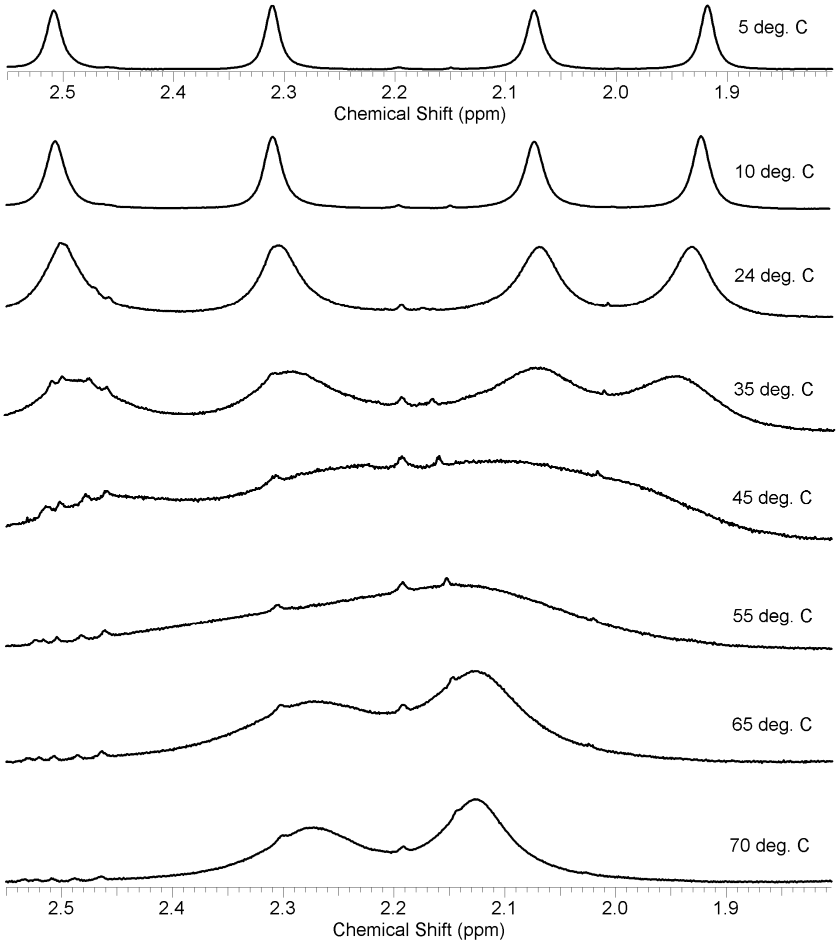

Figure 51. 500 MHz ^{1}H-NMR spectra of **31** in pyridine-d_5 at various temperatures.

Shown in Figure 51 are the ^{1}H-NMR peaks corresponding to the mesityl ortho-methyl groups at various temperatures. As the temperature increases, the four distinct methyl groups coalesce into two. Less dramatic coalescence occurs for the meso-mesityl meta-hydrogens and for the aryl hydrogens on the meso-phenyl substituent with ester moiety. From chemical shifts and coalescence temperatures, the activation barriers were estimated as $\Delta G_{323}^{\ddagger}$ = 15.0 ± 0.5 kcal/mol for the mesityl ring and $\Delta G_{297}^{\ddagger}$ = 15.7 ± 0.5 kcal/mol for the meso aryl ring with ester moiety.[143] Coalescence of the peaks could be due to equilibrium between two macrocycle conformations or rotation of the phenyl rings if they were being hindered. The similar activation barriers suggest that a porphyrin macrocycle conformational change is involved. Indeed the barriers to rotation for mesityl and p-substituted phenyl substitutents on a porphyrin are quite different, >26 kcal/mol and 14-18 kcal/mol, respectively.[143-146]

The origin of the macrocycle conformational change can be surmised from the structural difference between **31** and **H_2-30**, where no peak broadness was observed in the NMR. Substitution of bulky bromines for the original β-hydrogens could be forcing the dimer out of its original planar conformation and symmetry. Steric hindrance between the bromines and the opposing β-hydrogens on the fused porphyrin are the likely cause. Overcoming the barrier equates to the process of the macrocycle twisting while bromine slides past the opposing β-hydrogen. This allows for equilibration between the two conformations.

4.2.4. Electrochemistry

Table 7. Fused porphyrin dimer electrochemistry

Porphyrin	Electrochemistry (V vs. SCE) $E_{ox\ 1}$	$E_{ox\ 2}$	$E_{red\ 1}$	$E_{red\ 2}$
Doubly connected				
H_2-30	0.79	1.09	-0.66	-0.90
Zn-27	0.68	0.85	-0.79	-1.03
Zn-30	0.66	0.82	-0.82	-1.05
Triply connected				
H_2-29	0.68	1.03	-0.47	-0.74
Zn-29	0.56	0.78	-0.65	-0.88
Cu-29	0.67	1.05	-0.61	-0.87

Electrochemistry performed in dichloromethane containing 100mM $TBAPF_6$ electrolyte with ferrocene as internal reference.

Doubly and triply connected fused porphyrin dimers have vastly different electrochemical properties compared to the un-fused porphyrin analogues. The increase in effective conjugation length of the fused macrocycle makes the HOMO-LUMO gap smaller and the porphyrins easier to oxidize.[53] Table 7 shows electrochemical oxidation and reduction values for selected doubly and triply connected fused porphyrin dimers. Each porphyrin is capable of being oxidized or reduced by up to two electrons at moderate potentials. The metals are inert at the applied potentials, so the redox reactions involve forming macrocycle-based cationic or anionic species. Triply connected porphyrins tend to both oxidize and reduce more easily than the doubly connected analogues. The zinc porphyrins oxidize at less positive potentials than the freebase and copper porphyrin analogues, owing to the interactions between the metal ions and the macrocycle.

5. SUMMARY, CONCLUSIONS, AND PERSPECTIVES

Porphyrins are fascinating in their diversity of physical, electrochemical, and photophysical properties. They are synthetically malleable, allowing for structural variations on a nearly limitless scale. A few of these porphyrin varieties were described in the previous chapters, and each is useful for multiple applications. They can be polymerized into a semiconductive material as in Chapter 2, covalently bonded to metal oxide surfaces as in Chapter 3, and the macrocycle can be greatly expanded by ring fusion into porphyrin dimers as in Chapter 4.

The single most useful property of porphyrin compounds is their ability to absorb visible light. This region of the solar spectrum contains the peak photon flux of our sun, and thus porphyrins are excellent solar energy collectors. Efficiently using this absorbed energy was a goal in Chapters 2 and 3. Liquid-junction photoelectrochemical cells (PEC), with electricity as an output, were experimentally used as a proxy for the varied types of organic photovoltaics and for photoelectrochemical cells capable of forming fuels such as hydrogen gas from water.

Initial experiments using porphyrin polymer thin films in PEC showed a variety of system inefficiencies. It is likely that **Poly-1** absorbed light but the energy could not reach a location where electron transfer could occur. Dyad polymer **Poly-2** could perform internal charge separation with the porphyrin and fullerene, but those charges could not efficiently migrate to opposing electrodes in the PEC design. **Poly-2** functioned nearly five times more efficiently than **Poly-1**, however.

The hole migration properties of the porphyrin polymers were studied, with results suggesting rate limitations of ion penetration into the oxidized polymer films. Minimum D_{CT} values of 1.7 x 10^{-9} cm^2 sec^{-1} for **Poly-1**, 1.7 x 10^{-8} cm^2 sec^{-1} for **Poly-2**, 1.0 x 10^{-8} cm^2 sec^{-1} for **Zn-Poly-1**, and 2.3 x 10^{-8} cm^2 sec^{-1} for **Poly-3** were determined using a chronocoulometric method. It is possible that solid-state conductivity studies of porphyrin polymer films might be more practical. Additional experimentation comparing porphyrin polymer derivatives could lead to new insights and applications.

Studies of electron conductivity via the fullerene substituent in films of dyad polymer **Poly-2** have not yet been performed, and could shed additional light on the performance of dyad polymer films. Varying the PEC design could also provide information on the system. Utilizing electron- and hole-blocking layers on each electrode would direct the flow of photocurrent, possibly decreasing unwanted recombination processes. High surface area electrodes such a p-type metal oxides or using a bulk heterojunction PEC architecture could decrease the distance from porphyrin polymer to a boundary where electron transfers occur. This could decrease the amount of energy lost due to relaxation from the excited-state in **Poly-1** and charge recombination in **Poly-2**, increasing efficiency.

While thin film porphyrin polymers were relatively inefficient solar energy converters in PEC, porphyrins in general are commonly used in DSSC-type photovoltaic PEC. DSSC uses dyes attached to high surface area semiconductive metal oxides as discussed in Chapter 1.1. In Chapter 3 the silatrane functional group was introduced with a new method for forming monolayers covalently attached to metal oxides with siloxyl bonds. Ruthenium complexes and porphyrins were prepared with silatrane functionality, and reacted with TiO_2 and SnO_2 n-type semiconductors to form dye-sensitized electrodes. Their performance and stability were examined and compared with similarly-structured carboxylic acid and phosphonic acid surface linkers. It was determined that the surface linker moiety had less to do with the subsequent PEC performance of the dye on the electrode than the monolayer surface coverage concentration. For the dyes tested, the carboxylate-linked analogue **Zn-23** was hypothesized to have bonded normal to the semiconductor surface in a bidentate coordination, forming an efficiently packed monolayer. The silatrane **Zn-19** and phosphonic acid porphyrins **Zn-22** had significantly lower surface coverage than **Zn-23** and possibly were angled to the surface due to the tetrahedral nature of their surmised bidentate surface bonding. This would yield steric constraints and an inefficiently packed monolayer. Effects of the higher surface coverage for **Zn-23** included a decrease in solvent-exposed metal oxide surface and an increased light harvesting capability over the phosphonate- and siloxyl-linked dyes with similar electrode surface areas.

The stability studies of the carboxylate-, phosphonate-, and siloxyl-linked porphyrins on the TiO_2 surface showed significant differences. Leaching of the dyes from the metal oxide surface under strongly hydrolyzing alkaline conditions revealed the stabilities to be siloxyl > phosphonate > carboxylate. Therefore, the strength of the surface bond has little bearing on the processes involved at the interface of the dyes with the metal oxide. The bond strength would only play a role when conditions are favorable for dye leaching, a circumstance generally found in aqueous solutions. Under neutral to basic pH conditions, the siloxyl surface connections would be more ideal than phosphonate and carboxylate linkers. Since many biological materials function in this pH range, and most bodies of water are also generally neutral to basic in pH, the use of silatranes could open up a range of new applications for materials stabilized on metal oxides.

For future synthetic possibilities, the synthesized silatrane species shown in Figure 29 allow for silatrane derivatization of molecules using various coupling reactions. Use of silatranes for metal oxide surface functionalization will likely become more widespread as the applications of metal oxide nanoparticles and high surface area electrodes continue to expand.

The use of silatranes is just beginning to blossom, and future applications abound. A similarly bright future might be in store for the fused porphyrin dimers discussed in Chapter 4. These doubly and triply connected fused porphyrin dimers were synthesized using a new chemical oxidative reaction utilizing copper(II) salts. In various nitrile solvents and nitromethane, Cu^{2+} becomes a strong oxidizer capable of removing a single electron from a porphyrin. The subsequent radical coupling reactions between two oxidized porphyrins containing unsubstituted meso and β positions produces fused dimers. The generalized reaction can be also be tuned towards doubly or triply connected fused porphyrins as the major products by varying the reaction conditions and starting materials.

The properties of fused porphyrin dimers differ significantly from the porphyrin starting materials. First is the ability of the dimer to contain two distinct metal or non-metal atoms in a macrocycle structure. Secondly is the relative ease for oxidizing or reducing the dimers compared to the starting porphyrin. Multiple oxidations or reductions of the macrocycle, along with two redox-active metals, make the electrochemical properties of the porphyrin dimers complex and tunable. With the possibility of two different metals in the fused dimers, and the ability to alter the porphyrin electrochemistry by varying the macrocycle substituents, the fused dimers have great potential as redox catalysts. For example, the electrochemistry and specific substrate binding affinities could be tuned via structural modifications and metalation. The dimers could weakly bind the substrate as a ligand to one metal with the other metal being active for a specific redox reaction. Regio or enantio-selective reactions would be possible due to specific binding of the substrate to the fused porphyrin dimer catalyst and with the possibility of synthesizing a chiral fused porphyrin dimer. The ability of the fused porphyrins to become doubly reduced or oxidized at moderate potentials and in a narrow potential window (~200 mV) might allow for multi-electron redox reactions to occur when coupled to a redox-active metal, much like the active site of photosystem II.[147] In addition, supramolecular organization of the fused porphyrin dimers could give interesting properties for various applications.

The fused dimers also broadly absorb in the UV-Visible-NIR region with relatively high extinction coefficients. However, the excited-state lifetimes of the fused molecules have been previously determined to be relatively short compared to the starting porphyrins, limiting their use as light energy harvesters.[134-136] Because there is only speculation as to the reason for the picosecond lifetimes, it is possible the issue will be overcome in the future. If so, the fused dimers would be ideal for capturing solar energy for use in energy related applications.

Much effort has been made to gain basic scientific knowledge from the projects in this dissertation. The research presented here expanded on previous ideas and results of the worldwide scientific collective, and there is no doubt it will continue to expand through others' hard work. Humankind's technological stature relies on such innovation to solve our problems and sustain our existence. Hopefully the work herein can be applied to such.

6. EXPERIMENTAL PROCEDURES

6.1. General Experimental Methods

Materials. All reagents and chemicals were obtained from commercial sources unless noted. Specific reagent sources and purities are referenced where applicable. Dichloromethane, hexanes, tetrahydrofuran (THF), 2-methyl-tetrahydrofuran (MTHF), toluene, and triethylamine were distilled prior to use. Acetonitrile (Omnisolv grade) was stored on 4Å molecular sieves. Silica gel chromatography was performed using 230-400 mesh silica gel (Silicycle, Siliflash F60). Indium doped tin oxide (ITO, 8-12 Ω/sq) and fluorinated tin oxide (FTO, TEC 15, 12-14 Ω/sq) on silica glass was obtained from Delta Technologies and Hartford Glass, respectively.

General procedure for porphyrin metalations. Unless otherwise stated, metalation of porphyrins was performed by adding porphyrin and 5-10 equivalents of zinc(II) acetate dihydrate or copper(II) acetate hydrate to a 5:1 solution of dichloromethane / methanol. The solution was heated for 30 min and then allowed to stir overnight under a nitrogen atmosphere. The organic layer was washed with distilled water, saturated aqueous sodium bicarbonate, and again with distilled water, and the solvent removed under reduced pressure. All reactions went to completion.

General analytical methods. UV–Visible-NIR spectroscopy was performed using a Shimadzu UV-3101PC UV–Visible–NIR spectrophotometer or Shimadzu UV-2550 UV–Visible spectrophotometer.

Steady-state fluorescence spectra were measured using a Photon Technology International MP-1 spectrometer and corrected for detection system response. Excitation was provided by a 75 W xenon-arc lamp and single grating monochromator. Fluorescence was detected 90° to the excitation beam via a single grating monochromator and an R928 photomultiplier tube having S-20 spectral response and operating in the single photon counting mode.

Mass spectrometry was performed by the MALDI-TOF method using a Voyager DE STR from Applied Biosystems in reflector mode for all molecules, and linear mode for polymers. Commonly used matrices were terthiophene, diphenylbutadiene, and sinapinic acid.

^{1}H NMR spectra were obtained in deuterated solvents using a Varian 300 MHz, 400 MHz, or 500 MHz instrument with tetramethylsilane as internal reference. Proton assignments were aided by the use of COSY experiments.

Profilometry was used to determine sample thicknesses using a calibrated Sloan Dektak II Profilometer.

Electrochemistry was performed using a CH Instruments 650C or 760D electrochemical workstation using a standard 3-electrode cell setup. Counter and reference electrodes were platinum gauze and pseudo Ag/AgCl, respectively. Working electrodes and electrolytes were specific for each experiment. Potentials referenced to SCE using the ferrocene / ferrocenium redox couple as an internal standard, with values varying by solvent.[140]

PEC testing. The electrodes were connected to a programmable Keithley 2400 Sourcemeter linked to a computer via a National Instruments USB-6009 communication board, and all data were acquired by programs written using LabView 7.1 software. A 450 W Osram® xenon arc lamp with a Jobin Yvon single-grating monochromator was used for illumination at specific wavelengths. Light intensity was measured at each tested wavelength using a calibrated silicon diode detector (Newport Corp. model 818-UV) to obtain the power density spectrum. Current vs. wavelength measurements were obtained in 4 nm increments. Photocurrent was determined by subtracting the average dark current from the average light current. AM1.5G illumination was obtained using the xenon arc lamp with added filter (Newport Oriel model 81094) to simulate the AM1.5G solar spectrum. The lamp output was calibrated to 1000 W/m^2 using a Daystar Solar Meter. Current-Voltage measurements were obtained scanning an applied potential using a Keithley 2400 Sourcemeter.

6.2. Experimental Procedures for Chapter 2

Materials. Lithium perchlorate ($LiClO_4$) and sodium tetrakis-(3,5-bis-trifluoromethylphenyl)borate ($NaBPh_4$) were obtained from Alfa Aesar. Lithium bis(trifluoromethane)sulfonamide ($LiNTf_2$), tetrabutylammonium p-toluene sulfonate (TBAPTS), and 2,6-di-tert-butylpyridine were obtained from Sigma-Aldrich.

Synthesis. Porphyrin monomers **1** and **2** were synthesized by Dr. Paul Liddell according to previously-established methods.[46-47] Tetrakis-p-hydroxyphenyl porphyrin was obtained from Sigma-Aldrich and zinc was inserted according to Smeets et al. to produce monomer **3**.[148]

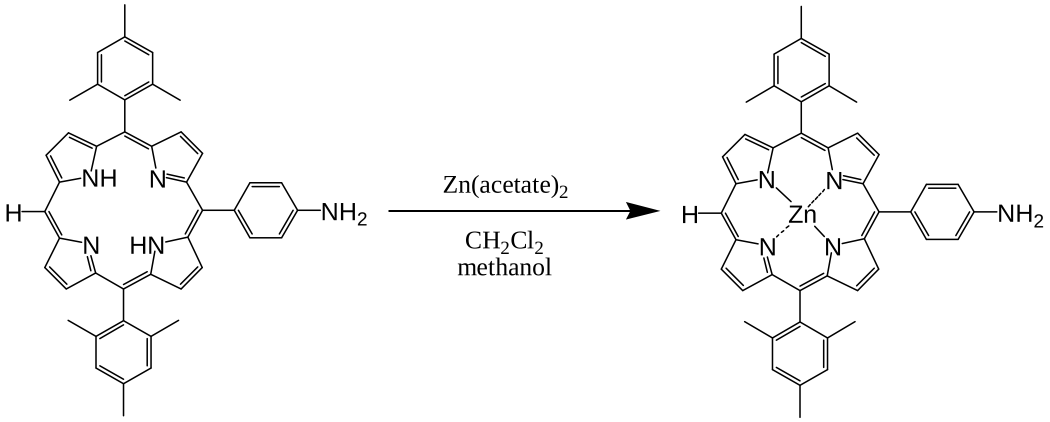

1 **Zn-1**

Zn(II)-5-(4-aminophenyl)-10,20-bis(2,4,6-trimethylphenyl)porphyrin (Zn-1). Porphyrin **1** was metalated to **Zn-1** using general procedure for porphyrin metalation given above. ^{1}H NMR (400 MHz, CDCl$_3$) δ 10.14 (1H, s, meso-H), 9.33 (2H, d, *J*=4 Hz, β-H), 8.96 (2H, d, *J*=4 Hz, β-H), 8.90 (2H, d, *J*=4 Hz, β-H), 8.80 (2H, d, *J*=4 Hz, β-H), 7.92 (2H, d, *J*=8 Hz, Ar-H), 7.29 (1H, s, Ar-H), 6.75 (2H, d, *J*=8 Hz, Ar-H), 3.50 (2H, s, NH$_2$), 2.65 (6H, s, Ar-CH$_3$), 1.83 (12H, s, Ar-CH$_3$); MALDI-TOF-MS m/z calcd for $C_{44}H_{37}N_5Zn$ 699.2, obsd 699.0; UV-visible ($\lambda_{max,}$ CH$_2$Cl$_2$) 416, 544, 580 nm.

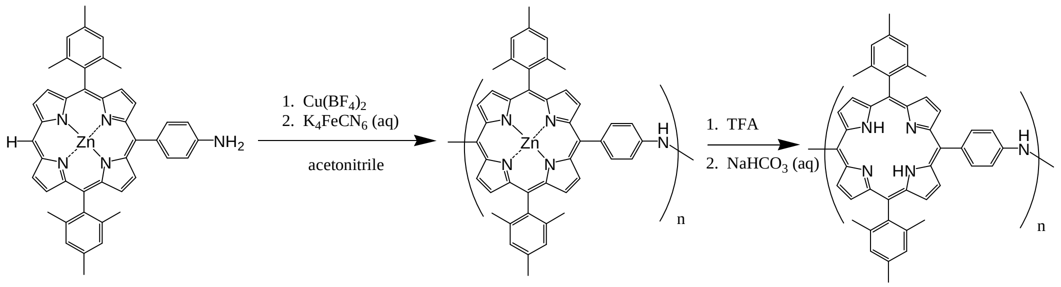

Zn-1

Poly-1

Chemical oxidative polymerization of Zn-1. A mixture of 300 mg porphyrin monomer **Zn-1** (4.28×10^{-4} mol) in 70 mL of acetonitrile was placed under nitrogen and cooled in an ice bath. A solution of 517 mg ($1.5 \text{x} 10^{-3}$ mol, 3.5 equivalents) $Cu(BF_4)_2$•6 water in 10 mL of acetonitrile was added. All porphyrin immediately dissolved and the solution turned green. The ice bath was removed and the reaction was stirred at room temperature for 5 h. An aqueous solution of 1.5 g potassium ferrocyanide in 25 mL distilled water was then added to quench the reaction and precipitate the porphyrin. The mixture was filtered and the residue washed with aqueous basic EDTA, then aqueous sodium bicarbonate, and finally distilled water. The solid remaining was dissolved in 50 mL of trifluoroacetic acid and stirred under a nitrogen atmosphere for 3 h. The solution was transferred to a separatory funnel and 120 mL chloroform and 150 mL of water were added. The organic layer was washed with 300 mL of saturated aqueous sodium bicarbonate and then 200 mL of distilled water, and the solvent was removed under reduced pressure. The solid obtained was dissolved in 35 mL of dichloromethane, and the porphyrin was precipitated by adding 190 mL of hexanes. The mixture was filtered to yield 196 mg of precipitated porphyrin (72%). ^1H NMR (500 MHz, $CDCl_3$) δ 9.6-8.6 (β-H), 8.0-6.8 (Ar-H, β-H from fused porphyrin impurity, Ar-N-H), 4.2-3.7

($Ar-NH_2$), 2.65-2.60 ($Ar-CH_3$), 2.50 ($Ar-CH_3$ from fused porphyrin impurity), 1.99 ($Ar-CH_3$ from fused porphyrin impurity), 1.90-1.80 ($Ar-CH_3$), -2.25 to -2.45 (N-H); UV-visible ($\lambda_{max,}$ THF) 418, 523, 581, 667, 818, 1062, 1105 nm. Analysis by MALDI-TOF-MS showed a series of peaks corresponding to oligomers of the polymer of different lengths.

Electrochemical polymerization. See Chapter 6.1 for general electrochemical instrumentation and procedures. Monomers were electropolymerized on a 25 μm diameter platinum electrode (CH Instruments), 1.6 mm diameter platinum electrode (Bio Analytical Systems), ITO, or FTO by cyclic voltammetry using CH Instruments 650C or 760D electrochemical workstations. Unless otherwise stated, solutions for electropolymerization consisted of the following: Monomer **1** – 0.60 mM in acetonitrile with 100 mM $LiClO_4$; Monomer **Zn-1 -** 0.53 mM in a 14:1 mixture of acetonitrile:dimethylformamide with 100 mM $LiClO_4$; Monomer **2** - 0.22 mM in dichloromethane with 100 mM tetra-*n*-butylammonium hexafluorophosphate; Monomer **3** – 1.1 mM in acetonitrile with 100 mM $LiClO_4$ and 50 mM 2,6-di-tert-butylpyridine.[42] Various thicknesses of polymer films were obtained by repeated CV cycles at 200 mV/sec, scanning anodic to ~1.3 V vs. SCE for Monomers **1** and **2** and to ~1.1 V vs. SCE for Monomers **Zn-1** and **3**.

Analytical methods. HPLC-gel permeation chromatography was performed on an Agilent 1200 series HPLC with a UV-Visible diode-array detector using a 79911-GP-MXC 5 μm mixed-C column. A calibration curve using polystyrene standards in THF (unstabilized, HPLC grade) with 1 mL/min elution was used for analysis. Dilute 30 μL samples of porphyrin polymer in THF were used for characterization. GPC analysis performed using Agilent ChemStation Rev.B.03.01 with GPC software add-on Rev.B.01.01.

Chemically polymerized porphyrin was analyzed electrochemically using a platinum 1.6 mm diameter electrode. Chronocoulometry of electropolymerized polymer was performed in acetonitrile with 100 mM $LiClO_4$, $LiNTf_2$, TBAPTS, or $NaBPh_4$. Chronocoulometric experiments were performed with increasing step potentials using a 100 ms pulse applied from ~0.2 V vs. SCE for **Poly-1**, **Poly-2**, and **Poly-3**, and ~ -0.1 V vs. SCE for **Poly-Zn-1.**

Counter electrodes for PEC. Platinized FTO (Pt/FTO) glass for use as electrodes in regenerative-type PEC were prepared using conductive FTO glass (Hartford Glass, TEC 15). Holes were drilled in the glass for future electrolyte introduction. A diamond burr and high speed rotary tool were used to place two holes on opposite corners of the glass. FTO was cleaned with distilled water, acetone, and ethanol, and then dried in air. A drop of 10 mM hexachloroplatinic acid (H_2PtCl_6) in anhydrous ethanol was placed on the conductive side of the FTO glass, which was then dried in air. The FTO was heated in air at 450^oC for 1 h, during which time a nearly transparent Pt/PtO film formed.

Regenerative PEC fabrication. Fabrication involved sealing the ITO or FTO with electrodeposited polymer to a platinized counter electrode (Pt/FTO) in a face-to-face design using a heat-sealable polymer (Solaronix, Surlyn®, 25 μm). The Pt/FTO holes were used as the corners of the heat-seal polymer frame. The sensitized electrode was placed on top, and the polymer melted on a hotplate. The electrolyte solution, the specifics of which are contained below, could be introduced via the holes, with a thin microscope slide glass cover used to cover the holes and limit solvent evaporation.

Regenerative PEC testing. See Chapter 6.1 for testing procedures. Unless noted, all photocurrent experiments used an electrolyte consisting of 750 mM 1,4-benzoquinone (BQ) with 25 mM hydroquinone (QH_2) and 150 mM tetra-*n*-butylammonium hexafluorophosphate ($TBAPF_6$) in acetonitrile. No efforts were made to have anhydrous solutions. PEC illuminated area ranged from 1-2 cm^2. For analysis, the FTO and ITO glass reflectance was taken into account to allow for differences in light transmission when illuminating through either electrode as discussed in the text.

6.3. Experimental Procedures for Chapter 3

Materials. The porphyrins TTP–COOH **11**, TMP–COOH **13**, TTP-β-vinyl COOH **23**, TTP-β-vinyl COOMe **24**, and 5,10,15,20-tetrakis-(4'-methylphenyl) porphyrin (TTP) were synthesized by Dr. Paul Liddell, and aminopropylsilatrane (**10**) was synthesized by Dr. Sean Vail.

Synthesis. The compounds cis-$(bpy)_2RuCl_2 \cdot 2H_2O$ and 2-formyl-5,10,15,20-tetra(4'-methylphenyl)porphyrin (β-formyl-TTP **20**) were synthesized according to literature methods.[102, 149]

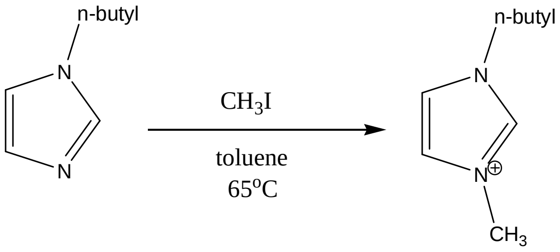

1-Butyl-3-methylimidazolium iodide. A procedure from Bonhote et al. was followed with modification.[22] To a 100 mL round-bottomed flask were added 10 mL (0.076 mmol) of *N*-(n-butyl)-imidazole (VWR) and 20 mL of toluene. The solution was stirred in the dark under a nitrogen atmosphere and 8 mL (0.129 mmol) of iodomethane (Fluka, puriss) was added in 1 mL increments over the course of an hour. The solution was heated to 65°C for 23 h, over which time the product phase-separated. The viscous orange oil was washed twice with 10 mL of hot toluene and volatile liquids were removed under reduced pressure to yield 17.63 g (87%) of the imidazolium salt. ^{1}H NMR(400 MHz, $CDCl_3$) δ 10.02 (1H, s, N–CH–N), 7.55 (1H, t, *J*=2 Hz, N–CH), 7.47 (1H, t, *J*=2 Hz, N–CH–), 4.35 (2H, t, *J*=7 Hz, N–CH_2), 4.13 (3H, s, N–CH_3), 1.93 (2H, m, CH_2), 1.41 (2H, m, CH_2), 0.98 (3H, t, *J*=7 Hz, CH_3). MALDI-TOF-MS m/z calcd for $C_8H_{15}N_2$ 139.1, obsd 139.1.

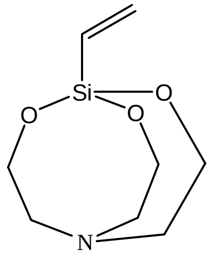

4

Vinylsilatrane (4). Vinylsilatrane was commercially obtained and purified prior to use. The wet yellow solid was first dissolved in dichloromethane and washed with water. A volume of hexanes double the amount of dichloromethane was then added, and a yellow precipitate removed by filtration. Solvent was removed from the filtrate under reduced pressure to yield a white solid that was then washed with hexanes. ^{1}H NMR (400 MHz, $CDCl_3$) δ 6.05-5.96 (1H, m, CH), 5.86-5.77 (2H, m, CH_2), 3.83 (6H, t, *J*=6 Hz, O-CH_2), 2.86 (6H, t, *J*=6 Hz, N-CH_2).

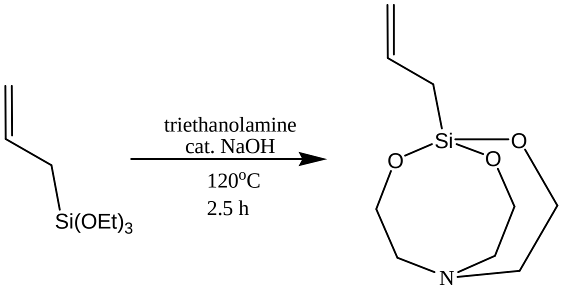

5

Allylsilatrane (5). In a dry round bottom flask was stirred 1.52 g of triethanolamine (1.0 x 10^{-2} mol) with ~5 mg of NaOH. After 10 min 2.28 mL allyltriethoxysilane (1.0 x 10^{-2} mol) was added. The reaction was stirred and slowly heated under a nitrogen atmosphere to 120°C. After 2.5 h, the reflux condenser was removed and the ethanol was distilled under a nitrogen atmosphere. After 1 h the reaction was cooled and yielded a white precipitate. The solid was dissolved in 30 mL of dichloromethane and washed twice with 30 mL water. Hexanes (30 mL) were added to the dichloromethane solution, and the dichloromethane was removed under reduced pressure. The organic solution was then cooled to 0°C, and the precipitate was filtered and washed with hexanes to yield 1.0 g of a fluffy white solid (44%). ^{1}H NMR (400 MHz, $CDCl_3$) δ 6.06-5.95 (1H, m, CH), 4.93-4.78 (2H, m, CH=C*H₂*), 3.79 (6H, t, *J*=6 Hz, O-CH_2), 2.82 (6H, t, *J*=6 Hz, N-CH_2).

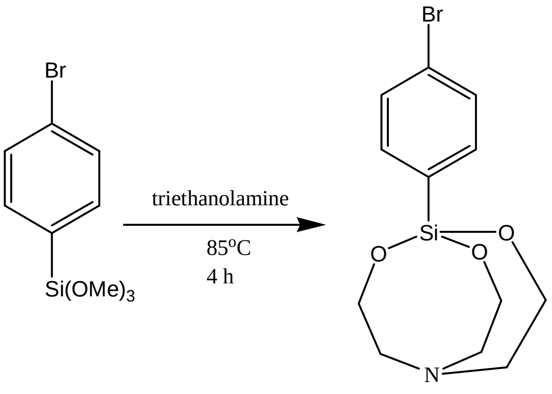

6

p-Bromophenyl-silatrane (6). To a dry round bottom flask was added 15 mL of toluene, 4.62 g of triethanolamine (3.1 x 10^{-2} mol), and 7.00 g of p-bromophenyl-trimethoxysilane (2.5 x 10^{-2} mol). A reflux condenser was attached and the mixture was stirred under a nitrogen atmosphere and heated to 85°C. After 4 h the reaction was cooled and the precipitate was filtered and washed with toluene and methanol to yield a white powder (7.0 g, 85%). ^{1}H NMR (400 MHz, $CDCl_3$) δ 7.59 (2H, d, *J*=8 Hz, Ar-H), 7.38 (2H, d, *J*=8 Hz, Ar-H), 3.89 (6H, t, *J*=6 Hz, O-CH_2), 2.92 (6H, t, *J*=6 Hz, N-CH_2).

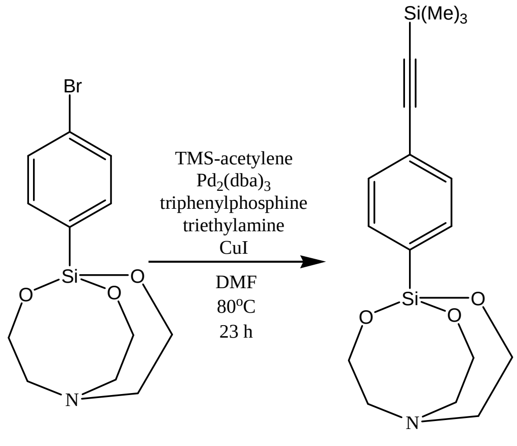

6 **7**

Trimethylsilyl-(4-ethynylphenyl)-silatrane (7). To a dry round bottom flask was added 23 mg (1.2 x 10^{-4} mol) CuI, 72 mg triphenylphosphine (2.7 x 10^{-4} mol), 1.00 g p-bromophenylsilatrane (3.0 x 10^{-3} mol), 5 mL triethylamine, and 15 mL DMF. The solution was purged with nitrogen, and 55 mg (6.0 x 10^{-5} mol) of tris(dibenzylideneacetone) dipalladium ($Pd_2(dba)_3$, Aldrich) was added along with 1.0 mL (7.1 x 10^{-3} mol) trimethylsilylacetylene. A reflux condenser was attached, and the system was purged with nitrogen and heated at 80°C for 23 h. The reaction was cooled and transferred to a separatory funnel with 60 mL of dichloromethane. The solution was washed with water, and the solvent was removed under reduced pressure to yield a brown solid. The solid was redissolved in dichloromethane, and filtered through Celite®, and the solvent was removed under reduced pressure. The crude material was flushed down a silica gel column using dichloromethane eluent to yield 463 mg of a white solid in ~95% purity (44%). ^{1}H NMR (400 MHz, $CDCl_3$) δ 7.66 (2H, d, *J*=8 Hz, Ar-H), 7.36 (2H, d, *J*=8 Hz, Ar-H), 3.90 (6H, t, *J*=6 Hz, O-CH_2, 2.92 (6H, t, *J*=6 Hz, N-CH_2), 0.23 (9H, s, Si-CH_3). MALDI-TOF-MS (sinapinic acid matrix) m/z calcd for $C_{17}H_{25}NO_3Si_2$ + 1(H) (m + H) 348.1, obsd 348.1.

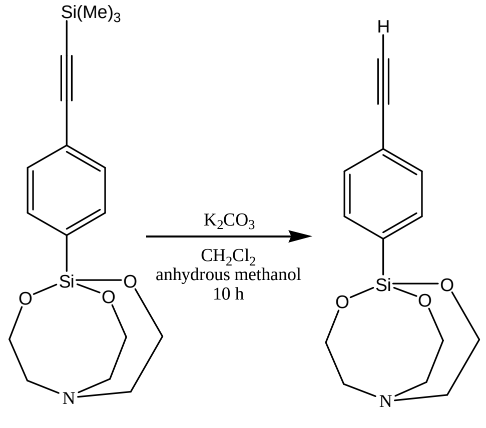

7 **8**

p-Ethynylphenyl-silatrane (8). ~5 mg Trimethylsilyl-(4-ethynylphenyl)-silatrane **7** was dissolved in 200 μL of dichloromethane. The solution was added to a mixture of 2 mg powdered anhydrous K_2CO_3 in 100 μL anhydrous methanol. The mixture was sonicated briefly, purged with nitrogen, and sealed with a stopper for 10 h. The solvent was removed by distillation, and the product residue was dissolved in dichloromethane and decanted from the K_2CO_3. The solution was washed with water and solvent removed under reduced pressure to yield a white solid (~5 mg, 100%). ^{1}H NMR (400 MHz, $CDCl_3$) δ 7.69 (2H, d, *J*=8 Hz, Ar-H), 7.40 (2H, d, *J*=8 Hz, Ar-H), 3.90 (6H, t, *J*=6 Hz, O-CH_2), 3.01 (1H, s, CH), 2.93 (6H, t, *J*=6 Hz, N-CH_2).

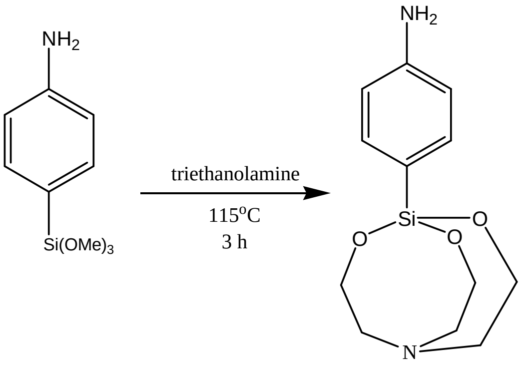

9

p-Aminophenyl-silatrane (9). In a dry round bottom flask was added 2.15 g p-aminophenyltrimethoxysilane (1.0×10^{-2} mol) and 1.52 g triethanolamine (1.0×10^{-2} mol). A reflux condenser was attached and the mixture was heated to 115°C while stirring under a nitrogen atmosphere. After 3 h the reaction was cooled and the solvent was removed under reduced pressure to yield a crude solid. This was recrystallized twice from chloroform and filtered to yield a white solid (1.68 g, 62%). ^{1}H NMR (400 MHz, $CDCl_3$) δ 7.53 (2H, d, *J*=8 Hz, Ar-H), 6.63 (2H, d, *J*=8 Hz, Ar-H), 3.88 (6H, t, *J*=6 Hz, O-CH_2), 3.55 (2H, br s, NH_2), 2.89 (6H, t, *J*=6 Hz, N-CH_2).

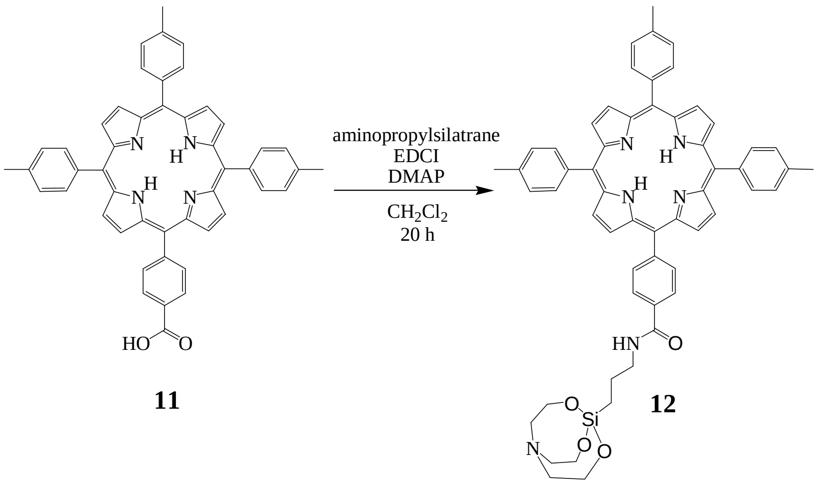

General procedure for porphyrin amide couplings. TTP-sil (12). To a round bottom flask was added 9.7 mg (1.38 x 10^{-5} mol) TTP–COOH **11** and 14.4 mg of EDCI (7.51 x 10^{-5} mol) dissolved in 35 mL of dichloromethane. The solution was stirred for 10 min in an ice bath under a nitrogen atmosphere, and then 12.9 mg of 1-(3-amino)-propylsilatrane (5.6 x 10^{-5} mol) and 6.4 mg of DMAP (5.2 x 10^{-5}) were added. The solution was stirred at room temperature for 20 h under a nitrogen atmosphere, and then washed twice with 15 mL of saturated sodium bicarbonate solution and once with 15 mL of water. The organic layer was concentrated under reduced pressure, and then the product isolated by chromatography on silica gel using chloroform containing 5% methanol as eluent (9 mg, 70%) ^{1}H NMR (300 MHz, $CDCl_3$) δ 8.88–8.77(m, 8H, β-H), 8.25 (2H, d, *J*=8 Hz, Ar–H), 8.15 (2H, d, *J*=8 Hz, Ar–H), 8.09 (6H, d, *J*=8 Hz, Ar–H), 7.55 (6H, d, *J*=8 Hz, Ar–H), 3.82 (6H, t, *J* = 6 Hz, O–CH_2), 3.63 (2H, q, *J*=6 Hz, CH_2), 2.83 (6H, t, *J*=6 Hz, N-CH_2), 2.71 (9H, s, Ar–CH_3), 1.89 (2H, m, CH_2), 0.67 (2H, t, *J* = 7 Hz, CH_2–Si), −2.76 (2H, s, NH). MALDI-TOF-MS m/z calcd for $C_{57}H_{54}N_6O_4Si$ 914.4, obsd 914.4.

The preparation of other silatrane derivatized porphyrins using aminopropylsilatrane followed a similar procedure and isolated yields of these products were >50% in each case.

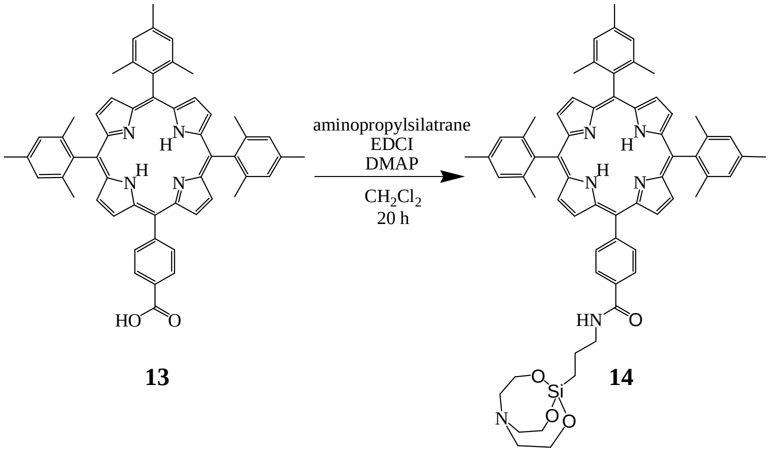

13 **14**

TMP-sil (14). Porphyrin **14** was prepared from TMP-COOH **13**. ^{1}H NMR (300 MHz, $CDCl_3$) δ 8.72 (2H, t, J=5 Hz, β-H), 8.68 (2H, t, J=5 Hz, β-H), 8.63 (4H, s, β-H), 8.24 (2H, d, J=8 Hz, Ar–H), 8.14 (2H, d, J=8 Hz, Ar–H), 7.27 (6H, s, Ar–H), 3.83 (6H, t, J=6 Hz, O–CH_2), 3.63 (2H, q, J=6 Hz, CH_2), 2.85 (6H, t, J=6 Hz, N-CH_2), 2.63 (9H, s, Ar–CH_3), 1.91-1.85 (20H, m, CH_2 and Ar-CH_3), 0.67 (2H, t, J = 7 Hz, CH_2–Si), −2.57 (2H, s, NH).

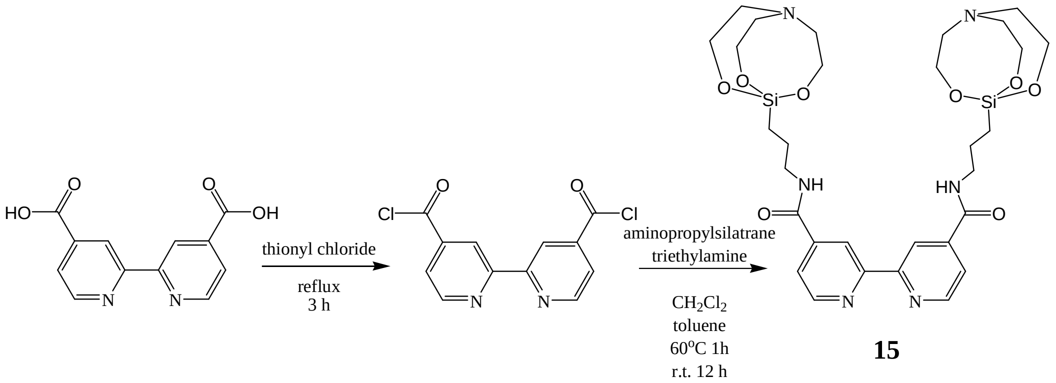

15

Bpy-sil (15). A mixture of 371 mg (1.52×10^{-3} mol) of 2,2$'$-bipyridyl-4,4$'$-dicarboxylic acid and 4 mL thionyl chloride (5.5×10^{-2} mol) was refluxed under a nitrogen atmosphere. After 3 h the excess thionyl chloride was removed under reduced pressure and a solution containing 450 μL of triethylamine (3.2×10^{-3} mol) in 5 mL of dichloromethane was added. This solution was transferred to a flask containing 712 mg (3.1×10^{-3}mol) of aminopropylsilatrane **10** and 15 mL of toluene was added. The reaction mixture was maintained at 60°C for 1 h and then stirred at room temperature for 12 h. The solvent was removed under reduced pressure and the product was purified by column chromatography on silica gel using chloroform containing 10% methanol as the eluent to yield 170 mg (17%) of the desired product. ^{1}H NMR (300 MHz, DMSO) δ 8.85–8.80 (2H, m, Ar–H), 8.76 (2H, s, Ar–H), 7.84–7.81 (2H, m, Ar–H), 3.60 (12H, t, *J*=6 Hz, CH_2–O), 3.17 (4H, q, CH_2), 2.78 (12H, t, *J*=6 Hz, CH_2–N), 1.56 (4H, m, CH_2), 0.19 (4H, t, *J*=8.5 Hz, CH_2–Si). MALDI-TOF-MS m/z calcd for $C_{30}H_{44}N_6O_8Si_2$ + 1(H) (m+H) 673.28, obsd 673.28.

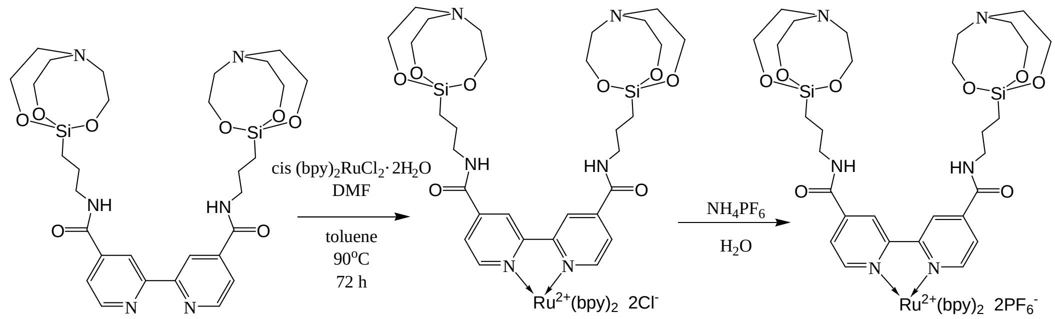

15 **16**

Ru(bpy)$_3$-sil (16). To a round bottom flask was added 31.8 mg (6.6 x 10^{-3} mol) of cis-(bpy)$_2$RuCl$_2$·2H$_2$O and 48.0 mg (7.1 x 10^{-3} mol) of bpy-sil **15** in 3 mL of dimethylformamide. The solution was heated to 90° C under a nitrogen atmosphere for 72 h. The solvent was removed under reduced pressure. Addition of water dissolved the product, and the residual starting material was removed by filtration. Excess NH$_4$PF$_6$ was added to the filtrate. The resulting solution was extracted with ethyl acetate and the solvent was removed under reduced pressure to yield a solid red product. Yield: 71.8 mg (79%). ^{1}H NMR (400 MHz, CD$_3$OD) δ 9.06 (2H, d, *J*=1 Hz, Ar-H), 8.67 (4H, dd, *J*=3 Hz, 2.5 Hz, Ar-H), 8.11 (4H, m, Ar-H), 7.96 (2H, m, Ar-H), 7.80 (6H, m, Ar-H), 7.48 (4H, m, Ar-H), 3.72 (12H, t, *J*=6 Hz, CH$_2$-O), 3.35 (4H, t, *J*=7 Hz, CH$_2$), 2.87 (12H, t, *J*=6 Hz, CH$_2$-N), 1.69 (4H, m, CH$_2$), 0.35 (4H, m, CH$_2$-Si). MALDI-TOF-MS m/z calcd for $C_{50}H_{60}N_{10}O_8Si_2$ + PF$_6$ 1231.22, obsd 1231.28.

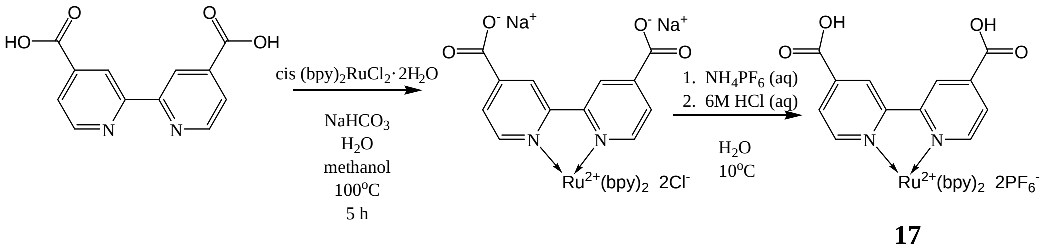

17

Ru(bpy)$_3$-COOH (17). A procedure from Sprintschnik et al. was followed with modification.[101] To a flask was added 102.9 mg (2.1×10^{-4} mol) of cis-$(bpy)_2RuCl_2\cdot 2H_2O$, 65.3 mg (2.7×10^{-4} mol) 2,2'-bipyridyl-4,4'-dicarboxylic acid, 62.8 mg of $NaHCO_3$ (7.5×10^{-4} mol), 3 mL of water, and 2 mL of methanol. The solution was heated to 100°C for 5 h under a nitrogen atmosphere. Excess NH_4PF_6 was added and the reaction mixture was cooled to 10°C. The reaction mixture was acidified using 120 μL of 6M aqueous HCl and the red precipitate was filtered to yield 190 mg (95%) of product. UV–Vis ($\lambda_{max,}$ acetonitrile) 458, 430 (sh) nm.

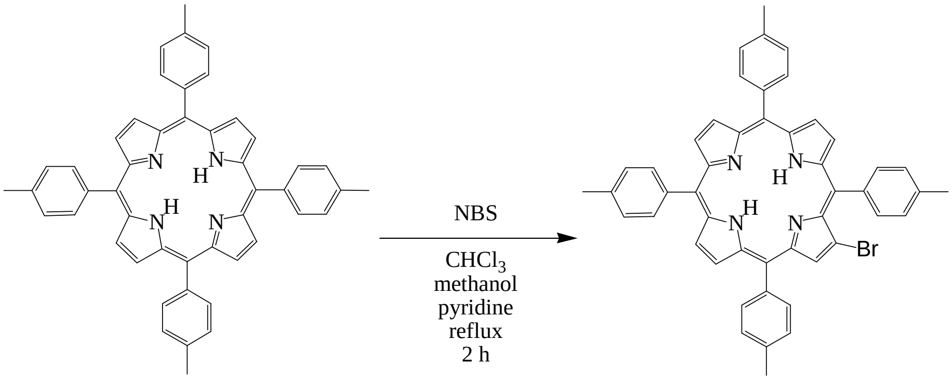

18

TTP-β-Br (18). In a dry round bottom flask was dissolved 260 mg TTP (3.9×10^{-4} mol) in a mixture of 130 mL chloroform, 1 mL pyridine, and 200 μL anhydrous methanol. The reaction was stirred and heated to reflux under a nitrogen atmosphere. Over a 2 h period, N-bromosuccinimide was added in increments totalling 80 mg (4.5×10^{-4} mol). After an additional 2 h at reflux, the reaction was cooled to room temperature and washed with water, and the solvent was removed under reduced pressure. The crude material was precipitated on the rotovap from dichloromethane and methanol. The precipitated porphyrin products were obtained by filtration and dried under reduced pressure. The product was purified by chromatography on silica gel (activated by heating overnight at 100^{o}C) using a 3:2 mixture of hexanes / dichloromethane as eluent (115 mg, 39%). ^{1}H NMR (400 MHz, $CDCl_3$) δ 8.91-8.75 (7H, m, *β*-H), 8.1-8.04 (6H, m, Ar-H), 7.95 (2H, d, *J*=8 Hz, Ar-H), 7.56-7.51 (8H, m, Ar-H), 2.70 (12H, s, Ar-CH_3), -2.85 (2H, s, NH). MALDI-TOF-MS m/z calcd for $C_{48}H_{37}BrN_4$ 750.2, obsd 750.2.

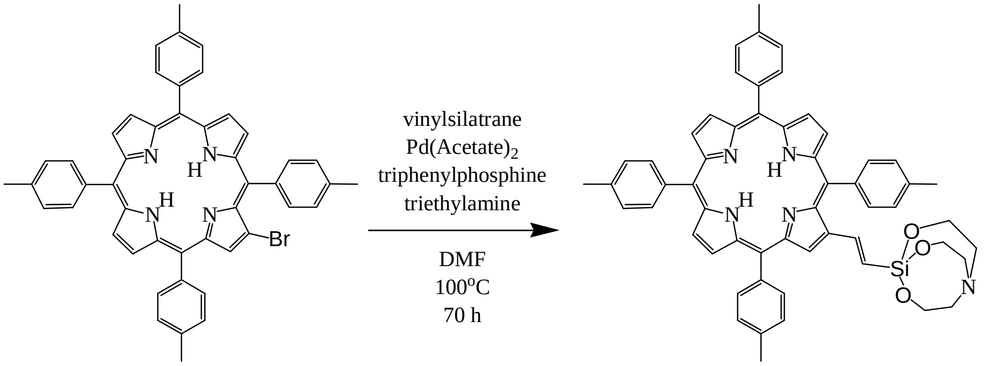

18 **19**

TTP-β-sil (19). In a dry round bottom flask was dissolved 81 mg TTP-β-Br **18** (1.1 x 10^{-4} mol), 48 mg vinylsilatrane **4** (2.4 x 10^{-4} mol), 8.5 mg palladium(II) acetate (3.8 x 10^{-5} mol), 30 mg triphenylphosphine (1.1 x 10^{-4} mol), and 200 μL triethylamine in 30 mL DMF. The reaction was kept under a nitrogen atmosphere and heated to 100^{o}C for 70 h. After cooling, the solvent was removed under reduced pressure. The crude products were purified by column chromatography on silica gel. TTP and brominated starting material were flushed from the column using dichloromethane as the eluent. Addition of 1% methanol to the dichloromethane eluent eluted the desired porphyrin. The solid was sonicated in a 50:50 methanol/water solution and filtered to yield the desired porphyrin product (21 mg, 22%). ^{1}H NMR (400 MHz, $CDCl_3$) δ 9.06 (1H, s, *β*-H), 8.85-8.83 (2H, m, *β*-H), 8.75 (2H, s, *β*-H), 8.70 (1H, d, *J*=5 Hz, *β*-H) 8.64 (1H, d, *J*=5 Hz, *β*-H), 8.09-7.99 (8H, m, Ar-H), 7.54-7.48 (8H, m, Ar-H), 7.06 (1H, d, *J*=18 Hz, *β*-CH), 6.65 (1H, d, *J*=18 Hz, CH-Si), 3.82 (6H, t, *J*=6 Hz, O-CH_2), 2.83 (6H, t, *J*=6 Hz, N-CH_2), 2.69 (12H, m, Ar-CH_3), -2.67 (2H, br s, NH). MALDI-TOF-MS m/z calcd for $C_{56}H_{51}N_5O_3Si$ 869.4, obsd 869.2.

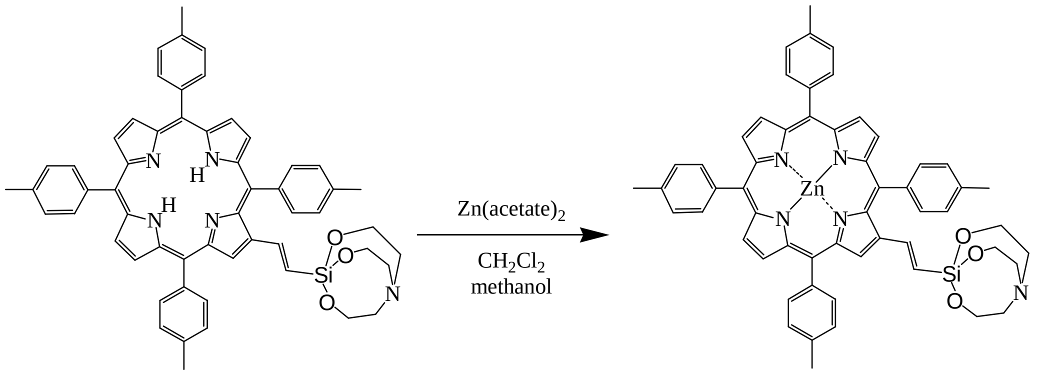

19 **Zn-19**

Zn-TTP-sil (Zn-19). TTP-β-sil was metalated using the general metalation procedure. ^{1}H NMR (400 MHz, $CDCl_3$) δ 9.11 (1H, s, *β*-H), 8.91-8.88 (4H, m, *β*-H), 8.85 (1H, d, *J*=4 Hz, *β*-H) 8.77 (1H, d, *J*=4 Hz, *β*-H), 8.07 (4H, d, *J*=8 Hz, Ar-H), 8.02 (2H, d, *J*=8 Hz, Ar-H), 7.98 (2H, d, *J*=8 Hz, Ar-H), 7.52-7.48 (8H, m, Ar-H), 7.04 (1H, d, *J*=18 Hz, *β*-CH), 6.52 (1H, d, *J*=18 Hz, CH-Si), 3.81 (6H, t, *J*=6 Hz, O-CH_2), 2.82 (6H, t, *J*=6 Hz, N-CH_2), 2.69 (12H, m, Ar-CH_3). MALDI-TOF-MS m/z calcd for $C_{56}H_{49}N_5O_3SiZn$ 931.3, obsd 931.4.

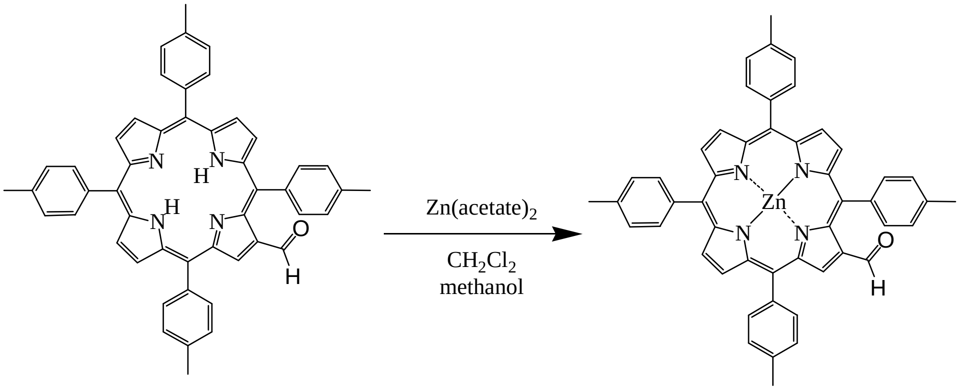

20 **Zn-20**

Zn-TTP-β-formyl (Zn-20). β-Formyl-TTP **20** was metalated using the general metalation procedure. ^{1}H NMR (400 MHz, CDCl$_3$) δ 9.56 (1H, s, *β*-H), 9.36 (1H, s, CHO), 8.97-8.91 (6H, m, *β*-H), 8.11-8.04 (8H, m, Ar-H), 7.57-7.53 (8H, m, Ar-H), 2.71-2.70 (12H, m, Ar-CH$_3$). MALDI-TOF-MS m/z calcd for $C_{49}H_{36}N_4OZn$ 760.2, obsd 760.2.

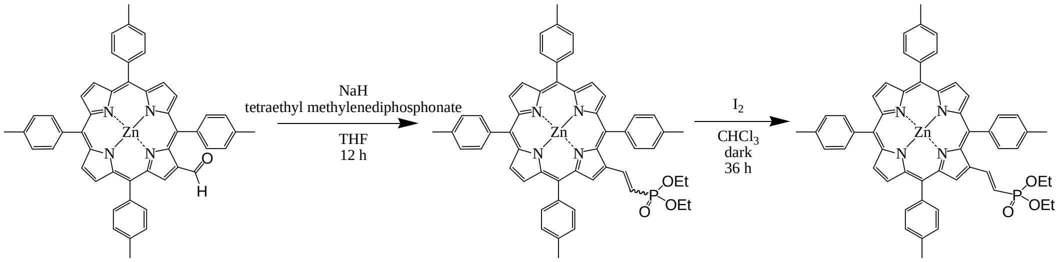

Zn-20 **Zn-21**

Zn-TTP-diethyl phosphonate (Zn-21). The porphyrin was prepared following a modified procedure from Bonfantini et al.[103-104] A dry round bottom flask with 40 mL distilled THF was flushed with nitrogen while adding 37 mg sodium hydride (9.3 x 10^{-4} mol). The solution was cooled in an ice bath and 69 mg of Zn-TTP-β–formyl **Zn-20** (9.1 x 10^{-5} mol) and 120 μL of tetraethyl methylenediphosphonate (4.8 x 10^{-4} mol) were added. It appeared that the solvent had become tainted with water, and additional sodium hydride was added. The reaction was stirred under a nitrogen atmosphere at room temperature overnight, and then quenched using a saturated ammonium chloride solution. The reaction mixture was placed in a separatory funnel with chloroform and a brine solution. The organic layer was washed with water and the solvent was then removed under reduced pressure. The crude product was redissolved in a mixture of dichloromethane and methanol, with subsequent removal of the dichloromethane by distillation under reduced pressure. The porphyrin was precipitated by addition of water, and then filtered. The crude material was purified by column chromatography on silica gel using 2% methanol in dichloromethane as eluent to obtain the 36 mg of a cis/trans mixture of the desired porphyrin. The porphyrin was dissolved in 25 mL chloroform and 8 mg I_2 (3.2×10^{-5} mol) was added. The reaction was allowed to stir for 36 h under a nitrogen atmosphere in the dark. The reaction was transferred to a separatory funnel and quenched by adding excess aqueous sodium bisulfite. The organic layer was washed with water and the solvent was removed under reduced pressure. Demetalation by acidic solutions during workup required re-metalation using the general metalation procedure, and 35 mg of **Zn-21** was isolated (43%). ^{1}H NMR (400 MHz, $CDCl_3$, ^{31}P decoupled) δ 8.89-8.75 (7H, m, β-H), 8.08-8.02 (6H, m, Ar-H), 7.68 (2H, d, *J*=8 Hz, Ar-H), 7.53 (2H, d, *J*=8 Hz, Ar-H), 7.47-7.44 (4H, m, Ar-H), 6.97 (2H, br d, *J*=7 Hz, Ar-H), 6.34 (1H, br d, *J*=17 Hz, β-CH), 5.19 (1H, br d, *J*=17 Hz, CH-P), 3.06 (4H, broad, P-CH_2), 2.75 (3H, s, Ar-CH_3), 2.645 (3H, s, Ar-CH_3), 2.640 (3H, s, Ar-CH_3), 2.35 (3H, s, Ar-CH_3), 0.86 (6H, t, CH_3). MALDI-TOF-MS m/z calcd for $C_{54}H_{47}N_4O_3PZn$ 894.3, obsd 894.4.

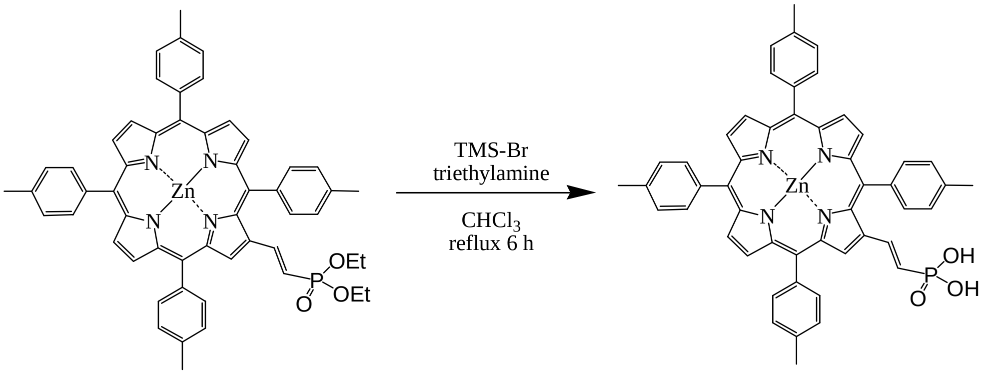

Zn-21 **Zn-22**

Zn-TTP-PO$_3$H$_2$ (Zn-22). The porphyrin was prepared following a procedure by Muthukumaran et al.[150] In a dry round bottom flask 37 mg of **Zn-21** (4.1 x 10^{-5} mol) and 200 μL triethylamine (1.4 x 10^{-3} mol) was dissolved in 25 mL chloroform, under a nitrogen atmosphere, and 150 μL bromotrimethylsilane was added dropwise. A reflux condenser was attached and the solution heated to reflux under a nitrogen atmosphere for 6 h. The reaction was cooled and washed with brine, dilute citric acid, and then water. The solvent was removed, and the crude material was determined to be partially demetalated. The crude product was remetalated using a modified version of the general metalation procedure where after the bicarbonate wash the organic layer was washed with a dilute solution of polyphosphoric acid (~3% w/w). After metalation the product was determined to be >95% pure (35 mg, 100 %). MALDI-TOF-MS m/z calcd for $C_{50}H_{39}N_4O_3PZn$ + 1(H) 839.2, obsd 839.3.

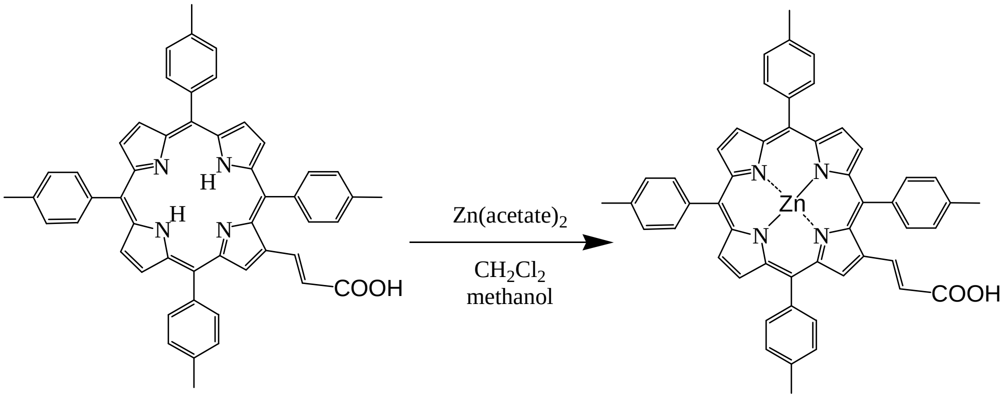

23 **Zn-23**

Zn-TTP-COOH (Zn-23). Metalation of **23** was performed using a modified version of the general porphyrin metalation procedure, where a dilute aqueous citric acid wash was performed after the bicarbonate wash in order to reprotonate the carboxylate group. MALDI-TOF-MS m/z calcd $C_{51}H_{38}N_4O_2Zn$ 802.2, obsd 802.2.

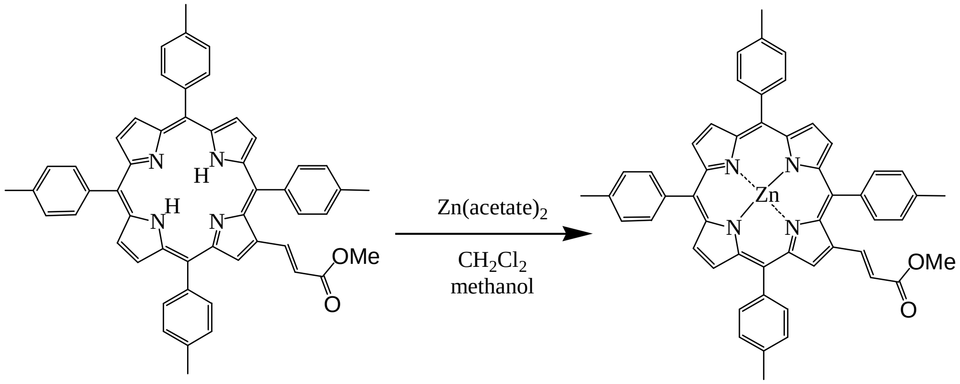

24 **Zn-24**

Zn-TTP-COOMe (Zn-24). Metalation of **24** was performed using the general porphyrin metalation procedure. ^{1}H NMR (400 MHz, $CDCl_3$) δ 9.08 (1H, s, *β*-H), 8.94-8.89 (6H, m, *β*-H), 8.08-8.05 (6H, m, Ar-H), 7.95 (2H, d, *J*=8Hz, Ar-H), 7.55-7.51 (8H, m, Ar-H), 7.37 (1H, d, *J*=15Hz, *β*-CH), 6.48 (1H, d, *J*=15Hz, CH), 3.73 (3H, s, O-CH_3), 2.72 (3H, s, Ar-CH_3), 2.70 (3H, s, Ar-CH_3), 2.69 (6H, s, Ar-CH_3). MALDI-TOF-MS m/z calcd for $C_{52}H_{40}N_4O_2$ Zn 816.2, obsd 816.3.

Electrochemistry. See Chapter 6.1 for general electrochemical instrumentation and procedures. Cyclic voltammetry was performed using a 1.6 mm diameter platinum electrode in a standard 3-electrode cell setup with platinum counter electrode and pseudo Ag/AgCl reference electrode. The electrolyte consisted of a solution of 100 mM tetra-*n*-butylammonium hexafluorophosphate ($TBAPF_6$) in dichloromethane.

Colloidal nanoparticulate solutions. SnO_2 solution.[76] Aqueous colloidal nanoparticle solutions of 12.8% SnO_2 /13.1% PEG / 0.43% NH_3 (w/w) were prepared by adding 0.46 g polyethylene glycol (Fluka - 17500 MW with bisphenol-A) and 50 μL of 30% aqueous ammonia to 3.0 g of commercial SnO_2 nanoparticle colloid (Alfa Aesar - 15% SnO_2 nanoparticles in water). The colloidal solution was stirred overnight to insure homogeneity.

TiO_2 solution. The colloid was prepared using a modified procedure from Kang et al.[151] A solution of 26 mL distilled water and 8.5 mL glacial acetic acid was cooled in an ice bath. Separately, 1 mL isopropanol and 4 mL titanium isopropoxide (Alfa Aesar 97%) were mixed, and the mixture was then added dropwise to the cooled solution with stirring. A reflux condenser was attached, and the mixture was heated at 110°C for 4.5 h. After cooling, 32 mL of the opaque colloid was transferred to a Teflon® container and placed in an acid digestion vessel autoclave (Parr – model 4744). The vessel was heated in an oven at 200°C for 12 h and then allowed to cool to room temperature. The colloid was redispersed into solution using a sonic horn (Branson Sonic Power - Sonifier cell disruptor - model 350) with continuous sonication for 2 min, a 50/50 pulse for 2 min, and continuous sonication for 1 min to fully disperse the material. The colloid was placed in a round bottom flask and concentrated to 4.2 mL (4.6 grams) using a rotary evaporator under reduced pressure. The concentrated colloid was mixed with 120 mg each of PEG (Fluka - 17500 MW with bisphenol-A) and PEO (Aldrich – 100000 MW). Another ~0.8 mL water was added to decrease the viscosity. The colloidal solution was stirred overnight to insure homogeneity.

Preparation and characterization of SnO_2 and TiO_2 electrodes. FTO was rinsed with acetone, water, and ethanol. An area on the substrate was then defined using Scotch® transparent tape (51 μm thick). The nanoparticle colloidal solution was spread over the tape mask using the doctor blade method with a razor blade or glass rod. The resulting film was dried in air, generally overnight. The tape was removed, and the films were heated in an oven at 450^{o}C for 1 hour. Profilometry was used to determine the thickness of TiO_2 and SnO_2 electrodes prepared using the above procedure. The results showed a narrow thickness range that varied between 3 μm and 3.2 μm for TiO_2 and between 3.9 μm and 4.2 μm for SnO_2 electrodes.

Sensitization of SnO_2. Porphyrins with the carboxylic acid linker were dissolved in ethyl acetate (~0.2 mM), and electrodes were soaked at room temperature for a minimum of 3 h. Porphyrins with the silatrane linker were dissolved in toluene, and electrodes were soaked at 80°C for a minimum of 3 h. Electrodes sensitized with silatrane porphyrins were then soaked in chloroform with

~20% ethanol to remove unbound porphyrin. Ruthenium compounds were dissolved in acetonitrile, and electrodes were soaked at 80°C. Electrodes in the silatrane functionalized ruthenium dye solution were soaked for 5 h while electrodes in the carboxylic acid ruthenium dye solution were soaked for a shorter time to achieve comparable absorbance to the silatrane electrodes. After sensitization, electrodes containing ruthenium silatrane dye were soaked in acetonitrile with 10% ethanol to remove unbound dye.

Sensitization of TiO_2. Porphyrins were dissolved in toluene (~0.2 mM), and electrodes were soaked at 90^{o}C for 1 h, rinsed in toluene and acetonitrile, and then dried in air.

Counter electrodes for PEC. Platinized FTO (Pt/FTO) glass for use as counter electrodes in regenerative-type PEC were prepared as described in Chapter 6.2. Hg_2SO_4 / Hg electrodes were prepared by packing mercury metal and then mercurous sulfate into a glass cylinder in to one end of which was sealed a platinum wire as shown in Figure 52. Inert glass wool was used to keep the materials from leaching out. The electrode was stored in a saturated aqueous solution of potassium sulfate.

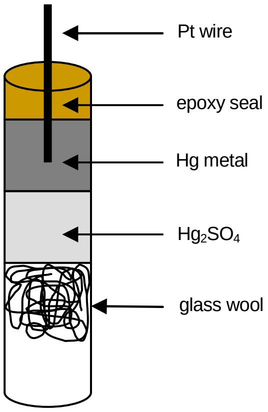

Figure 52. Hg_2SO_4 / Hg electrode

PEC fabrication. Non-regenerative. A Teflon® PEC apparatus was used for non-regenerative cells, and is shown in Figure 53. Two Teflon® blocks with 13 mm diameter open chambers (3.5 mL) were connected by a Nafion® N-112 proton exchange membrane via 14 mm I.D. rubber o-ring connections. The outside of each Teflon® block chamber was sealed using either transparent glass or the sensitized FTO electrode situated between 14 mm I.D. rubber o-ring connections of the chamber and an aluminum plate with 13 mm diameter aperture to allow for illumination. The apparatus was assembled using two screws to sandwich the materials and seal all o-ring connections.

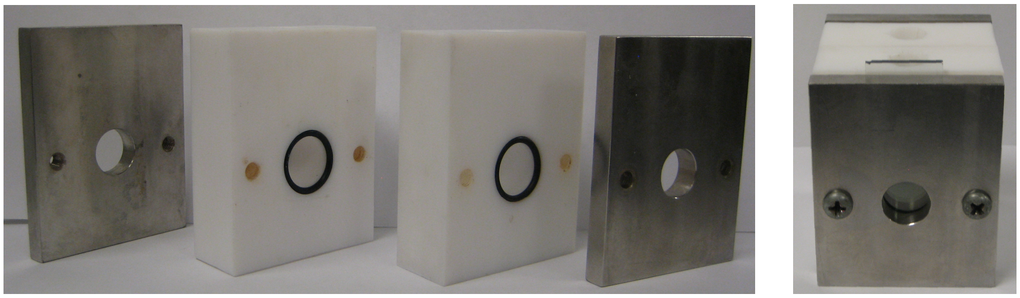

Figure 53. Non-regenerative PEC assembly. Teflon® and aluminum blocks (left) and fully assembled (right)

Regenerative. Fabrication involved sealing a sensitized electrode to a platinized counterelectrode (Pt/FTO) in a face-to-face design using a heat-sealable polymer (Solaronix, Surlyn®, 25 μm) to confine the active area of the electrodes and act as a high-resistance spacer between them. The Pt/FTO holes were used as the corners of the heat-seal polymer frame. The sensitized electrode was placed on top, and the polymer melted on a hotplate. The electrolyte solution, the specifics of which are provided below, could be introduced via the holes, with a thin microscope slide glass cover used to cover the holes and limit solvent evaporation.

PEC testing. Non-regenerative cell. Photocurrent was measured in a two-chambered Teflon cell with a Nafion® membrane barrier as described above. Sensitized SnO_2 electrodes with a 1.45 cm^2 illumination area were prepared. The anode compartment contained a buffered aqueous solution (250 mM *N*-tris(hydroxymethyl)methyl-2-aminoethane-sulfonic acid (TES) / 100 mM KCl) at a pH of 7.35 containing 10-15 mM *β*-nicotinamide adenine dinucleotide reduced disodium salt (NADH) as a sacrificial electron donor. The solution was continuously bubbled with argon. The cathode compartment contained saturated aqueous K_2SO_4 and a Hg_2SO_4/Hg electrode. See Chapter 6.1 for PEC testing procedures.

Regenerative cell. Dye sensitized SnO_2 or TiO_2 electrodes were cut into 1 cm × 1 cm electrodes which were then made into regenerative photoelectrochemical cells as described above. The regenerative electrolyte consisted of 100 mM LiI, 50 mM I_2, 650 mM 1-butyl-3-methylimidazolium iodide, and 50 mM 4-*tert*-butylpyridine in a 85:15 acetonitrile:valeronitrile solvent mixture. See Chapter 6.1 for PEC testing procedures.

Transient absorption spectroscopy. All nanosecond transient absorption spectroscopy experiments were performed by Dr. Amy Keirstead.[76] Time-resolved transient absorption experiments were carried out using a nanosecond laser flash photolysis system. The excitation source was an Opotek optical parametric oscillator pumped by the third harmonic of a Continuum Surelite Nd:YAG laser. The pulse width was 5 ns and the repetition rate was 5 Hz. The detection system consisted of a 75 W xenon-arc lamp (Spectra Physics model 66905), a double grating monochromator (Spectral Products, 1/4 m Digikröm), and a silicon photodiode (Thorlabs, Inc., DET210) coupled to a voltage amplifier. The signal was captured by a Tektronix TDS 303213 digitizing oscilloscope and transferred to a PC that controls the laser system using software written by Ultrafast Systems LLC. In all cases the sample electrode was placed in an aqueous sodium borate buffer pH 7.35, aligned 45^o to the probe beam, and excited from the back side. Lifetime distributions were calculated using TimeMaster software (Photon Technology International). The chosen fitting function contained 200 fixed exponential terms with logarithmically spaced lifetimes ranging from 100 ns to 1 ms and variable pre-exponentials.

Dye leaching study. TiO_2 electrodes were sensitized with porphyrin using the procedure described above. Porphyrin was leached from the sensitized TiO_2 electrode surface using a strongly alkaline solution consisting of a mixture of THF / methanol / 0.5% aqueous Cs_2CO_3 (w/w) in a 10:5:2 ratio. Electrodes were soaked at room temperature for 20 min and rinsed with a THF / water solution followed by an acetonitrile wash. For ‘cured’ electrodes, TiO_2 was sensitized as described previously and then heated at ~80°C for 1 h in a solution of acetonitrile containing 0.6% water.

6.4. Experimental Procedures for Chapter 4

Materials. $Cu(ClO_4)_2 \cdot 6H_2O$ (Alfa Aesar, reagent grade) and $Cu(BF_4)_2 \cdot 6H_2O$ (Strem Chemicals, 99%) were partially dehydrated under vacuum and stored in a desiccator. Nitromethane (Fisher, ACS grade) was stored on 4Å molecular sieves.

Synthesis. Porphyrins **1** and **H_2-28** were provided by Dr. Paul Liddell.

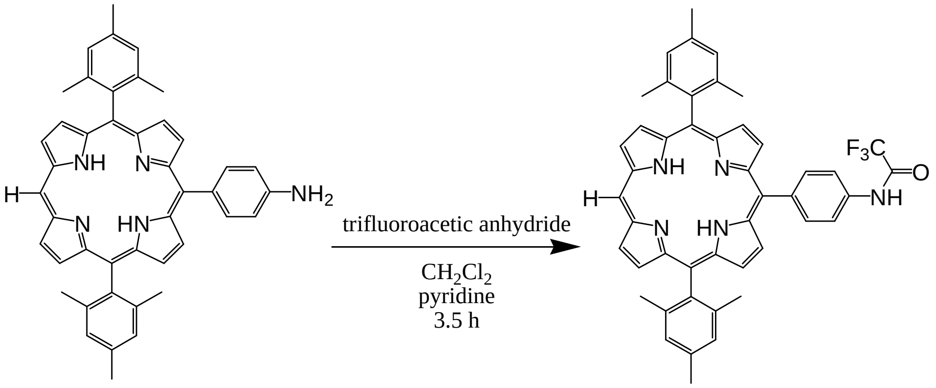

1

H_2-25

H_2-25. A solution of 164 mg of porphyrin **1** (2.57×10^{-4} mol) in 40 mL dichloromethane and 200 μL pyridine was cooled in an ice bath under a nitrogen atmosphere. Trifluoroacetic anhydride (178 μL, 1.28×10^{-3} mol, 5 equivalents) was added and the solution was stirred for 3.5 h. The reaction mixture was washed with saturated aqueous sodium bicarbonate solution followed by a wash with water to yield 180 mg porphyrin (95%). ^{1}H NMR (400 MHz, $CDCl_3$) δ 10.12 (1H, s, meso-H), 9.26 (2H, d, *J*=4 Hz, β-H), 8.83 (2 H, d, *J*=4 Hz, β-H), 8.77 (2H, d, *J*=5 Hz, β-H), 8.75 (2H, d, *J*=4 Hz, β-H), 8.24 (1H, s, N-H), 8.23 (2H, d, *J*=7 Hz, Ar-H), 7.93 (2H, d, *J*=7 Hz, Ar-H), 7.29 (4H, s, Ar-H), 2.63 (6H, s, Ar-CH_3) 1.83 (12H, s, Ar-CH_3), -2.90 (2H, s, N-H); MALDI-TOF-MS m/z calcd for $C_{46}H_{38}F_3N_5O$ 733.3, obsd 733.4; UV-visible ($\lambda_{max,}$ CH_2Cl_2) 412, 508, 540, 583, 638 nm.

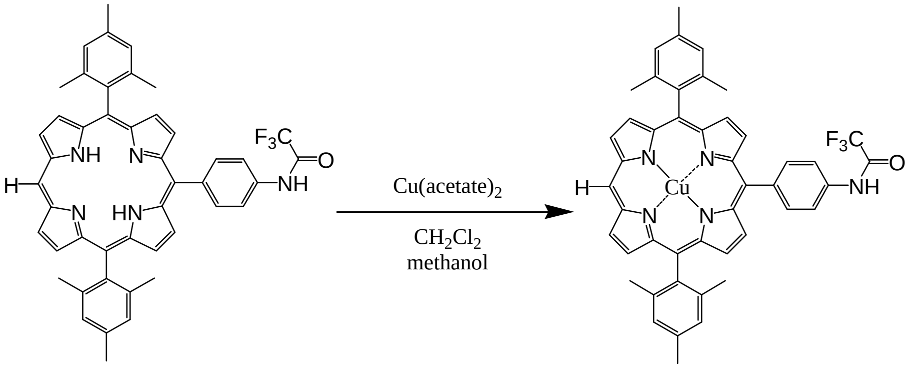

H$_2$-25 **Cu-25**

Cu-25. The porphyrin **Cu-25** was synthesized from **H$_2$-25** using the general procedure for porphyrin metalation described above. MALDI-TOF-MS m/z calcd for $C_{46}H_{36}CuF_3N_5O$ 794.2, obsd 794.4; UV-visible ($\lambda_{max,}$ CH_2Cl_2) 410, 534, 567 nm.

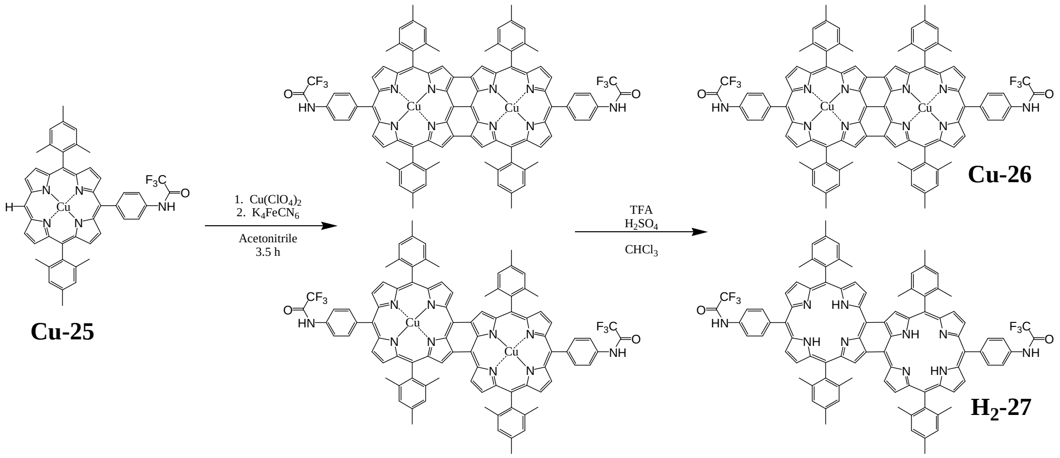

Porphyrin dimers 26 and 27. A solution of 179 mg of $Cu(ClO_4)_2$•6 H_2O (4.83×10^{-4} mol, 3.3 equivalents) in 4 mL acetonitrile was added to a mixture of 116 mg porphyrin **Cu-25** (1.46×10^{-4} mol) in 35 mL of acetonitrile. All porphyrin immediately dissolved, and the purple solution was stirred under a nitrogen atmosphere for 3.5 h. The reaction was quenched with an aqueous solution of 400 mg of potassium ferrocyanide in 40 mL of distilled water, and 50 mL chloroform was added. The organic layer was washed three times with 50 mL of water and then the solvent was removed under reduced pressure. The porphyrin was stirred in an ice cold solution of 20 mL of trifluoroacetic acid, 10 mL of chloroform, and 6.5 mL of concentrated sulfuric acid for 1.5 h. The solution was then added to 50 mL of cold distilled water and extracted twice with 30 mL of chloroform. The combined organic extracts were washed with distilled water, saturated aqueous sodium bicarbonate containing EDTA, and again with distilled water (50 mL each). The organic layer was dried under reduced pressure. Repeated flash column chromatography was performed on silica gel using a 3:2 mixture of dichloromethane / hexanes as eluent to yield Cu-triply connected porphyrin **Cu-26**

(33 mg, 29%) and free base doubly connected porphyrin **H_2-27** (36 mg, 34%) as the first and second major band, respectively. For **Cu-26**: MALDI-TOF-MS m/z calcd for $C_{92}H_{66}Cu_2F_6N_{10}O_2$ 1584.4, obsd 1584.6; UV-visible-NIR ($\lambda_{max,}$ CH_2Cl_2) 409, 557, 577, 911(sh), 1002 nm. For **H_2-27**: ^{1}H NMR (400 MHz, $CDCl_3$) δ 9.25 (2H, d, *J*=5 Hz, β-H), 8.83 (2H, s, β-H), 8.46 (2H, d, *J*=5 Hz, β-H), 8.31 (2H, d, *J*=5 Hz, β-H), 8.26 (2H, d, *J*=5 Hz, β-H), 8.24 (2H, d, *J*=5 Hz, β-H), 8.20 (2H, d, *J*=5 Hz, β-H), 8.17 (2H, s, N-H), 8.13 (4H, d, *J*=8 Hz, Ar-H), 7.93 (4H, d, *J*=8 Hz, Ar-H), 7.31 (4H, s, Ar-H), 7.25 (4H, s, Ar-H), 2.66 (6H, s, Ar-CH_3), 2.61 (6H, s, Ar-CH_3), 2.08 (12H, s, Ar-CH_3), 1.95 (12H, s, Ar-CH_3), 0.71 (4H, s, N-H); MALDI-TOF-MS m/z calcd for $C_{92}H_{72}F_6N_{10}O_2$ 1463.6, obsd 1463.7; UV-visible-NIR ($\lambda_{max,}$ CH_2Cl_2) 424, 499, 561, 611, 739(sh), 814 nm.

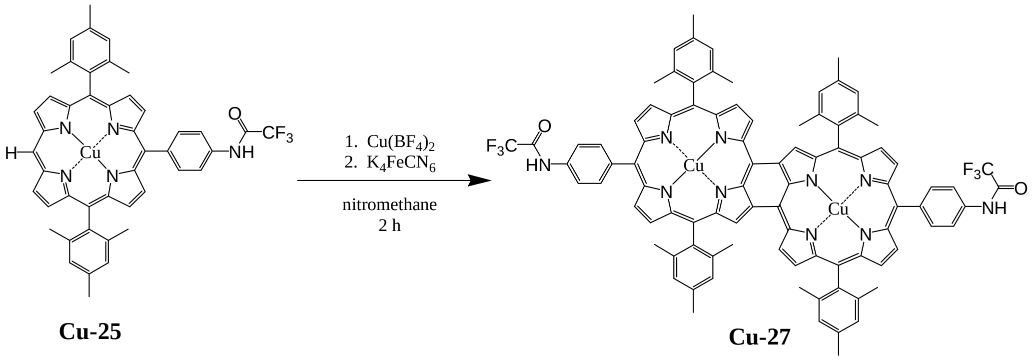

Cu-25

Cu-27

Porphyrin dimer Cu-27. Synthesis method 1. A solution of 55 mg of $Cu(BF_4)_2$•6 H_2O (1.6×10^{-4} mol, 3 equivalents of porphyrin) in 10 mL nitromethane was added to a mixture of 42 mg porphyrin **Cu-25** (5.3×10^{-5} mol) in 20 mL of nitromethane. All porphyrin immediately dissolved and the solution immediately turned to a dark red. The solution was stirred under a nitrogen atmosphere for 2 h. The reaction was quenched with an aqueous solution of 1 g of potassium ferrocyanide in 30 mL of distilled water, followed by the addition of 50 mL dichloromethane. The organic was washed twice with 50 mL of water and then the solvent was removed under reduced pressure to yield porphyrin product. TLC was performed using a 1:1 mixture of dichloromethane / hexanes and mass spectrometry each provided evidence for a single porphyrin product **Cu-27** (41 mg, 98%). MALDI-TOF-MS m/z calcd for $C_{92}H_{68}Cu_2F_6N_{10}O_2$ 1586.4, obsd 1586.2; UV-visible ($\lambda_{max,}$ CH_2Cl_2) 418, 487 (sh), 553, 629, 702 (sh), 768 nm.

Synthesis method 2. Dimer **Cu-27** was also prepared from **H_2-27** as described by the general procedure for porphyrin metalation given above.

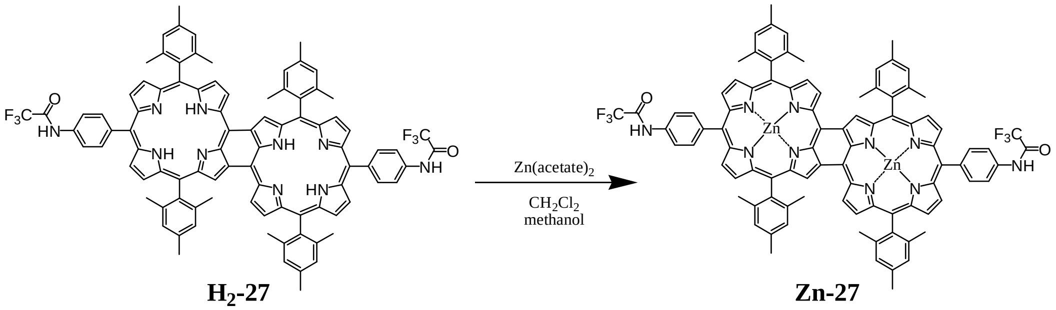

H_2-27 **Zn-27**

Zn-27. This material was prepared from **H_2-27** as specified by the general procedure for porphyrin metalation. ^{1}H NMR (400 MHz, $CDCl_3$) δ 9.47 (2H, d, *J*=5 Hz, β-H), 9.03 (2H, s, β-H), 8.57 (2H, d, *J*=5 Hz, β-H), 8.39 (4H, m, β-H), 8.33 (4H, m, β-H), 8.16 (2H, s, N-H), 8.14 (4H, d, *J*=8 Hz, Ar-H), 7.91 (4H, d, *J*=8 Hz, Ar-H), 7.31 (4H, s, Ar-H), 7.25 (4H, s, Ar-H), 2.66 (6H, s, Ar-CH_3), 2.62 (6H, s, Ar-CH_3), 2.08 (12H, s, Ar-CH_3), 1.95 (12H, s, Ar-CH_3); MALDI-TOF-MS m/z calcd for $C_{92}H_{68}F_6N_{10}O_2Zn_2$ 1590.4, obsd 1590.5; UV-visible-NIR ($\lambda_{max,}$ CH_2Cl_2) 422, 492, 551(sh), 563, 593(sh), 638, 718(sh), 787 nm.

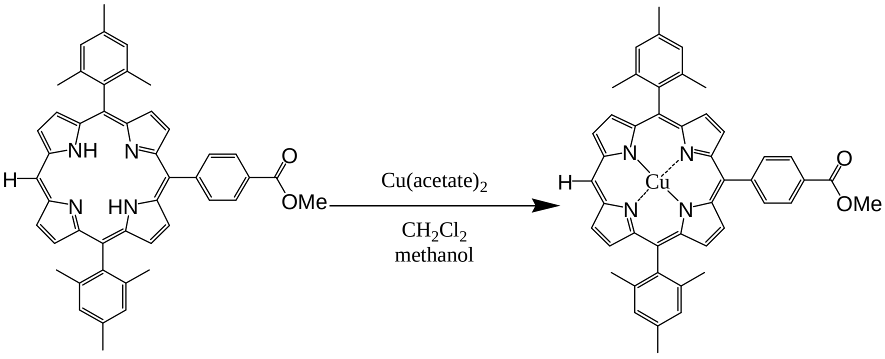

H$_2$-28 **Cu-28**

Cu-28. This material was prepared from **H$_2$-28** as specified by the general procedure for porphyrin metalation. MALDI-TOF-MS m/z calcd for $C_{46}H_{38}CuN_4O_2$ 741.2, obsd 741.3; UV-visible ($\lambda_{max,}$ CH_2Cl_2) 410, 534, 567 nm.

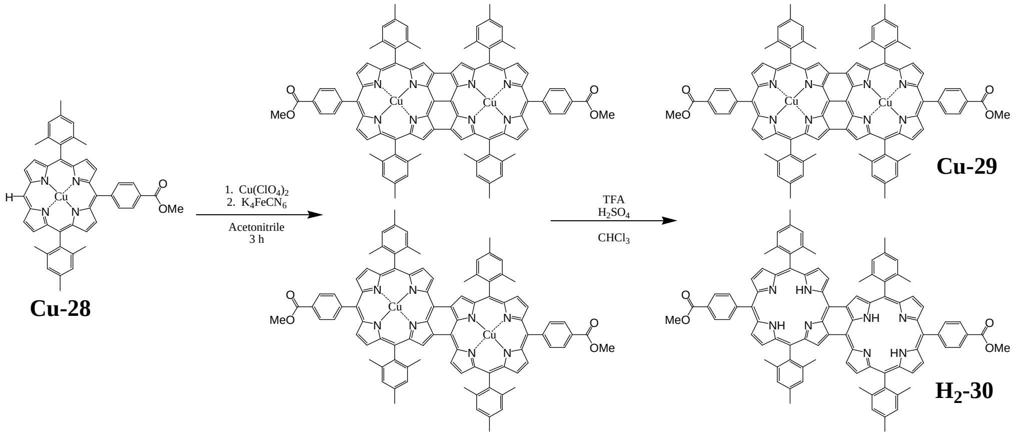

Porphyrin dimers 29 and 30. A solution of 200 mg of $Cu(ClO_4)_2$•6 H_2O (5.40 × 10^{-4} mol, 3.3 equivalents) in 5 mL of acetonitrile was added to a mixture of 123 mg of porphyrin **Cu-28** (1.65 × 10^{-4} mol) in 40 mL of acetonitrile. All porphyrin immediately dissolved and the solution slowly turned purple. The solution was stirred under a nitrogen atmosphere for 3 h. The reaction was then quenched with a solution of 350 mg of potassium ferrocyanide in 50 mL of distilled water, followed by the addition of 50 mL. The organic layer was washed three times with 60 mL of water followed by removal of the solvent under reduced pressure. The porphyrin was stirred for 30 minutes in a solution of 20 mL of trifluoroacetic acid, 10 mL of dichloromethane, and 6 mL of concentrated sulfuric acid. The solution was then poured into 50 mL of cold distilled water followed by the addition of 30 mL of chloroform. The organic layer was washed with distilled water, saturated aqueous sodium bicarbonate containing EDTA, and again with distilled water (50 mL each), followed by removal of the solvent under reduced pressure. Flash column chromatography using silica gel and a 1:1 mixture of dichloromethane / hexanes yielded Cu-triply connected **Cu-29** (38 mg, 31%) and free base double connected **H_2-30** (53 mg, 47%) as the first and second major band, respectively. For **Cu-29**: MALDI-TOF-MS m/z calcd for $C_{92}H_{70}Cu_2N_8O_4$ 1478.4, obsd 1478.5; UV-visible-NIR ($\lambda_{max,}$ CH_2Cl_2) 409, 557, 577, 909 (sh), 1002 nm. For **H_2-30**: ^1H NMR (400 MHz, $CDCl_3$) δ 9.25 (2H, d, *J*=5 Hz, β-H), 8.83 (2H, s, β-H), 8.46 (2H, d, *J*=5 Hz, β-H), 8.37 (4H, d, *J*=8 Hz, Ar-H), 8.29 (2H, d, *J*=5 Hz, β-H), 8.24 (4H, d, *J*=5 Hz, β-H), 8.20 (2H, d, *J*=5 Hz, β-H), 8.17 (4H, d, *J*=8 Hz, Ar-H), 7.30 (4H, s, Ar-H), 7.25 (4H, s, Ar-H), 4.08 (6H, s, O-CH_3), 2.66 (6H, s, Ar-CH_3), 2.61 (6H, s, Ar-CH_3), 2.08 (12H, s, Ar-CH_3), 1.95 (12H, s, Ar-CH_3), 0.71 (4H, s, N-H); MALDI-TOF-MS m/z calcd for $C_{92}H_{76}N_8O_4$ 1357.6, obsd 1357.6; UV-visible-NIR ($\lambda_{max,}$ CH_2Cl_2) 425, 499, 561, 610, 739(sh), 812 nm.

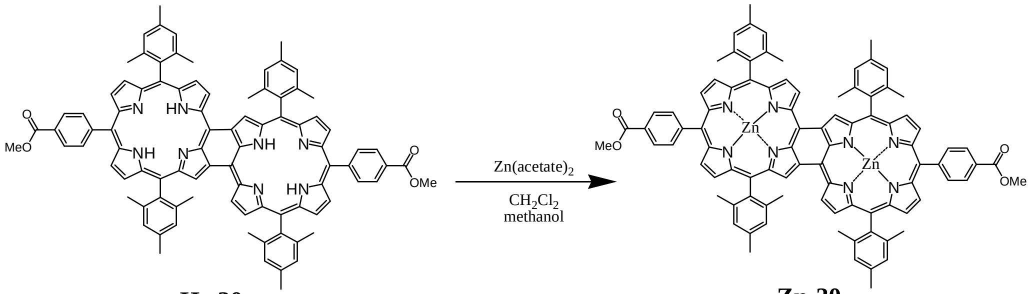

H$_2$-30 **Zn-30**

Zn-30. This material was prepared from **H$_2$-30** as specified by the general procedure for porphyrin metalation. ^{1}H NMR (400 MHz, CDCl$_3$) δ 9.47 (2H, d, *J*=5 Hz, β-H), 9.04 (2H, s, β-H), 8.57 (2H, d, *J*=5 Hz, β-H), 8.38-8.31 (12H, m, β-H and Ar-H), 8.19 (4H, d, *J*=8 Hz, Ar-H), 7.30 (4H, s, Ar-H), 7.26 (4H, s, Ar-H), 4.07 (6H, s, O-CH$_3$), 2.66 (6H, s, Ar-CH$_3$), 2.62 (6H, s, Ar-CH$_3$), 2.08 (12H, s, Ar-CH$_3$), 1.94 (12H, s, Ar-CH$_3$); MALDI-TOF-MS m/z calcd for $C_{92}H_{72}N_8O_4Zn_2$ 1484.4, obsd 1484.2; UV-visible-NIR ($\lambda_{max,}$ CH$_2$Cl$_2$) 423, 491, 550(sh), 564, 593(sh), 638, 718(sh), 786 nm.

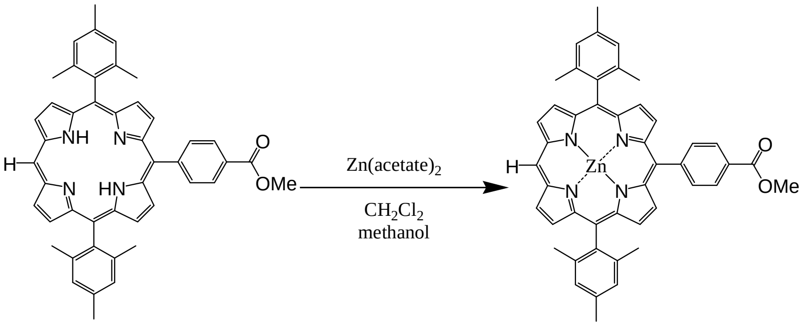

H$_2$-28 **Zn-28**

Zn-28. This material was prepared from **H$_2$-28** as specified by the general procedure for porphyrin metalation. ^{1}H NMR (400 MHz, CDCl$_3$) δ 10.19 (1H, s, meso-H), 9.36 (2H, d, *J*=3 Hz, β-H), 8.92 (2H, d, *J*=3 Hz, β-H), 8.84 (4H, s, β-H), 8.41 (2H, d, *J*=7 Hz, Ar-H), 8.32 (2H, d, *J*=7 Hz, Ar-H), 7.30 (4H, s, Ar-H), 4.09

(3H, s, O-CH_3), 2.65 (6H, s, Ar-CH_3), 1.82 (12H, s, Ar-CH_3). MALDI-TOF-MS m/z calcd for $C_{46}H_{38}N_4O_2Zn$ 742.2, obsd 742.0.

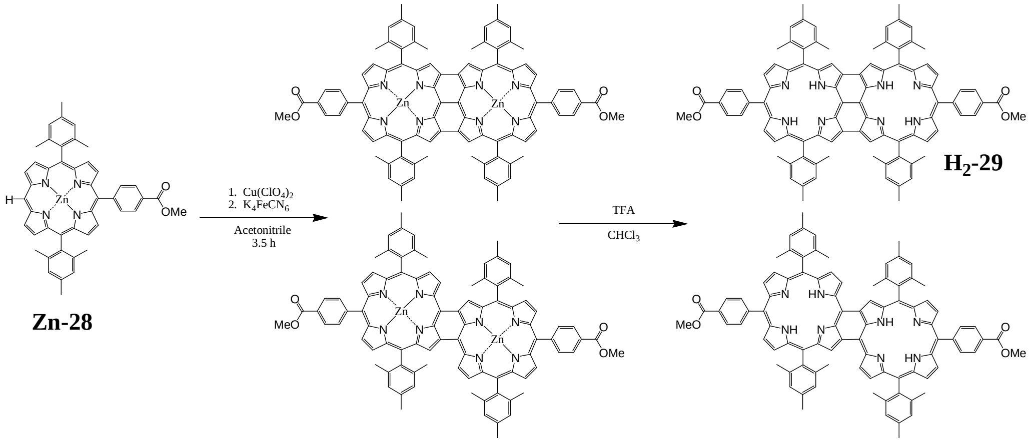

Zn-28

H_2-29

H_2-29. A solution of 142 mg of $Cu(ClO_4)_2$•6 H_2O (3.83×10^{-4} mol, 3.6 equivalents) in 5 mL of acetonitrile was added to a mixture of 80 mg of porphyrin **Zn-28** (1.07×10^{-4} mol) in 20 mL of acetonitrile. All porphyrin immediately dissolved and the solution slowly turned purple. The solution was stirred under a nitrogen atmosphere for 3.5 h. The reaction was quenched with an aqueous solution of 900 mg of potassium ferrocyanide in 50 mL of distilled water, followed by the addition of 40 mL of chloroform. The organic layer was washed twice with 50 mL of water and the solvent removed under reduced pressure. The two major products had similar R_f values and could not be purified by column chromatography. The crude porphyrin products were demetalated by dissolving them in a 1:1 mixture of chloroform / trifluoroacetic acid for 1 h, then poured into 50 mL of distilled water. The organic layer was washed with a saturated aqueous solution of sodium bicarbonate and water followed by removal of the solvent under reduced pressure. Flash column chromatography was performed on silica gel using a 2:1 mixture of dichloromethane / hexanes to yield freebase triply-connected porphyrin dimer **H_2-29** (26mg, 36%). The doubly-connected analogue was not obtained in pure form. ^{1}H NMR (400 MHz, $CDCl_3$) δ 8.23 (4H, d, *J*=8 Hz, Ar-H), 7.87 (4H, d, *J*=8 Hz, Ar-H), 7.46 (4H, d, *J*=4 Hz, β-H), 7.39 (4H, d, *J*=4 Hz, β-H), 7.11 (8H, s, Ar-H), 6.91 (4H, br s, β-H), 4.34 (4H, br s, N-H), 4.02 (6H, s, O-CH_3), 2.50 (12H, s, Ar-CH_3), 2.02 (24H, s, Ar-CH_3). MALDI-TOF-MS m/z calcd for $C_{92}H_{74}N_8O_4$ 1355.6, obsd 1355.6. UV-visible-NIR ($\lambda_{max,}$ CH_2Cl_2) 407, 474, 562, 944 (sh), 1051, 1090, 1167 (sh) nm.

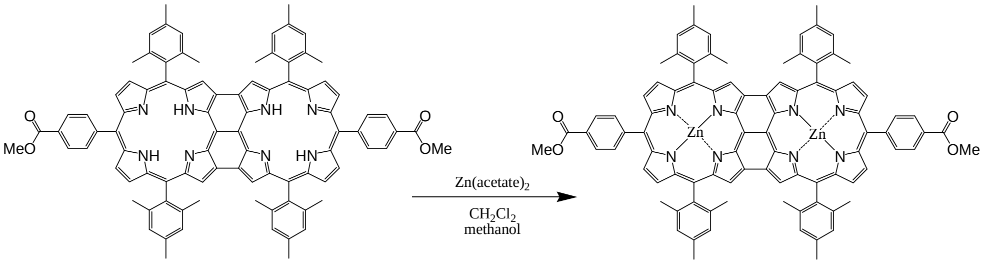

H_2-29 **Zn-29**

Zn-29. Porphyrin dimer **H_2-29** (10 mg, 7.4 x 10^{-6} mol) was metalated using a modified procedure for general porphyrin metalation in which the reaction was refluxed for 3 h and kept warm (~35°C) for a further 24 h. The crude products were chromatographed on silica gel using a 3:1 mixture of dichloromethane / hexanes to yield 6.8 mg of the desired doubly zincated porphyrin dimer **Zn-29** (62%). ^{1}H NMR (400 MHz, $CDCl_3$) δ 8.24 (4H, d, *J*=8 Hz, Ar-H), 7.87 (4H, d, *J*=8 Hz, Ar-H), 7.54 (4H, d, *J*=4 Hz, β-H), 7.47 (4H, d, *J*=4 Hz, β-H), 7.11 (8H, s, Ar-H), 6.94 (4H, s, β-H), 4.34 (4H, br s, N-H), 4.02 (6H, s, O-CH_3), 2.51 (12H, s, Ar-CH_3), 2.01 (24H, s, Ar-CH_3). MALDI-TOF-MS m/z calcd for $C_{92}H_{70}N_8O_4Zn_2$ 1482.4, obsd 1482.6. UV-visible-NIR ($\lambda_{max,}$ CH_2Cl_2) 415, 458, 558, 581, 931, 1055 nm.

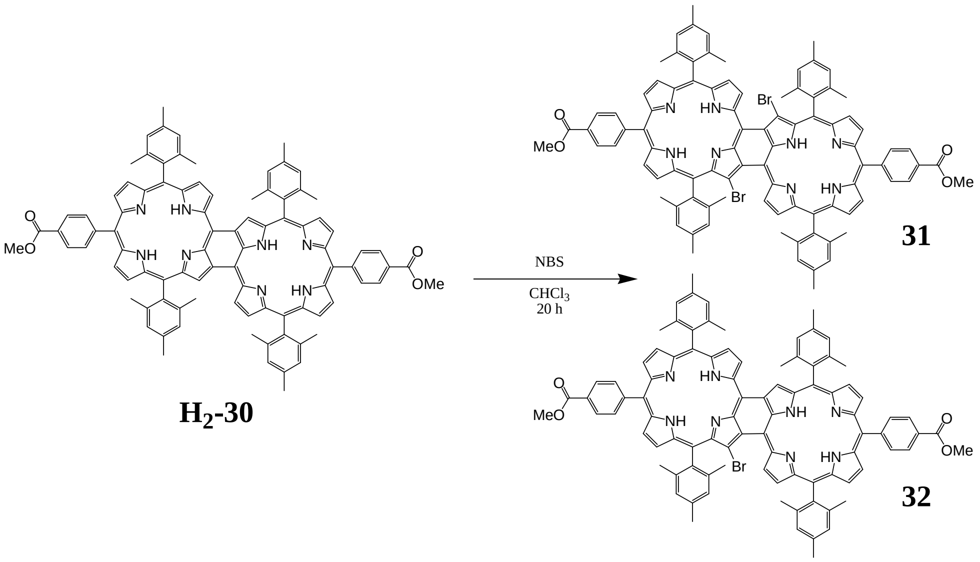

H_2-30

31

32

Bromination of H_2-30. A solution of 34 mg of porphyrin **H_2-30** (2.5×10^{-5} mol) and 4.5 mg of N-bromosuccinimide (2.5×10^{-5} mol) in 10 mL of chloroform was stirred at room temperature for 20 h and then dried by distillation of the solvent under reduced pressure. The crude material was chromatographed on silica using a 2:1 mixture of dichloromethane / hexanes. The dibrominated compound **31** (12 mg, 32%) eluted first followed by the monobrominated compound **32** (10.2 mg, 29%) and lastly the starting material. For **31**: ^{1}H NMR (400 MHz, $CDCl_3$) δ 9.23 (2H, d, *J*=5 Hz, β-H), 8.45-8.25 (6H, br, Ar-H), 8.21 (2H, d, *J*=5 Hz, β-H), 8.20 (2H, d, *J*=5 Hz, β-H), 8.18 (2H, d, *J*=5 Hz, β-H), 8.17 (2H, d, *J*=5 Hz, β-H), 8.12 (2H, d, *J*=5 Hz, β-H), 8.01 (2H, br s, Ar-H), 7.23 (2H, br s, Ar-H), 7.16 (6H, s, Ar-H), 4.08 (6H,s, O-CH_3), 2.54 (6H,s, Ar-CH_3), 2.51 (6H, s, Ar-CH_3), 2.23 (6H, s, Ar-CH_3), 2.07 (6H, s, Ar-CH_3), 1.76 (12H, br s, Ar-CH_3), 1.74 (6H, br s, Ar-CH_3), 1.06 (2H, s, N-H), 0.58 (2H, s, N-H); ^{1}H NMR (500 MHz, d_5-pyridine) δ 9.63 (2H, d, *J*=5 Hz, β-H), 8.53 (2H, d, *J*=5 Hz, β-H), 8.49 (4H, d, *J*=5 Hz, β-H), 8.46 (4H, d, *J*=8 Hz, Ar-H), 8.42 (2H, d, *J*=5 Hz, β-H), 8.31 (2H, d, *J*=5 Hz, β-H), 8.2 (4H, br s, Ar-H), 7.45-7.22 (8H, br m, Ar-H), 4.02 (6H, s, O-CH_3), 2.61 (6H, s, Ar-CH_3), 2.60 (6H, s, Ar-CH_3), 2.51 (6H, s, Ar-CH_3), 2.31 (6H, s, Ar-CH_3), 2.08 (6H, s, Ar-CH_3), 1.94 (6H, s, Ar-CH_3), 1.45 (2H, s, N-H), 0.98 (2H, s, N-H); MALDI-TOF-MS m/z calcd for $C_{92}H_{74}Br_2N_8O_4$ 1514.4, obsd 1514.5; UV-visible-NIR ($\lambda_{max,}$ CH_2Cl_2) 431, 501, 569, 618, 802 nm. For **32**: ^{1}H NMR (400 MHz, $CDCl_3$) δ 9.36 (1H, d, *J*=5 Hz, β-H), 9.21 (1H, d, *J*=5 Hz, β-H), 8.54 (1H, s, β-H), 8.49 (1H, d, *J*=5 Hz, β-H), 8.37 (4H, d, *J*=8 Hz, Ar-H), 8.28-8.15 (13H, β-H, Ar-H), 7.23 (4H, br s, Ar-H), 7.21 (2H, br s, Ar-H), 4.083 (3H, s, O-CH_3), 4.081 (3H, s, O-CH_3), 2.60 (3H, s, Ar-CH_3), 2.58 (3H, s, Ar-CH_3), 2.56 (6H, s, Ar-CH_3), 2.3-1.7 (12H, br s, Ar-CH_3), 2.01 (6H, s, Ar-CH_3), 1.93 (6H, s, Ar-CH_3), 0.95 (2H, s, N-H), 0.38 (2H, br s, N-H); ^{1}H NMR (500 MHz, d_5-pyridine) δ 9.76 (1H, d, *J*=5 Hz, β-H), 9.53 (1H, d, *J*=5 Hz, β-H), 9.01 (1H, s, β-H), 8.59-8.55 (2H, m, β-H), 8.54-8.49 (4H, m, β-H), 8.48-8.43 (6H, m, β-H, Ar-H), 8.29 (1H, d, *J*=5 Hz, β-H), 8.24 (1H, d, *J*=5 Hz, β-H), 8.22-8.18 (4H, br s and d, *J*=8 Hz, Ar-H), 7.5-7.3 (8H, br m, Ar-H), 4.03 (3H, s, O-CH_3), 4.02 (3H, s, O-CH_3), 2.65 (3H, s, Ar-CH_3), 2.62 (6H, s, Ar-CH_3), 2.54 (3H, s, Ar-CH_3), 2.70-1.80 (12H, br s, Ar-CH_3), 2.34 (6H, s, Ar-CH_3), 2.04 (6H, s, Ar-CH_3), 1.50 (2H, s, N-H), 0.84 (2H, br s, N-H); MALDI-TOF-MS m/z calcd for $C_{92}H_{75}BrN_8O_4$ 1436.5, obsd 1436.8; UV-visible-NIR ($\lambda_{max,}$ CH_2Cl_2) 428, 502, 567, 612, 807 nm.

Electrochemistry. See Chapter 6.1 for general electrochemical instrumentation and procedures. Cyclic voltammetry was performed using a 1.6

mm diameter platinum electrode in a standard 3-electrode cell setup. The electrolyte solution consisted of a 100 mM solution of tetra-*n*-butylammonium hexafluorophosphate ($TBAPF_6$) in dichloromethane.

NMR temperature study. ^1H NMR spectra were obtained in deuterated pyridine using a Varian 500 MHz instrument with the temperature calibrated using ethylene glycol with the help of Dr. Brian Cherry.

REFERENCES

1. LLNL; DOE U.S. Energy Flow 2008. https://flowcharts.llnl.gov/ (accessed Jan. 11th, 2012).

2. *International energy outlook 2011 DOE/EIA-0484(2011)*; U.S. EIA: Washington, D.C., 2011; pp 1-202.

3. World economic outlook database. International Monetary Fund: www.imf.org, 2011 (accessed Jan. 12th, 2012).

4. IPCC, 2007: Summary for Policymakers. In: Climate Change 2007: The Physical Science Basis. Contribution of Working Group I to the Fourth Assessment Report of the Intergovernmental Panel on Climate Change [Solomon, S., D. Qin, M. Manning, Z. Chen, M. Marquis, K.B. Averyt, M.Tignor and H.L. Miller (eds.)]. Cambridge University Press, Cambridge, United Kingdom and New York, NY, USA.

5. Afgan, N. H.; Gobaisi, D. A.; Carvalho, M. G.; Cumo, M., Sustainable energy development. *Renewable and Sustainable Energy Reviews* **1998,** *2* (3), 235-286.

6. Xu, Y.; Schoonen, M. A. A., The absolute energy positions of conduction and valence bands of selected semiconducting minerals. *Am. Mineral. 85* (3-4), 543-556.

7. Enright, B.; Redmond, G.; Fitzmaurice, D., Spectroscopic determination of flatband potentials for polycrystalline TiO_2 electrodes in mixed solvent systems. *J. Phys. Chem.* **1994,** *98* (24), 6195-6200.

8. Nazeeruddin, M. K.; Kay, A.; Rodicio, I.; Humphry-Baker, R.; Mueller, E.; Liska, P.; Vlachopoulos, N.; Graetzel, M., Conversion of light to electricity by cis-X_2bis(2,2'-bipyridyl-4,4'-dicarboxylate)ruthenium(II) charge-transfer sensitizers (X = Cl^-, Br^-, I^-, CN^-, and SCN^-) on nanocrystalline titanium dioxide electrodes. *J. Am. Chem. Soc.* **1993,** *115* (14), 6382-90.

9. O'Regan, B.; Graetzel, M., A low-cost, high-efficiency solar cell based on dye-sensitized colloidal titanium dioxide films. *Nature* **1991,** *353* (6346), 737-40.

10. Snaith, H. J., Estimating the Maximum Attainable Efficiency in Dye-Sensitized Solar Cells. *Adv. Funct. Mater.* **2010,** *20* (1), 13-19.

11. Gordon, R. G., Criteria for Choosing Transparent Conductors. *MRS Bull.* **2011,** *25* (08), 52-57.

12. Desilvestro, J.; Graetzel, M.; Kavan, L.; Moser, J.; Augustynski, J., Highly efficient sensitization of titanium dioxide. *J. Am. Chem. Soc.* **1985,** *107* (10), 2988-2990.

13. Matsumura, M.; Matsudaira, S.; Tsubomura, H.; Takata, M.; Yanagida, H., Dye Sensitization and Surface Structures of Semiconductor Electrodes. *Ind. Eng. Chem. Prod. Res. Dev.* **1980,** *19* (3), 415-421.

14. Argazzi, R.; Bignozzi, C. A.; Heimer, T. A.; Castellano, F. N.; Meyer, G. J., Enhanced Spectral Sensitivity from Ruthenium(II) Polypyridyl Based Photovoltaic Devices. *Inorg. Chem.* **1994,** *33* (25), 5741-5749.

15. Gouterman, M., Spectra of porphyrins. *J. Mol. Spectrosc.* **1961,** *6*, 138-163.

16. Nazeeruddin, M. K.; Pechy, P.; Graetzel, M., Efficient panchromatic sensitization of nanocrystalline TiO_2 films by a black dye based on a trithiocyanato-ruthenium complex. *Chem. Commun.* **1997,** (18), 1705-1706.

17. Rothenberger, G.; Fitzmaurice, D.; Graetzel, M., Spectroscopy of conduction band electrons in transparent metal oxide semiconductor films: optical determination of the flatband potential of colloidal titanium dioxide films. *J. Phys. Chem.* **1992,** *96* (14), 5983-6.

18. Lyon, L. A.; Hupp, J. T., Energetics of the Nanocrystalline Titanium Dioxide/Aqueous Solution Interface: Approximate Conduction Band Edge Variations between $H_0= -10$ and $H_-= +26$. *J. Phys. Chem. B* **1999,** *103* (22), 4623-4628.

19. Redmond, G.; Fitzmaurice, D., Spectroscopic determination of flatband potentials for polycrystalline titania electrodes in nonaqueous solvents. *J. Phys. Chem.* **1993,** *97* (7), 1426-1430.

20. Hara, K.; Horiguchi, T.; Kinoshita, T.; Sayama, K.; Arakawa, H., Influence of electrolytes on the photovoltaic performance of organic dye-sensitized nanocrystalline TiO_2 solar cells. *Sol. Energy Mater. Sol. Cells* **2001,** *70* (2), 151-161.

21. Papageorgiou, N.; Athanassov, Y.; Armand, M.; Bonhote, P.; Pettersson, H.; Azam, A.; Graetzel, M., The performance and stability of ambient temperature molten salts for solar cell applications. *J. Electrochem. Soc.* **1996,** *143* (10), 3099-3108.

22. Bonhote, P.; Dias, A.-P.; Papageorgiou, N.; Kalyanasundaram, K.; Graetzel, M., Hydrophobic, Highly Conductive Ambient-Temperature Molten Salts. *Inorg. Chem.* **1996,** *35* (5), 1168-78.

23. Bagno, A.; Butts, C.; Chiappe, C.; D'Amico, F.; Lord, J. C. D.; Pieraccini, D.; Rastrelli, F., The effect of the anion on the physical properties of trihalide-based N,N-dialkylimidazolium ionic liquids. *Org. Biomol. Chem.* **2005,** *3* (9), 1624.

24. Boschloo, G.; Häggman, L.; Hagfeldt, A., Quantification of the Effect of 4-tert-Butylpyridine Addition to I^-/I_3^- Redox Electrolytes in Dye-Sensitized Nanostructured TiO_2 Solar Cells. *J. Phys. Chem. B* **2006,** *110*, 13144-13150.

25. Gratzel, M., Photovoltaic performance and long-term stability of dye-sensitized meosocopic solar cells. *Comptes Rendus Chimie* **2006,** *9* (5-6), 578-583.

26. Kusama, H.; Arakawa, H., Influence of benzimidazole additives in electrolytic solution on dye-sensitized solar cell performance. *J. Photochem. Photobiol. A: Chem.* **2004,** *162* (2-3), 441-448.

27. Bergeron, B. V.; Marton, A.; Oskam, G.; Meyer, G. J., Dye-Sensitized SnO_2 Electrodes with Iodide and Pseudohalide Redox Mediators. *J. Phys. Chem. B* **2005,** *109*, 937-943.

28. Sapp, S. A.; Elliott, C. M.; Contado, C.; Caramori, S.; Bignozzi, C. A., Substituted Polypyridine Complexes of Cobalt(II/III) as Efficient Electron-Transfer Mediators in Dye-Sensitized Solar Cells. *J. Am. Chem. Soc.* **2002,** *124* (37), 11215-11222.

29. Yella, A.; Lee, H. W.; Tsao, H. N.; Yi, C.; Chandiran, A. K.; Nazeeruddin, M. K.; Diau, E. W. G.; Yeh, C. Y.; Zakeeruddin, S. M.; Gratzel, M., Porphyrin-Sensitized Solar Cells with Cobalt (II/III)-Based Redox Electrolyte Exceed 12 Percent Efficiency. *Science* **2011,** *334* (6056), 629-634.

30. Winder, C.; Sariciftci, N. S., Low bandgap polymers for photon harvesting in bulk heterojunction solar cells. *J. Mater. Chem.* **2004,** *14* (7), 1077.

31. Falk, J. E.; Smith, K. M., *Porphyrins and metalloporphyrins*. Elsevier: Amsterdam; Oxford, 1975.

32. Hascoat, P.; Yang, S. I.; Lammi, R. K.; Alley, J.; Bocian, D. F.; Lindsey, J. S.; Holten, D., Effects of Metalation State (Free Base, Mg, Zn, Cd) on Excited-State Energy Transfer in Diarylethyne-Linked Porphyrin Dimers. *Inorg. Chem.* **1999,** *38*, 4849-4853.

33. Kuciauskas, D.; Liddell, P. A.; Lin, S.; Johnson, T. E.; Weghorn, S. J.; Lindsey, J. S.; Moore, A. L.; Moore, T. A.; Gust, D., An Artificial Photosynthetic Antenna-Reaction Center Complex. *J. Am. Chem. Soc.* **1999,** *121* (37), 8604-8614.

34. Kalyanasundaram, K.; Vlachopoulos, N.; Krishnan, V.; Monnier, A.; Graetzel, M., Sensitization of titanium dioxide in the visible light region using zinc porphyrins. *J. Phys. Chem.* **1987,** *91* (9), 2342-7.

35. Lee, C.-W.; Lu, H.-P.; Lan, C.-M.; Huang, Y.-L.; Liang, Y.-R.; Yen, W.-N.; Liu, Y.-C.; Lin, Y.-S.; Diau, E. W.-G.; Yeh, C.-Y., Novel Zinc Porphyrin Sensitizers for Dye-Sensitized Solar Cells: Synthesis and Spectral, Electrochemical, and Photovoltaic Properties. *Chem. Eur. J.* **2009,** *15*, 1403-1412.

36. Wang, Q.; Campbell, W. M.; Bonfantani, E. E.; Jolley, K. W.; Officer, D. L.; Walsh, P. J.; Gordon, K.; Humphry-Baker, R.; Nazeeruddin, M. K.; Graetzel, M., Efficient Light Harvesting by Using Green Zn-Porphyrin-Sensitized Nanocrystalline TiO_2 Films. *J. Phys. Chem. B* **2005,** *109* (32), 15397-15409.

37. de la Garza, L.; Jeong, G.; Liddell, P. A.; Sotomura, T.; Moore, T. A.; Moore, A. L.; Gust, D., Enzyme-Based Photoelectrochemical Biofuel Cell. *J. Phys. Chem. B* **2003,** *107*, 10252-10260.

38. Hambourger, M.; Brune, A.; Gust, D.; Moore Ana, L.; Moore Thomas, A., Enzyme-assisted reforming of glucose to hydrogen in a photoelectrochemical cell. *Photochem Photobiol* **2005,** *81* (4), 1015-20.

39. Umeyama, T.; Takamatsu, T.; Tezuka, N.; Matano, Y.; Araki, Y.; Wada, T.; Yoshikawa, O.; Sagawa, T.; Yoshikawa, S.; Imahori, H., Synthesis and Photophysical and Photovoltaic Properties of Porphyrin−Furan and −Thiophene Alternating Copolymers. *J. Phys. Chem. C* **2009,** *113*, 10798-10806.

40. Bettelheim, A.; White, B. A.; Raybuck, S. A.; Murray, R. W., Electrochemical polymerization of amino-, pyrrole-, and hydroxy-substituted tetraphenylporphyrins. *Inorg. Chem.* **1987,** *26* (7), 1009-1017.

41. Li, G.; Wang, T.; Schulz, A.; Bhosale, S.; Lauer, M.; Espindola, P.; Heinze, J.; Fuhrhop, J.-H., Porphyrin-acetylene-thiophene polymer wires. *Chem. Commun.* **2004,** (5), 552-553.

42. Savenije, T. J.; Koehorst, R. B. M.; Schaafsma, T. J., Spectroelectrochemical Measurement of Charge Transport Properties of Electropolymerized Tetrakis(hydroxyphenyl)porphyrins. *J. Phys. Chem. B* **1997,** *101* (5), 720-725.

43. White, B. A.; Murray, R. W., Kinetics of electron self-exchange reactions between metalloporphyrin sites in submicrometer polymeric films on electrodes. *J. Am. Chem. Soc.* **1987,** *109* (9), 2576-2581.

44. Hayon, J.; Raveh, A.; Bettelheim, A., Electrocatalytic properties of chemically polymerized films of cobalt, iron and manganese tetrakis(o-aminophenyl)porphyrins. *J. Electroanal. Chem.* **1993,** *359* (1–2), 209-221.

45. Rault-Berthelot, J.; Paul-Roth, C.; Poriel, C.; Juillard, S.; Ballut, S.; Drouet, S.; Simonneaux, G., Comparative behaviour of the anodic oxidation of mono-, di- and tetra-arylporphyrins: Towards new electroactive materials with variable bandgaps. *J. Electroanal. Chem.* **2008,** *623* (2), 204-214.

46. Liddell, P. A.; Gervaldo, M.; Bridgewater, J. W.; Keirstead, A. E.; Lin, S.; Moore, T. A.; Moore, A. L.; Gust, D., Porphyrin-Based Hole Conducting Electropolymer. *Chem. Mater.* **2008,** *20* (1), 135-142.

47. Gervaldo, M.; Liddell, P. A.; Kodis, G.; Brennan, B. J.; Johnson, C. R.; Bridgewater, J. W.; Moore, A. L.; Moore, T. A.; Gust, D., A photo- and electrochemically-active porphyrin-fullerene dyad electropolymer. *Photochem. Photobiol. Sci.* **2010,** *9* (7), 890-900.

48. Genies, E. M.; Tsintavis, C., Redox Mechanism and Electrochemical-Behavior of Polyaniline Deposits. *J. Electroanal. Chem.* **1985,** *195* (1), 109-128.

49. Nelson, I. V.; Larson, R. C.; Iwamoto, R. T., Polarographic evidence for the stability of copper(I) ion in some non-complexing nonaqueous solvents. *J. Inorg. Nucl. Chem.* **1961,** *22* (3–4), 279-284.

50. Inamo, M.; Kumagai, H.; Harada, U.; Itoh, S.; Iwatsuki, S.; Ishihara, K.; Takagi, H. D., Electron transfer reactions between copper(II) porphyrin complexes and various oxidizing reagents in acetonitrile. *Dalton Trans.* **2004,** (11), 1703.

51. Inoue, M.; Navarro, R. E.; Inoue, M. B., New soluble polyaniline: Synthesis, electrical properties and solution electronic spectrum. *Synth. Met.* **1989,** *30* (2), 199-207.

52. Brennan, B. J.; Kenney, M. J.; Liddell, P. A.; Cherry, B. R.; Li, J.; Moore, A. L.; Moore, T. A.; Gust, D., Oxidative coupling of porphyrins using copper(II) salts. *Chem. Commun.* **2011,** *47* (36), 10034-10036.

53. Tsuda, A.; Furuta, H.; Osuka, A., Syntheses, Structural Characterizations, and Optical and Electrochemical Properties of Directly Fused Diporphyrins. *J. Am. Chem. Soc.* **2001,** *123* (42), 10304-10321.

54. Ren, X.; Pickup, P. G., Strong dependence of the electron-hopping rate in poly-tris(5-amino-1,10-phenanthroline)iron(III/II) on the nature of the counter-anion. *J. Electroanal. Chem.* **1994,** *365* (1-2), 289-92.

55. O'Connell, K. M.; Waldner, E.; Roullier, L.; Laviron, E., Experimental study of redox modified electrodes with simultaneous electron and proton exchange. *J. Electroanal. Chem. Interfacial Electrochem.* **1984,** *162* (1-2), 77-85.

56. Forster, R. J.; Vos, J. G., Charge transport properties of poly(N-vinylimidazole) containing [Os(N)6]2+/3+ moieties. *J. Inorg. Organomet. Polym.* **1991,** *1* (1), 67-86.

57. Daum, P.; Murray, R. W., Charge-transfer diffusion rates and activity relationships during oxidation and reduction of plasma-polymerized vinylferrocene films. *J. Phys. Chem.* **1981,** *85* (4), 389-96.

58. Daum, P.; Lenhard, J. R.; Rolison, D.; Murray, R. W., Diffusional charge transport through ultrathin films of radiofrequency plasma polymerized vinylferrocene at low temperature. *J. Am. Chem. Soc.* **1980,** *102* (14), 4649-53.

59. Oyama, N.; Yamaguchi, S.; Nishiki, Y.; Tokuda, K.; Matsuda, H.; Anson, F. C., Apparent diffusion coefficients for electroactive anions in coatings of protonated poly(4-vinylpyridine) on graphite electrodes. *J. Electroanal. Chem. Interfacial Electrochem.* **1982,** *139* (2), 371-82.

60. Hjelm, J.; Handel, R. W.; Hagfeldt, A.; Constable, E. C.; Housecroft, C. E.; Forster, R. J., Conducting Polymers Containing In-Chain Metal Centers: Homogeneous Charge Transport through a Quaterthienyl-Bridged {Os(tpy)2} Polymer. *J. Phys. Chem. B* **2003,** *107* (38), 10431-10439.

61. Savenije, T. J.; Koehorst, R. B. M.; Schaafsma, T. J., Spectroelectrochemical measurement of charge transport properties of electropolymerized tetrakis(hydroxyphenyl)porphyrins. *J. Phys. Chem. B* **1997,** *101* (5), 720-725.

62. White, B. A.; Murray, R. W., Electroactive porphyrin films from electropolymerized metallotetra(o-aminophenyl)porphyrins. *J. Electroanal. Chem. Interfacial Electrochem.* **1985,** *189* (2), 345-52.

63. White, B. A.; Murray, R. W., Kinetics of electron self-exchange reactions between metalloporphyrin sites in submicrometer polymeric films on electrodes. *J. Am. Chem. Soc.* **1987,** *109* (9), 2576-81.

64. Yano, J.; Ogura, K.; Kitani, A.; Sasaki, K., The kinetic difference between hydroquinone and Fe^{2+} in the electrochemical response of a polyaniline-film-coated electrode. *Synth. Met.* **1992,** *52* (1), 21-31.

65. Maree, C. H. M.; Roosendaal, S. J.; Savenije, T. J.; Schropp, R. E. I.; Schaafsma, T. J.; Habraken, F. H. P. M., Photovoltaic effects in porphyrin polymer films and heterojunctions. *J. Appl. Phys.* **1996,** *80* (6), 3381-3389.

66. Hogan, C. F.; Forster, R. J., Mediated electron transfer for electroanalysis: transport and kinetics in thin films of [Ru(bpy)2PVP10](ClO4)2. *Anal. Chim. Acta* **1999,** *396* (1), 13-21.

67. Denisevich, P.; Abruna, H. D.; Leidner, C. R.; Meyer, T. J.; Murray, R. W., Electropolymerization of vinylpyridine and vinylbipyridine complexes of iron and ruthenium: homopolymers, copolymers, reactive polymers. *Inorg. Chem.* **1982,** *21* (6), 2153-61.

68. Cole, S. J.; Curthoys, G. C.; Magnusson, E. A.; Phillips, J. N., Ligand binding by metalloporphyrins. III. Thermodynamic functions for the addition of substituted pyridines to nickel(II) and zinc(II) porphyrins. *Inorg. Chem.* **1972,** *11* (5), 1024-1028.

69. Splan, K. E.; Massari, A. M.; Hupp, J. T., A Porous Multilayer Dye-Based Photoelectrochemical Cell That Unexpectedly Runs in Reverse. *J. Phys. Chem. B* **2004,** *108* (13), 4111-4115.

70. He, J.; Lindström, H.; Hagfeldt, A.; Lindquist, S.-E., Dye-Sensitized Nanostructured p-Type Nickel Oxide Film as a Photocathode for a Solar Cell. *J. Phys. Chem. B* **1999,** *103*, 8940-8943.

71. Coakley, K. M.; McGehee, M. D., Conjugated Polymer Photovoltaic Cells. *Chem. Mater.* **2004,** *16*, 4533-4542.

72. Dürr, M.; Rosselli, S.; Yasuda, A.; Nelles, G., Band-Gap Engineering of Metal Oxides for Dye-Sensitized Solar Cells. *J. Phys. Chem. B* **2006,** *110*, 21899-21902.

73. Harris, J. A.; Trotter, K.; Brunschwig, B. S., Interfacial Electron Transfer in Metal Cyanide-Sensitized TiO_2 Nanoparticles. *J. Phys. Chem. B* **2007,** *111*, 6695-6702.

74. Galoppini, E., Linkers for anchoring sensitizers to semiconductor nanoparticles. *Coord. Chem. Rev.* **2004,** *248* (13-14), 1283-1297.

75. McNamara, W. R.; Snoeberger Iii, R. C.; Li, G.; Richter, C.; Allen, L. J.; Milot, R. L.; Schmuttenmaer, C. A.; Crabtree, R. H.; Brudvig, G. W.; Batista, V. S., Hydroxamate anchors for water-stable attachment to TiO_2 nanoparticles. *Energy Environ. Sci.* **2009,** *2* (11), 1173.

76. Brennan, B. J.; Keirstead, A. E.; Liddell, P. A.; Vail, S. A.; Moore, T. A.; Moore, A. L.; Gust, D., 1-(3'-amino)propylsilatrane derivatives as covalent surface linkers to nanoparticulate metal oxide films for use in photoelectrochemical cells. *Nanotechnology* **2009,** *20* (50), 505203/1-505203/10.

77. Nazeeruddin, M. K.; Humphry-Baker, R.; Officer, D. L.; Campbell, W. M.; Burrell, A. K.; Grätzel, M., Application of Metalloporphyrins in Nanocrystalline Dye-Sensitized Solar Cells for Conversion of Sunlight into Electricity. *Langmuir* **2004,** *20*, 6514-6517.

78. Bae, E.; Choi, W.; Park, J.; Shin, H. S.; Kim, S. B.; Lee, J. S., Effects of Surface Anchoring Groups (Carboxylate vs Phosphonate) in Ruthenium-Complex-Sensitized TiO_2 on Visible Light Reactivity in Aqueous Suspensions. *J. Phys. Chem. B* **2004,** *108* (37), 14093-14101.

79. Kilså, K.; Mayo, E. I.; Brunschwig, B. S.; Gray, H. B.; Lewis, N. S.; Winkler, J. R., Anchoring Group and Auxiliary Ligand Effects on the Binding of Ruthenium Complexes to Nanocrystalline TiO_2 Photoelectrodes. *J. Phys. Chem. B* **2004,** *108*, 15640-15651.

80. Shklover, V.; Ovchinnikov, Y. E.; Braginsky, L. S.; Zakeeruddin, S. M.; Grätzel, M., Structure of Organic/Inorganic Interface in Assembled Materials Comprising Molecular Components. Crystal Structure of the Sensitizer Bis[(4,4‘-carboxy-2,2‘-bipyridine)(thiocyanato)]ruthenium(II). *Chem. Mater.* **1998,** *10* (9), 2533-2541.

81. Shklover, V.; Nazeeruddin, M. K.; Grätzel, M.; Ovchinnikov, Y. E., Packing of ruthenium sensitizer molecules on mostly exposed faces of nanocrystalline TiO2: crystal structure of (NBu4+)2[Ru(H2tctterpy)(NCS)3]2−·0.5□DMSO. *Appl. Organomet. Chem.* **2002,** *16* (11), 635-642.

82. Gutiérrez-Sosa, A.; Martínez-Escolano, P.; Raza, H.; Lindsay, R.; Wincott, P. L.; Thornton, G., Orientation of carboxylates on TiO_2(1 1 0). *Surf. Sci.* **2001,** *471* (1–3), 163-169.

83. Bae, E.; Choi, W., Effect of the Anchoring Group (Carboxylate vs Phosphonate) in Ru-Complex-Sensitized TiO_2 on Hydrogen Production under Visible Light. *J. Phys. Chem. B* **2006,** *110* (30), 14792-14799.

84. Park, H.; Bae, E.; Lee, J.-J.; Park, J.; Choi, W., Effect of the Anchoring Group in Ru-Bipyridyl Sensitizers on the Photoelectrochemical Behavior of Dye-Sensitized TiO2 Electrodes: Carboxylate versus Phosphonate Linkages. *J. Phys. Chem. B* **2006,** *110* (17), 8740-8749.

85. Vandervoort, P.; Vansant, E. F., Modification of the silica surface with aminosilanes. *Pol. J. Chem.* **1997,** *71* (5), 550-567.

86. Ghosh, P.; Spiro, T. G., Photoelectrochemistry of tris(bipyridyl)ruthenium(II) covalently attached to n-type tin(IV) oxide. *J. Am. Chem. Soc.* **1980,** *102* (17), 5543-9.

87. Unno, M.; Kakiage, K.; Yamamura, M.; Kogure, T.; Kyomen, T.; Hanaya, M., Silanol dyes for solar cells: higher efficiency and significant durability. *Appl. Organomet. Chem.* **2010,** *24* (3), 247-250.

88. Fung, A. K. M.; Chiu, B. K. W.; Lam, M. H. W., Surface modification of TiO_2 by a ruthenium(II) polypyridyl complex via silyl-linkage for the sensitized photocatalytic degradation of carbon tetrachloride by visible irradiation. *Water Res.* **2003,** *37* (8), 1939-1947.

89. Lee, G. S.; Lee, Y.-J.; Ha, K.; Yoon, K. B., Orientation-Controlled Monolayer Assembly of Zeolite Crystals on Glass Using Terephthaldicarboxaldehyde as a Covalent Linker. *Tetrahedron* **2000,** *56* (36), 6965-6968.

90. Hasobe, T.; Imahori, H.; Sato, T.; Ohkubo, K.; Fukuzumi, S., Enhancement of Light Harvesting and Photocurrent Generation by ITO Electrodes Modified with meso,meso-Linked Porphyrin Oligomers. *Nano Lett.* **2003,** *3*, 409-412.

91. Frye, C. L.; Vincent, G. A.; Finzel, W. A., Pentacoordinate silicon compounds. V. Novel silatrane chemistry. *J. Amer. Chem. Soc.* **1971,** *93* (25), 6805-11.

92. Voronkov, M. G.; Dyakov, V. M.; Kirpichenko, S. V., Silatranes. *J. Organomet. Chem.* **1982,** *233* (1), 1-147.

93. Shlyakhtenko, L. S.; Potaman, V. N.; Sinden, R. R.; Gall, A. A.; Lyubchenko, Y. L., Structure and dynamics of three-way DNA junctions: atomic force microscopy studies. *Nucleic Acids Res.* **2000,** *28* (18), 3472-3477.

94. Shlyakhtenko, L. S.; Gall, A. A.; Filonov, A.; Cerovac, Z.; Lushnikov, A.; Lyubchenko, Y. L., Silatrane-based surface chemistry for immobilization of DNA, protein-DNA complexes and other biological materials. *Ultramicroscopy* **2003,** *97* (1–4), 279-287.

95. Wahab, M. A.; Sudhakar, S.; Yeo, E.; Sellinger, A., Evaporation-Induced Self-Assembly of Mesoscopically Ordered Organic/Organosilica Nanocomposite Thin Films with Photoluminescent Properties and Improved Hardness. *Chem. Mater.* **2008,** *20*, 1855-1861.

96. Albéniz, A. C.; Espinet, P.; López-Fernández, R., Competition of Insertion and Transmetalation Pathways in the Reactions of Alkenylsilanes with Aryl Complexes of Palladium(II). An Experimental Study. *Organometallics* **2006,** *25*, 5449-5455.

97. Akira, S., Recent advances in the cross-coupling reactions of organoboron derivatives with organic electrophiles, 1995–1998. *J. Organomet. Chem.* **1999,** *576* (1–2), 147-168.

98. Sonogashira, K.; Tohda, Y.; Hagihara, N., A convenient synthesis of acetylenes: catalytic substitutions of acetylenic hydrogen with bromoalkenes, iodoarenes and bromopyridines. *Tetrahedron Lett.* **1975,** *16* (50), 4467-4470.

99. Guram, A. S.; Rennels, R. A.; Buchwald, S. L., A Simple Catalytic Method for the Conversion of Aryl Bromides to Arylamines. *Angew. Chem. Int. Ed. Engl.* **1995,** *34* (12), 1348-1350.

100. Dabestani, R.; Bard, A. J.; Campion, A.; Fox, M. A.; Mallouk, T. E.; Webber, S. E.; White, J. M., Sensitization of titanium dioxide and strontium titanate electrodes by ruthenium(II) tris(2,2'-bipyridine-4,4'-dicarboxylic acid) and zinc tetrakis(4-carboxyphenyl)porphyrin: an evaluation of sensitization efficiency for component photoelectrodes in a multipanel device. *J. Phys. Chem.* **1988,** *92* (7), 1872-8.

101. Sprintschnik, G.; Sprintschnik, H. W.; Kirsch, P. P.; Whitten, D. G., Photochemical reactions in organized monolayer assemblies. 6. Preparation and photochemical reactivity of surfactant ruthenium(II) complexes in monolayer assemblies and at water-solid interfaces. *J. Am. Chem. Soc.* **1977,** *99* (15), 4947-54.

102. Bonfantini, E. E.; Burrell, A. K.; Campbell, W. M.; Crossley, M. J.; Gosper, J. J.; Harding, M. M.; Officer, D. L.; Reid, D. C. W., Efficient synthesis of free-base 2-formyl-5,10,15,20-tetraarylporphyrins, their reduction and conversion to [(porphyrin-2-yl)methyl]phosphonium salts. *J. Porphyrins Phthalocyanines* **2002,** *06* (11), 708.

103. Inoue, H.; Tsubouchi, H.; Nagaoka, Y.; Tomioka, K., Synthesis of allenes by double Horner–Wadsworth–Emmons reaction. *Tetrahedron* **2002,** *58* (1), 83-90.

104. Locos, O. B.; Dahms, K.; Senge, M. O., Allenylporphyrins: a new motif on the porphyrin periphery. *Tetrahedron Lett.* **2009,** *50* (21), 2566-2569.

105. Nasr, C.; Kamat, P. V.; Hotchandani, S., Photoelectrochemistry of Composite Semiconductor Thin Films. Photosensitization of the SnO_2 /TiO_2 Coupled System with a Ruthenium Polypyridyl Complex. *J. Phys. Chem. B* **1998,** *102*, 10047-10056.

106. Bard, A. J.; Faulkner, L. R., *Electrochemical methods : fundamentals and applications*. John Wiley: New York, 2001.

107. Bahr, J. L.; Kuciauskas, D.; Liddell, P. A.; Moore, A. L.; Moore, T. A.; Gust, D., Driving force and electronic coupling effects on photoinduced electron transfer in a fullerene-based molecular triad. *Photochem. Photobiol.* **2000,** *72* (5), 598-611.

108. James, D. R.; Ware, W. R., Recovery of underlying distributions of lifetimes from fluorescence decay data. *Chem. Phys. Lett.* **1986,** *126* (1), 7-11.

109. Siemiarczuk, A.; Wagner, B. D.; Ware, W. R., Comparison of the maximum entropy and exponential series methods for the recovery of distributions of lifetimes from fluorescence lifetime data. *J. Phys. Chem.* **1990,** *94* (4), 1661-6.

110. Closs, G. L.; Miller, J. R., Intramolecular long-distance electron transfer in organic molecules. *Science* **1988,** *240* (4851), 440-7.

111. Datta, J.; Bhattacharya, A.; Kundu, K. K., Relative standard electrode potentials of I_3^-/I^-, I_2/I_3^-, and I_2/I^- redox couples and the related formation constants of I_3^- in some pure and mixed dipolar aprotic solvents. *Bull. Chem. Soc. Jpn.* **1988,** *61* (5), 1735-1742.

112. Iguchi, N.; Cady, C.; Snoeberger Iii, R. C.; Hunter, B. M.; Sproviero, E. M.; Schmuttenmaer, C. A.; Crabtree, R. H.; Brudvig, G. W.; Batista, V. S., Characterization of siloxane adsorbates covalently attached to TiO_2. *Proc. of SPIE* **2008,** *7034*, 70340C1-70340C-8.

113. Hotchkiss, P. J.; Jones, S. C.; Paniagua, S. A.; Sharma, A.; Kippelen, B.; Armstrong, N. R.; Marder, S. R., The Modification of Indium Tin Oxide with Phosphonic Acids: Mechanism of Binding, Tuning of Surface Properties, and Potential for Use in Organic Electronic Applications. *Acc. Chem. Res.* **2011**, 111019085014005.

114. Luschtinetz, R.; Frenzel, J.; Milek, T.; Seifert, G., Adsorption of Phosphonic Acid at the TiO_2 Anatase (101) and Rutile (110) Surfaces. *J. Phys. Chem. C* **2009,** *113* (14), 5730-5740.

115. Di Valentin, C.; Costa, D., Anatase TiO_2 Surface Functionalization by Alkylphosphonic Acid: A DFT+D Study. *J. Phys. Chem. C* **2012,** *116* (4), 2819-2828.

116. Zhou, Y.; Li, X.; Zhang, J.; Zhou, X.; Lin, Y., Performances improvement of eosin Y sensitized solar cells by modifying TiO_2 electrode with silane-coupling reagent. *Chin. Sci. Bull.* **2009,** *54* (15), 2633-2640.

117. Rochford, J.; Chu, D.; Hagfeldt, A.; Galoppini, E., Tetrachelate Porphyrin Chromophores for Metal Oxide Semiconductor Sensitization: Effect of the Spacer Length and Anchoring Group Position. *J. Am. Chem. Soc.* **2007,** *129*, 4655-4665.

118. Paniagua, S. A.; Hotchkiss, P. J.; Jones, S. C.; Marder, S. R.; Mudalige, A.; Marrikar, F. S.; Pemberton, J. E.; Armstrong, N. R., Phosphonic Acid Modification of Indium−Tin Oxide Electrodes: Combined XPS/UPS/Contact Angle Studies. *Journal of Physical Chemistry C* **2008,** *112*, 7809-7817.

119. Ukaji, E.; Furusawa, T.; Sato, M.; Suzuki, N., The effect of surface modification with silane coupling agent on suppressing the photo-catalytic activity of fine TiO_2 particles as inorganic UV filter. *Appl. Surf. Sci.* **2007,** *254* (2), 563-569.

120. Guerrero, G.; Mutin, P. H.; Vioux, A., Anchoring of Phosphonate and Phosphinate Coupling Molecules on Titania Particles. *Chem. Mater.* **2001,** *13* (11), 4367-4373.

121. Cleland, D. M.; Gordon, K. C.; Officer, D. L.; Wagner, P.; Walsh, P. J., Tuning the optical properties of ZnTPP using carbonyl ring fusion. *Spectrochim. Acta Part A* **2009,** *74* (4), 931-935.

122. Imahori, H.; Umeyama, T.; Ito, S., Large π-Aromatic Molecules as Potential Sensitizers for Highly Efficient Dye-Sensitized Solar Cells. *Acc. Chem. Res.* **2009,** *42*, 1809-1818.

123. Rogers, J. E.; Nguyen, K. A.; Hufnagle, D. C.; McLean, D. G.; Su, W.; Gossett, K. M.; Burke, A. R.; Vinogradov, S. A.; Pachter, R.; Fleitz, P. A., Observation and Interpretation of Annulated Porphyrins: Studies on the Photophysical Properties of meso- Tetraphenylmetalloporphyrins. *J. Phys. Chem. A* **2003,** *107*, 11331-11339.

124. Kim, K. S.; Lim, J. M.; Osuka, A.; Kim, D., Various strategies for highly-efficient two-photon absorption in porphyrin arrays. *J. Photochem. Photobiol. C: Photochem. Rev.* **2008,** *9* (1), 13-28.

125. Osuka, A.; Shimidzu, H., meso, meso-Linked Porphyrin Arrays. *Angew. Chem. Int. Ed. Engl.* **1997,** *36* (1-2), 135-137.

126. Tsuda, A.; Furuta, H.; Osuka, A., Completely Fused Diporphyrins and Triporphyrin. *Angew. Chem.* **2000,** *112* (14), 2649-2652.

127. Fendt, L.-A.; Fang, H.; Plonska-Brzezinska, M. E.; Zhang, S.; Cheng, F.; Braun, C.; Echegoyen, L.; Diederich, F., meso,meso-Linked and Triply Fused Diporphyrins with Mixed-Metal Ions: Synthesis and Electrochemical Investigations. *Eur. J. Org. Chem.* **2007,** *2007* (28), 4659-4673.

128. Aratani, N.; Osuka, A.; Kim, Y. H.; Jeong, D. H.; Kim, D., Extremely Long, Discrete meso□–□meso-Coupled Porphyrin Arrays. *Angew. Chem. Int. Ed.* **2000,** *39* (8), 1458-1462.

129. Tsuda, A.; Osuka, A., Fully Conjugated Porphyrin Tapes with Electronic Absorption Bands That Reach into Infrared. *Science* **2001,** *293* (5527), 79-82.

130. Wallace, G. G.; Spinks, G. M.; Kane-Maguire, L. A. P.; Teasdale, P. R., *Conductive electroactive polymers : intelligent materials systems*. CRC: Boca Raton, 2003.

131. Sahoo, A. K.; Nakamura, Y.; Aratani, N.; Kim, K. S.; Noh, S. B.; Shinokubo, H.; Kim, D.; Osuka, A., Synthesis of Brominated Directly Fused Diporphyrins through Gold(III)-Mediated Oxidation. *Org. Lett.* **2006,** *8*, 4141-4144.

132. Yoshida, N.; Aratani, N.; Osuka, A., Poly(zinc(II)-5,15-porphyrinylene) from silver(I)-promoted oxidation of zinc(II)-5,15-diarylporphyrins. *Chem. Commun.* **2000,** (3), 197-198.

133. Kamo, M.; Tsuda, A.; Nakamura, Y.; Aratani, N.; Furukawa, K.; Kato, T.; Osuka, A., Metal-Dependent Regioselective Oxidative Coupling of 5,10,15-Triarylporphyrins with DDQ-Sc(OTf)$_3$ and Formation of an Oxo-quinoidal Porphyrin. *Org. Lett.* **2003,** *5*, 2079-2082.

134. Cho, H. S.; Jeong, D. H.; Cho, S.; Kim, D.; Matsuzaki, Y.; Tanaka, K.; Tsuda, A.; Osuka, A., Photophysical Properties of Porphyrin Tapes. *J. Am. Chem. Soc.* **2002,** *124* (49), 14642-14654.

135. Heo, J. H.; Ikeda, T.; Lim, J. M.; Aratani, N.; Osuka, A.; Kim, D., Molecular-Shape-Dependent Photophysical Properties ofmeso-β Doubly Linked Zn(II) Porphyrin Arrays and Their Indene-Fused Analogues†. *J. Phys. Chem. B* **2010,** *114* (45), 14528-14536.

136. Yoon, M.-C.; Noh, S. B.; Tsuda, A.; Nakamura, Y.; Osuka, A.; Kim, D., Photophysics ofmeso-β Doubly Linked Ni(II) Porphyrin Arrays: Large Two-Photon Absorption Cross-Section and Fast Energy Relaxation Dynamics. *J. Am. Chem. Soc.* **2007,** *129* (33), 10080-10081.

137. Frampton, M. J.; Accorsi, G.; Armaroli, N.; Rogers, J. E.; Fleitz, P. A.; McEwan, K. J.; Anderson, H. L., Synthesis and near-infrared luminescence of a deuterated conjugated porphyrin dimer for probing the mechanism of non-radiative deactivation. *Org. Biomol. Chem.* **2007,** *5* (7), 1056.

138. Mruthyunjaya, H. C.; Vasudeva Murthy, A. R., Formal oxidation-reduction potentials of copper(II)-copper(I) systems in acetonitrile. *J. Electroanal. Chem* **1968,** *18* (1–2), 200-204.

139. Badoz-Lambling, J.; Bardin, J. C., Solvatation des ions par le nitromethane. *Electrochim. Acta* **1974,** *19* (11), 725-731.

140. Noviandri, I.; Brown, K. N.; Fleming, D. S.; Gulyas, P. T.; Lay, P. A.; Masters, A. F.; Phillips, L., The Decamethylferrocenium/Decamethylferrocene Redox Couple: A Superior Redox Standard to the Ferrocenium/Ferrocene Redox Couple for Studying Solvent Effects on the Thermodynamics of Electron Transfer. *J. Phys. Chem. B* **1999,** *103* (32), 6713-6722.

141. Larson, R. C.; Iwamoto, R. T., Electrochemical and Infrared Evaluation of the Formation Constants of Aquo-Copper(II) Complexes in Nitromethane. *Inorg. Chem.* **1962,** *1* (2), 316-323.

142. Miyahara, T.; Nakatsuji, H.; Hasegawa, J.; Osuka, A.; Aratani, N.; Tsuda, A., Ground and excited states of linked and fused zinc porphyrin dimers: Symmetry adapted cluster (SAC)—configuration interaction (CI) study. *J. Chem. Phys.* **2002,** *117* (24), 11196.

143. Gutowsky, H. S.; Holm, C. H., Rate Processes and Nuclear Magnetic Resonance Spectra. II. Hindered Internal Rotation of Amides. *J. Chem. Phys.* **1956,** *25* (6), 1228-1234.

144. Eaton, S. S.; Eaton, G. R., Rotation of phenyl rings in metal complexes of substituted tetraphenylporphyrins. *J. Am. Chem. Soc.* **1975,** *97* (13), 3660-3666.

145. Eaton, S. S.; Eaton, G. R., Effects of para substituent and metal ion on rates of phenyl ring rotation in ruthenium, indium, and titanium complexes of para-substituted tetraphenylporphyrins. *J. Am. Chem. Soc.* **1977,** *99* (20), 6594-6599.

146. Dirks, J. W.; Underwood, G.; Matheson, J. C.; Gust, D., Conformational dynamics of .alpha.,.beta.,.gamma.,.delta.-tetraarylporphyrins and their dications. *J. Org. Chem.* **1979,** *44* (14), 2551-2555.

147. McEvoy, J. P.; Brudvig, G. W., Water-Splitting Chemistry of Photosystem II. *Chem. Rev.* **2006,** *106* (11), 4455-4483.

148. Smeets, S.; Roex, H.; Dehaen, W., Asymmetrically protected porphyrin meso-tetraphenols and their application in the synthesis of pentaporphyrin dendrimers. *ARKIVOC* **2003,** (4), 83-92.

149. Sullivan, B. P.; Salmon, D. J.; Meyer, T. J., Mixed phosphine 2,2'-bipyridine complexes of ruthenium. *Inorg. Chem.* **1978,** *17* (12), 3334-41.

150. Muthukumaran, K.; Loewe, R. S.; Ambroise, A.; Tamaru, S.-i.; Li, Q.; Mathur, G.; Bocian, D. F.; Misra, V.; Lindsey, J. S., Porphyrins Bearing Arylphosphonic Acid Tethers for Attachment to Oxide Surfaces. *J. Org. Chem.* **2004,** *69* (5), 1444-1452.

151. Kang, M. G.; Park, N. G.; Park, Y. J.; Ryu, K. S.; Chang, S. H., Manufacturing method for transparent electric windows using dye-sensitized TiO_2 solar cells. *Sol. Energy Mater. Sol. Cells* **2003,** *75* (3), 475-479.

APPENDIX

PUBLICATIONS

The research summarized in this dissertation has resulted in the following peer-reviewed publications:

Brennan, B. J.; Keirstead, A. E.; Liddell, P. A.; Vail, S. A.; Moore, T. A.; Moore, A. L.; Gust, D., 1-(3'-amino)propylsilatrane derivatives as covalent surface linkers to nanoparticulate metal oxide films for use in photoelectrochemical cells. *Nanotechnology* **2009,** *20* (50), 505203/1-505203/10.

Gervaldo, M.; Liddell, P. A.; Kodis, G.; Brennan, B. J.; Johnson, C. R.; Bridgewater, J. W.; Moore, A. L.; Moore, T. A.; Gust, D., A photo- and electrochemically-active porphyrin-fullerene dyad electropolymer. *Photochem. Photobiol. Sci.* **2010,** *9* (7), 890-900.

Brennan, B. J.; Kenney, M. J.; Liddell, P. A.; Cherry, B. R.; Li, J.; Moore, A. L.; Moore, T. A.; Gust, D., Oxidative coupling of porphyrins using copper(II) salts. *Chem. Commun.* **2011,** *47* (36), 10034-10036.